Quantifying Galactic Propagation Uncertainty in WIMP Dark Matter Search with AMS01 Z=-1 Spectrum
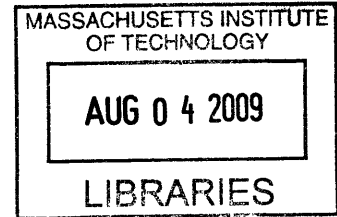
by

Sa Xiao

Submitted to the Department of Physics
in partial fulfillment of the requirements for the degree of

Doctor of Philosophy

at the

MASSACHUSETTS INSTITUTE OF TECHNOLOGY

June 2009

Author ....
Department of Physics
May 30, 2009

Certified by....................................
Peter Fisher
Professor
Thesis Supervisor

Accepted by ....
Thomas Greytak
Associate Department Head for Education

Quantifying Galactic Propagation Uncertainty in WIMP Dark Matter Search with AMS01 Z=-1 Spectrum

by

Sa Xiao

Submitted to the Department of Physics
on May 30, 2009, in partial fulfillment of the
requirements for the degree of
Doctor of Philosophy

Abstract

A search for a WIMP dark matter annihilation signal is carried out in the AMS01 negatively charged (Z=-1) particle spectrum, following a set of supersymmetric benchmark scenarios in the mSUGRA framework. The result is consistent with no dark matter, assuming a smooth isothermal distribution of dark matter in the Galactic halo. 90% upper bounds of the boost factor by which the flux from the DM annihilation could be enhanced without exceeding AMS01 data are derived to be $\sim 10^2 - 10^5$, varied as different mSUGRA senarios. The Boron-to-Carbon ratio energy spectrum is measured with AMS01, which allows us to constrain the cosmic ray (CR) Galactic propagation parameters. In the diffusive reaccelaration (DR) model, the propagation parameters are shown to be $D_{xx} \sim 4.5 \times 10^{28} - 6 \times 10^{28}$ cm^2 s^{-1}, and $v_A \sim 28 - 42$ km s^{-1}. The impact of the uncertainties in the cosmic ray propagation model on dark matter limits is studied and the associated uncertainties of the 90% upper bound of the boost factor are found to be less than 30%.

Thesis Supervisor: Peter Fisher
Title: Professor

Acknowledgments

Contents

Chapter 1

Introduction

Many observations imply the existence of dark matter [21]. However, its nature still remains mysterious. Weakly interacting massive particles (WIMPs) are promising candidates [21], particularly the lightest supersymmetric particle (LSP), which may self-annihilate producing standard model charged particles. If this is the case, we will have a chance to detect WIMPs indirectly through their annihilation products in cosmic rays [21].

The AMS01 (Alpha Magnetic Spectrometer) experiment, a magnetic spectrometer designed to measure charged cosmic rays from several hundred MeV to about 300 GeV (see chapter 4 see for a description of the AMS experiment), collected data for ten days while on board the STS-91 Flight of Discovery. Previous work [24] [55] carried out a search for a WIMP annihilation signal in the AMS01 negatively charged (Z=-1) particle spectrum. The result was consistent with no dark matter, assuming a smooth isothermal distribution of dark matter in the halo, for the set of supersymmetric benchmark scenarios proposed in [17] in the constrained Minimum Supersymmetric Standard Model (cMSSM) framework. However, many theories and numerical simulations predict clumps of dark matter may exist [22] [41]. For clumpy halos, the rate of WIMP annihilation may be enhanced by orders of magnitude. Such magnification resulting from the clumpiness of dark matter is parameterized by the boost factor. We can derive an upper bound of the boost factor by which the electron flux from the DM annihilation could be enhanced without exceeding AMS01 data.

The modeling of charged particle propagation in the galaxy [58] introduces an uncertainty into any WIMP search using cosmic rays. In this thesis I study the impact of uncertainties in the cosmic ray propagation model on dark matter limits. The transport mechanisms of cosmic rays in the galaxy are dominated by particle diffusion in the galactic magnetic fields. Some elements, such as Carbon, Nitrogen and Oxygen, are directly injected into cosmic rays by supernova explosions. These are called primary nuclei. Other elements, such as Lithium, Beryllium and Boron, on the other hand, are mainly generated during cosmic ray propagation, since these light elements would have been destroyed during nucleosynthesis in the sources. These secondary nuclei can be used to measure the amount of interstellar matter through which the primary nuclei pass between the source and the Earth. The ratio of the number of secondary to the primary elements is largely independent of the injection

spectra, and is a good probe of the propagation model. The Boron-to-Carbon ratio is a very effective secondary-to-primary ratio for such purpose because they are relatively well measured in the cosmic rays and the cross sections for the production of their secondaries are well known. AMS01 had good capability to distinguish charged particles up to Oxygen (Z=8). The major tasks of this work are: (1) Measure the Boron-to-Carbon ratio as a function of energy using AMS01 data, and use it to constrain the galactic propagation parameters, such as the spatial diffusion coefficient and Alfven velocity [8] which controls the reacceleration (see Chapter 3) level. (2) Upon getting a good region in the propagation parameter space, run through the whole WIMP search analysis with different propagation parameters to quantify the uncertainty in the dark matter sensitivity resulting from the propagation models. In the end, PAMELA results and prospects for future experiments on indirect dark matter searches, especially AMS02, are also briefly discussed.

Chapter 2

Dark Matter

2.1 Evidence for Dark Matter

The first hints of dark matter arose from the study of a cluster of galaxies. Galaxy clusters are the largest gravitationally bound systems in the universe. In 1933, Fritz Zwicky [67] applied the virial theorem to the Coma cluster of galaxies and found that the mass estimated in this way was about 400 times larger than that estimated based on the brightness of the cluster. Even counting the X-Ray gas which makes up $\sim 50\%$ of the baryonic mass of the cluster, there is still far less mass than that deduced from the gravitational effect. A lot of evidence thereafter has been accumulated in the favor of the existence of dark matter, which infers its existence mostly only via gravitational force. One galactic scales, the observations of the rotation curves of galaxies reveals the existence of unseen matter. The roatation curve describes the orbital velocities of stars and gas as a function of their distance from the galactic center. In Newtonian dynamics the circular velocity is $v(r) = \sqrt{\frac{GM(r)}{r}}$, which is expected to be falling $\propto 1/\sqrt{r}$ beyond the galactic bulge or visible disks. However observed rotation curves [60] exhibit a characteristic flat behavior at large distances, even far beyond the visible disks. For example, in our own Galaxy, $v \approx 220$ km/s at the location of our solar system (8.5 kpc) and remains largely constant out to the largest observable radius (~ 50 kpc). Flat rotation curves can be explained by the presence of a dark halo with density $\rho(r) \propto 1/r^2$, so that $M(r) \propto r$.

Recent N-body simulations suggest the existence of a universal dark matter profile [52]. A generic parametrization of a dark matter halo density is

$$\rho(r) = \frac{\rho_0}{(r/R)^\gamma (1 + (r/R)^\alpha)^{(\beta-\gamma)/\alpha}}$$

Some widely used halo profile models include the isothermal (Iso) [19], Navarro, Frenk and White [52], and Moore, et al [49]. Their values of the parameters $(R, \alpha, \beta, \gamma)$ are given in Table 2.1. I use isothermal profile in this analysis, which is the most conservative one in terms of annihilation rate. The most recent estimate of our local dark matter density, ρ_0, assuming an isothermal profile, is $\rho_0 \approx 0.3$ GeV/cm^3 [38]. There is, however, significant uncertainty in ρ_0. For example, this value may be

Model	α	β	γ	R(kpc)
Iso	2.0	2.0	0	3.5
NFW	1.0	3.0	1.0	20.0
Moore	1.5	3.0	1.5	28.0

Table 2.1: Parameters of some widely used profile models for the dark matter density in galaxies.R is the galactic core radius, and can vary from galaxy to galaxy

increased up to a factor of 2 due to the detailed model of our Galaxy [38]. I use $\rho_0 = 0.3$ GeV/cm^3 in my analysis.

The joint analysis of the anisotropy of the cosmic microwave background (CMB), large scale structure and Type Ia supernova data [44], provide stringent constraints on the constituents of the mass-energy budget of the Universe: baryons, dark matter and dark energy. The results indicate that neutrinos are far from enough to account for all the dark matter [56], and that dark matter is cold or warm, and non-baryonic [21]. The dark matter is now known to be about 22% of the total energy density in the universe ($\Omega_{DM} \approx 0.22$)[42], which provides an important constraint on theoretical modeling of dark matter candidates.

2.2 Dark Matter Candidates

Candidates for DM must be non-baryonic, cold or warm, and stable over cosmological time scales, which leave open many possibilities. There are numerous plausible DM candidates that have been discussed in the literature ([21], [26] and references therein), whose masses and interaction cross sections span many orders of magnitudes, as shown in Figure 2-1.

2.2.1 WIMPs

Weakly interacting massive particles (WIMPs) are among the most well-motivated DM candidates. WIMPs are particles with mass mix roughly between 10 GeV to several TeV, and with cross sections near the weak scale. Their present relic density can be calculated reliably assuming WIMPs are in the thermal and chemical equilibrium with the hot soup of Standard Model particles after inflation. When their interaction rate drops below the expansion rate of the Universe, WIMPs drop out of thermal equilibrium ("freeze out"), and their co-moving density remains constant afterwords. Freeze-out happens at temperature $T_F \approx m_\chi/20$, which implies that WIMPs are already non-relativistic (cold) when decoupling from the thermal plasma. An order-of-magnitude estimate of the relic density of WIMPs is given by [37]:

$$\Omega_\chi h^2 \approx \frac{0.1 pb \cdot c}{< \sigma_A v >}$$

For $< \sigma_A v > = 1$ pb·c, typical for the weak scale, this thermal relic density has the right order of magnitude required by cosmology ($\Omega_{DM} \approx 0.22$). A leading WIMP

candidate is the neutralino, a SUSY particle.

Some Dark Matter Candidate Particles
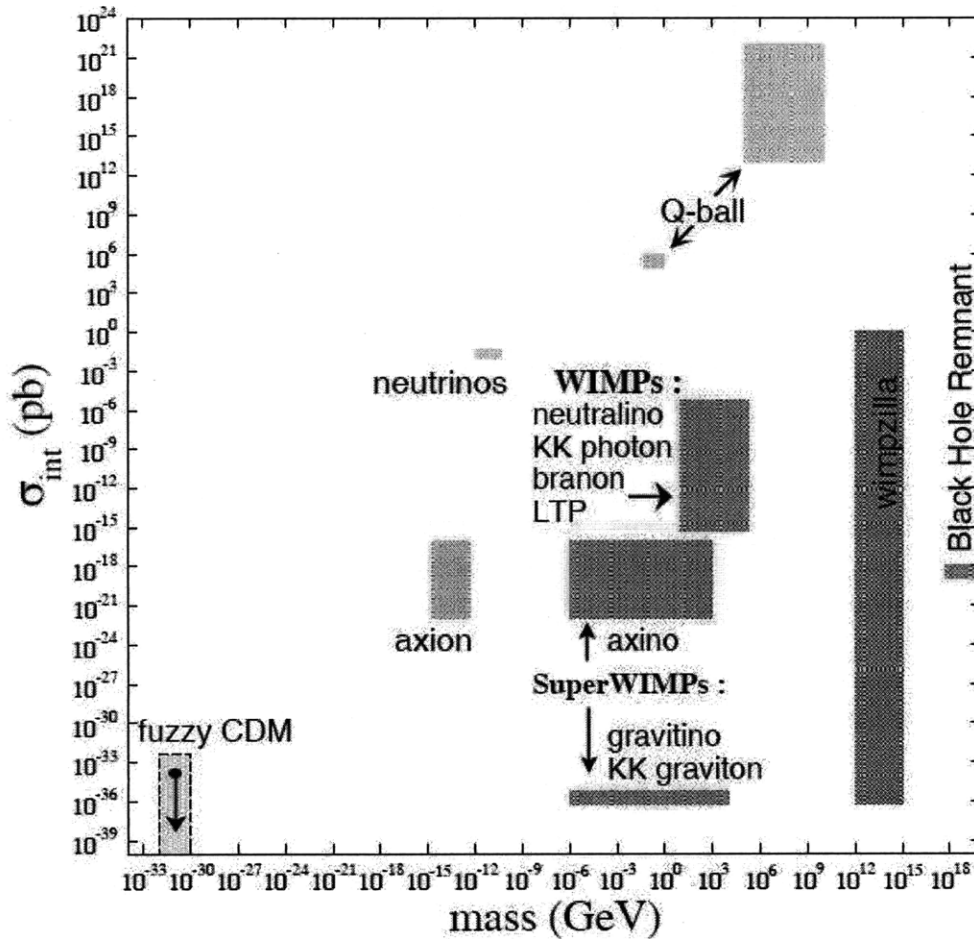
Figure 2-1: Various dark matter candidates on a mass versus interaction cross-section plot [26]

2.2.2 Supersymmetric Dark Matter

A lot of problems remaining unsolved by the current Standard Model of particle physics indicate that our Standard Model may be only the low-energy limit of a more fundamental theory. Supersymmetry (SUSY) [37] is one of the most popular extensions of the Standard Model. Many features make SUSY very attractive. One is its role in understanding the hierarchy problem — why the weak force is 10^{32} times stronger than gravity. The question is actually why the Higgs boson is so much lighter than the Plank mass. The problem arises in the radiative corrections to the mass of the Higgs boson. At 1-loop, the correction scales as $\delta m_s^2 \sim (\frac{\alpha}{2\pi})\Lambda^2$, where Λ is a high-energy cut-off where new physics become to play an important role. If we take this scale to be the Planck scale, then we have a quadratically

diverging Lagrangian. Supersymmetry provides a solution to this divergence problem. It assumes that there exists a superpartner of each Standard Model particle, with the same mass but with spin different by 1/2 (turning bosons to fermions, and vice versa). Since the contribution of fermion loops to δm_s^2 have opposite sign to the corresponding bosonic loops, the quadratic divergence terms are canceled out, and the radiative correction at 1-loop level becomes [21]

$$\delta m_s^2 \sim (\frac{\alpha}{2\pi})(\Lambda^2 + m_B^2) - (\frac{\alpha}{2\pi})(\Lambda^2 + m_F^2) = (\frac{\alpha}{2\pi})(m_B^2 - m_F^2)$$

Provided $|m_B^2 - m_F^2| \leq 1$ TeV, supersymmetric algebra ensures that perturbation theory is valid up to the Planck scale.

Another reason for interest in SUSY is that it naturally makes the gauge couplings of strong, weak and electromagnetic forces converge at a scale $M_U \approx 2 \times 10^{16}$ GeV [10]. Without the contribution of SUSY partners, the extrapolation of the coupling constants using only Standard Model particles fail to converge to a common value.

Last but not least, Supersymmetry provides an excellent dark matter candidate: the lightest stable particle, called the neutralino. The superpartners of gauge bosons B,W_3 (or photon and Z, equivalently), and the neutral Higgs bosons H_1^0, H_2^0, mix into four Majorana fermionic mass eigenstates.

$$\chi = N_{11}\widetilde{B} + N_{12}\widetilde{W_3} + N_{21}\widetilde{H_1}^0 + N_{22}\widetilde{H_2}^0$$

The neutralino is the lightest mass eigenstate. Provided R-parity [65] is conserved, the neutralino is stable and can only be destroyed via pair annihilation (because the neutralino is a Majorana particle, which means it is its own anti-particle). As discussed before, as long as their self-annihilation cross section is of weak strength, neutralino relic density can account for the cosmological DM. The leading channels for neutralino annihilations are annihilations to fermion-antifermion pairs (primarily heavy fermions, such as bottom and charm quarks and tau leptons), gauge bosons pairs (W^+W^-, ZZ) and final states containing Higgs bosons. For a complete list of all tree level processes, see [37].

2.3 (c)MSSM and Benchmark Points

The Minimal Supersymmetric Standard Model (MSSM) is the minimal supersymmetric extension of the Standard Model, in the sense that it contains the smallest possible field content necessary to give rise to all the fields of the Standard Model. We associate fermionic superpartners to all gauge fields (Gluons,$W^\pm, Z, \gamma$), and scalar superpartners to all fermions (quarks and leptons). Finally, two Higgs superfields need to be introduced, up-type Higgs doublets and down-type Higgs doublets, where only one is required in the Standard Model. An extra one is necessary because it is impossible to introduce Yukawa couplings of both up and down type quarks to the same Higgs field in the MSSM [37]. Furthermore, introducing the second Higgs field can make the theory anomaly-free [53]. Table 2.2 is a summary of the resulting particle

Superfield	SM particles	Spin	Superpartners	Spin
Q	$\begin{pmatrix} u_L \\ d_L \end{pmatrix}$	1/2	$\begin{pmatrix} \widetilde{u_L} \\ \widetilde{d_L} \end{pmatrix}$	0
U^c	$\overline{u_R}$	1/2	$\widetilde{u_R}^*$	0
D^c	$\overline{d_R}$	1/2	$\widetilde{d_R}^*$	0
L	$\begin{pmatrix} \nu_L \\ e_L \end{pmatrix}$	1/2	$\begin{pmatrix} \widetilde{\nu_L} \\ \widetilde{e_L} \end{pmatrix}$	0
E^c	$\overline{e_R}$	1/2	$\widetilde{e_R}^*$	0
H_1	H_1	0	$\widetilde{H_1}$	1/2
H_2	H_2	0	$\widetilde{H_2}$	1/2
G^a	g	1	$\widetilde{g}$	1/2
W_i	W_i	1	$\widetilde{W_i}$	1/2
B	B	1	$\widetilde{B}$	1/2

Table 2.2: Field content of MSSM

content of MSSM.

The MSSM has 105 free parameters. Practical phenomenological study of the MSSM requires that the number of parameters must be reduced by making some theoretically well-motivated assumptions. The minimum supergravity (mSUGRA) scenario [39], a constrained MSSM (cMSSM), is a popular phenomenological model, in which the gauge couplings, the soft supersymmetry-breaking scalar (sfermion and Higgs boson) masses m_0, gaugino masses $m_{1/2}$ and trilinear couplings A_0 are each assumed to be universal at the Grand Unification Scale. The 105 free parameters are thus reduced to five (four continuous and one sign) in this scenario:

$$m_0, m_{1/2}, A_0, \tan(\beta), sign(\mu)$$

where $\tan(\beta)$ is the ratio of the vacuum expectation values of the two Higgs fields and μ is the higgsino mass parameter.

These parameters are constrained by many experiments, including supersymmetric particle searches at collider experiments [47], rare B decays [36], the measurement of the anomalous magnetic moment of the muon [18], and the relic dark matter Ω_{DM} measurement from WMAP and other cosmological data taking [42] [44]. A set of benchmark scenarios in the framework of the mSUGRA , taking into account all the constraints mentioned above, was proposed by Battaglia et.al [17]. These benchmarks (see Table 2.3) allow clear comparison of many different experimental results. In my analysis I follow them to survey the dark matter parameter space.

2.4   DM Search Methods

Many methods have been proposed to search for WIMPs. These include experiments which hope to measure the recoil of dark matter particles elastically scattering off of nuclei (direct searches) [28], experiments such as AMS01, which hope to observe the

Model	A	B	C	D	E	F	G	H	I	J	K	L	M
$m_{1/2}$	600	250	400	525	300	1000	375	935	350	750	1300	450	1840
m_0	120	60	85	110	1530	3450	115	245	175	285	1000	300	1100
$\tan\beta$	5	10	10	10	10	10	20	20	35	35	35	50	50
$sign(\mu)$	+	+	+	−	+	+	+	+	+	+	−	+	+
m_t	175	175	175	175	171	171	175	175	175	175	175	175	175
χ mass	252	98	163	220	115	430	153	402	143	320	573	187	821

Table 2.3: Post-WMAP cMSSM benchmark parameters sets proposed in [17]. $m_0, m_{1/2}, m_t$ and χ are in units of GeV. A_0 is assumed to be zero for all scenarios.

products of dark matter annihilations (indirect searches), and collider experiments [15] which hope to produce DM particles. Indirect searches include searches for neutrinos [34], gamma-rays [50], and charged final states [16] [27]. The fluxes of these annihilation final states are proportional to the annihilation rate, which in turn depends on the square of the dark matter density. Neutralino annihilation produces the same amount of electrons and positrons, protons and antiprotons respectively. Positrons and antiprotons, however, have low background from known astrophysical sources. Therefore, they are better channels than electrons and protons for dark matter search. However, in practice, it is highly challenging to measure the positron or antiproton energy spectrum accurately. The challenge mainly comes from distinguishing positrons from protons, knowing that the abundance of protons in cosmic rays is about 10^4 times of that of positrons, so even a 10^{-4} leakage of protons in positrons would mess up the positron spectrum completely. The same reasoning also applies to antiprotons. AMS01 positron ID was limited to a momentum range of up to about 3 GeV due to the Cerenkov limit [5]. Thus electron channel is chosen instead for the analysis. An upper limit on the dark matter annihilation rate can be set by requiring that the associated electron emission does not exceed the observed flux.

2.4.1 DM Search w/ AMS01

Electrons and positrons can be produced in a variety of dark matter annihilation modes. For example, annihilations to ZZ or W^+W^- can produce electrons and positrons with energy of $m_\chi/2$. A continuum of electrons and positrons, extending to much lower energies, can be produced in the cascades of annihilation products such as heavy leptons, heavy quarks, Higgs bosons and gauge bosons. The spectrum of electrons or positrons produced in dark matter annihilations significantly depends on the annihilation modes, which directly associate to the supersymmetric scenario used to construct the neutralino.

Electrons and positrons move under the influence of the galactic magnetic fields, thus they will loose memory of their origin. Diffusion is usually employed to model this transport process. We need to take into account the annihilations within a spherical volume centered at the observer (the Earth) and with radius equal to the propagation length of the electron. The modeling of such propagation in galaxy is discussed in detail in the next chapter. Figure 2-2 shows the energy loss time-scales of nucleons
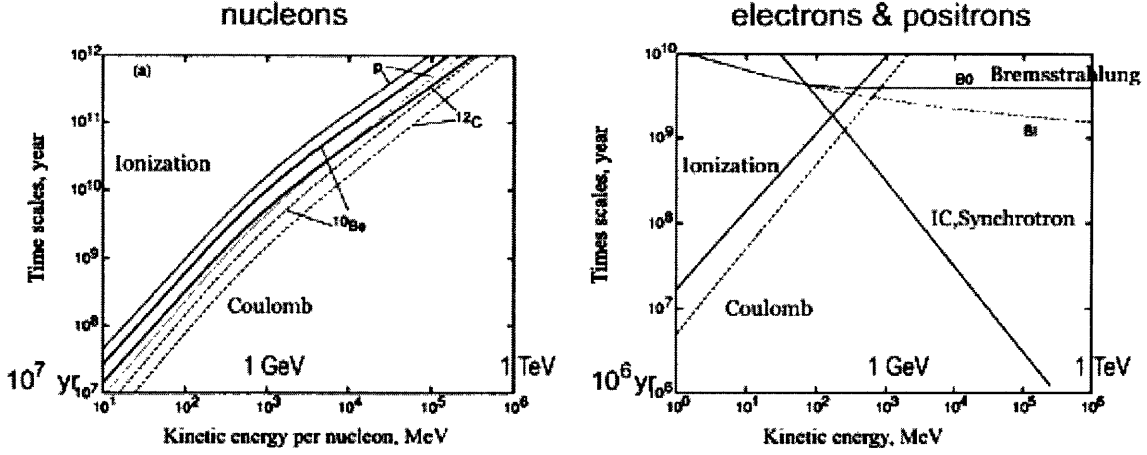
Figure 2-2: The left panel, time scales of energy loss for nucleons in the interstellar matter; the right panel: for electrons and positrons.

(left) and electrons and positrons (right) via various mechanisms in the interstellar matter [62]. Mainly resulting from the inverse Compton scattering on both starlight and the cosmic microwave background and Synchrotron radiation, it takes about 100 million years for the energy of an electron to drop from 100 GeV to 1 GeV. 1 GeV is approximately the minimum energy of our detection range. The diffusion coefficient D is typically 10^{28} cm^{2}sec^{-1} [62], thus the propagation length of the electron is $\sqrt{D\tau} \approx 3$ kpc. The lifetime of antiprotons is about 5 orders of magnitude greater than that of electrons, resulting 2 to 3 orders of magnitude greater in their propagation length. Therefore, electrons detected by AMS01 have their origins within 3kpc of Earth, while anitprotons originate from the whole Galactic halo.

2.5 Substructure of DM Distribution

There are reasons to believe that the dark matter distribution in the Galactic halo is not smooth. The existence of "clumps" is a common feature of N-body simulations. There are theoretical arguments to support this result. For instance, initial density fluctuations after the Big Bang are expected to produce clumps of dark matter at all scales [22]. If cosmic strings or other defects exist, they may seed the formation of density-enhanced dark matter clumps [41]. Also, we know that the Galaxy has consumed smaller dwarf galaxies that have dark matter. The should produce anisotropies in DM distribution in the Milky Way [1].

The electron flux from neutralino annihilation could be enhanced by the substructures in the galactic halo. If we assume we are averaging over a volume l^3 where l is the electron propagation length, containing many small clumps, which have scales much smaller than the propagation length of electrons, we can define an enhancement factor, which is called the boost factor. The boost factor, B, is defined as the ratio of the average of the squared density of dark matter with a clumpy distribution to that with a smooth isothermal distribution, $B = <\rho^2>_{clumpy} / <\rho^2>_{iso}$. It

can satisfy self-consistency to introduce a boost factor for electron and positron flux because there is actually freedom to have clumpy distribution models to accommodate electron and positron flux while still producing the right Galactic rotation curve and will not overproduce other annihilation products, such as antiprotons, neutrinos and gamma rays. The electron flux from annihilation scales as $< \rho^2 >$, while the rotation curve depends on $< \rho >$. Figure 2-3 is a simple example to illustrate that $< \rho^2 >$ could be enhanced while $< \rho >$ remains the same when the distribution becomes inhomogeneous. Because the propagation of electrons or positrons, antiprotons, neutrinos and gamma rays are not the same, the boost factors for them are not necessarily the same. Gamma rays and neutrinos are charge neutral and they don't interact with the galactic magnetic fields, so their fluxes are obtained by integrating along the line-of-sight connecting the Earth and the source. For antiprotons, they are similar to the case of electrons and positrons in terms of integrating over a volume. However, a nearby clump would serve to increase the electron and positron flux more than it would increase the antiproton flux, as electrons and positrons have shorter propagation length (roughly several kpc) than that of antiprotons because of their rapid energy loss [20].

In 1994 and 1995, the High Energy Antimatter Telescope (HEAT) observed a flux of cosmic positrons well in excess of the predicted rate from astrophysical sources. The energy spectrum peaked at 10 GeV and extended to higher energies [16]. Such an enhancement could be explained by a clumpy dark matter halo with boost factor (from several tens to ten thousands, vary as SUSY models) [12].
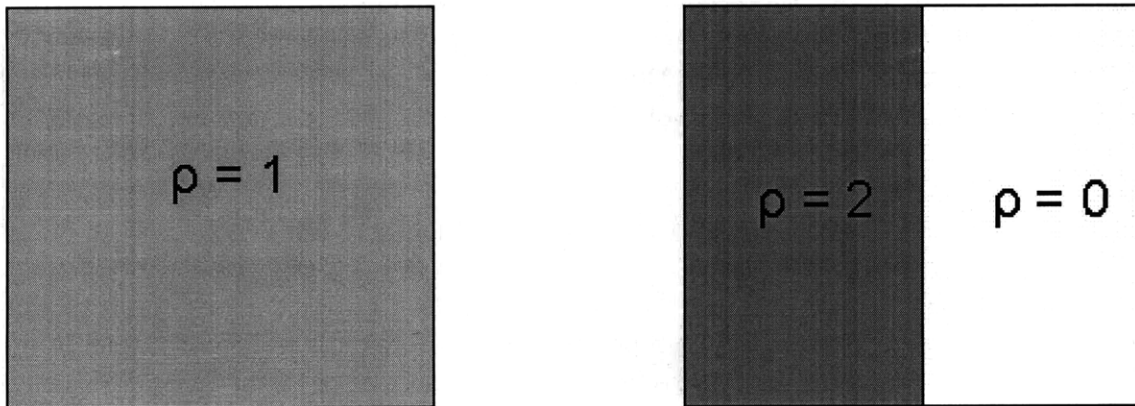

Figure 2-3: In the left panel, the density distribution is homogenous over the whole unit area, thus $< \rho >= 1$, $< \rho^2 >= 1$; In the right panel, all matter concentrates on the left half of the unit area, thus $< \rho >= 1$, $< \rho^2 >= 2$, so the boost for this case is 2.

Chapter 3

Cosmic Rays

3.1 Overview of the Galactic Cosmic Rays

The cosmic rays incident at the top of the terrestrial atmosphere include all stable charged particles and nuclei. There are magnetic fields in the galaxy, which is on the order of 10^{-7} Gauss. A charged particle moving in the magnetic field executes a helical path. Using the relation between the momentum P, magnetic field B and gyroradius r_g,

$$p_\perp(MeV/c) = 3 \times 10^{-4} Br_g(Gauss \cdot cm)$$

a 10^{14} eV/c proton would have a radius of 3×10^{18} cm, or 1pc. This is much smaller than the typical scale of a galaxy, which is about 10 kpc. Therefore, cosmic rays below this energy can be seen to conduct a random walk and are confined by the magnetic fields in the galaxy. Even though they have no memory of their origins when they reach the Earth, they are of Galactic origin. This leads to the assumption of a steady state condition on a galactic scale. The renewal of the cosmic rays requires an average energy input to compensate for the loss of nuclei by nuclear and electronic collisions or escape from the galaxy. The lifetime of the confinement in the interstellar magnetic field is $\sim 10^7$ yr, as measured by the surviving fraction of the radioactive secondary nuclei Be^{10} [58]. If we take the galactic radius as 10 kpc, we have a volume of 10^{68} cm^3. The energy density of cosmic rays is about 1 eV/cm^3. Therefore, the energy production rate in cosmic rays should be $1eV/cm^3 \times 10^{68}cm^3 \div 10^7yr \sim 10^{42}erg/sec$. The explosion energy of a supernovae is about 10^{51} erg and the event rate is about once per 100 years. Thus the energy production rate matches the required renewal rate of the cosmic rays estimated above. Therefore, it is commonly believed that supernovae remnants is a principal mechanism for generating and accelerating cosmic rays, which is also supported by many arguments based on the chemical patterns [58].

"Primary" cosmic rays are those particles accelerated at astrophysical sources and "secondaries" are those particles produced in the interaction of the primaries with the interstellar matter. Electrons, protons, helium nuclei, as well as carbon, oxygen, iron and other nuclei synthesized in stars, are primaries. Nuclei such as lithium, beryllium, boron, which have low binding energy and thus would be destroyed during stellar burning process, are secondaries. Figure 3-1 shows the comparison of the chemical
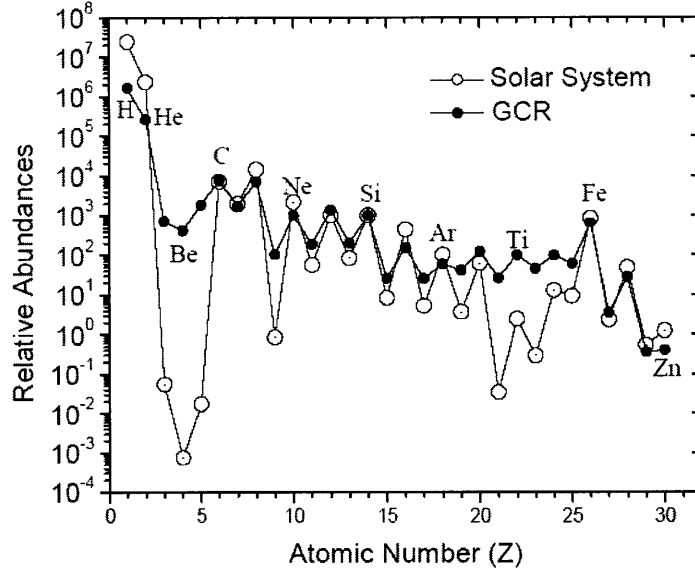
Figure 3-1: Comparison of the chemical distributions in the Solar System and in the cosmic rays. The Solar System abundances in the figure represent the abundances of elements in the proto-solar nebula. [48]

distributions in the stars and in the cosmic rays. The most dramatic difference is a six orders of magnitude enrichment in the cosmic ray abundances for the elements LiBeB, which indicates that these light elements were born mainly during the course of propagation.

The energy distribution of cosmic rays from several GeV to 100 TeV is smooth, with a power-law distribution [54]. The energy spectra of several components of cosmic rays are shown in Figure 3-2. Fermi acceleration [30] by the supernovae shocks can naturally yield a power-law structure. The propagation is a diffusion process, which will largely preserve the power-law nature, although the index may change. The modeling of propagation is discussed in more detail in Section 3.2. The roll over at lower energy results from solar modulation, which is discussed in Section 3.3.

3.2 Propagation of the Cosmic Ray Nuclei in the Galaxy

3.2.1 Cosmic Ray Propagation Model

Diffusion theory is often employed to describe the large-scale galactic propagation of the cosmic rays. The cosmic rays move in spiral trajectories around the galactic magnetic fields with gyroradii determined by the particle energy. The collision against the irregularities and moving magnetic fields diffuse the cosmic rays [30] [58]. This provides the mechanism of the confinement and acceleration of the cosmic rays in

20
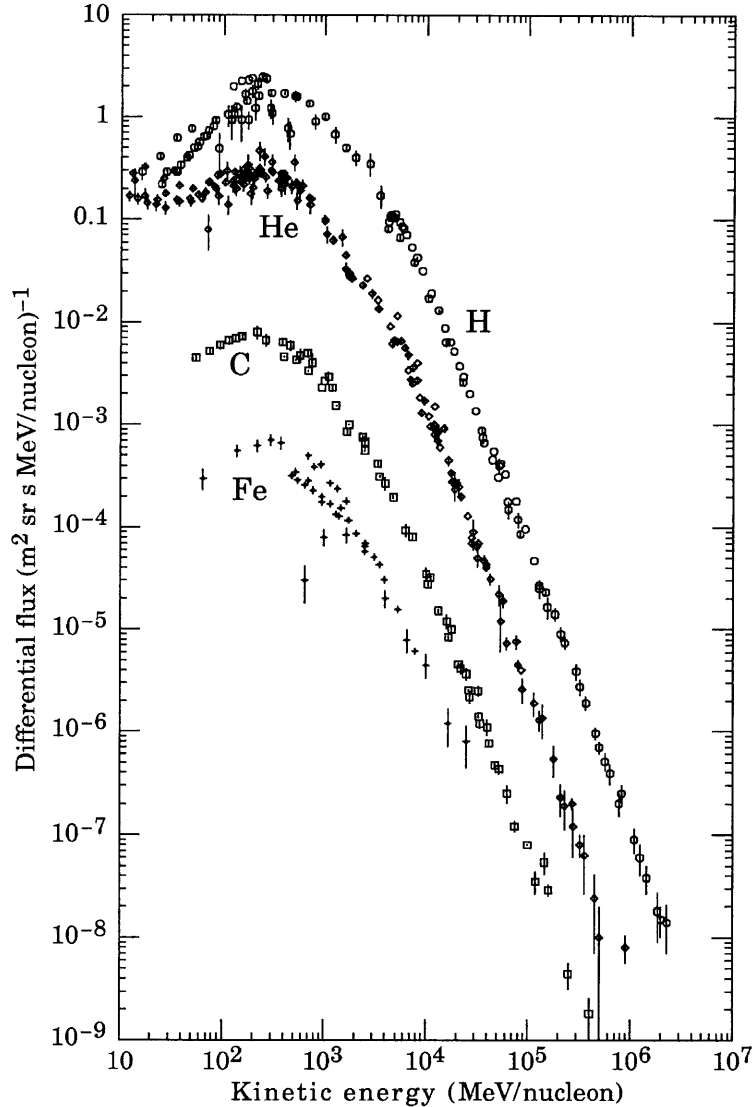
Figure 3-2: Cosmic ray nuclei spectra, from PDG Cosmic Rays, T.K. Gaisser and T. Stanev.[54]

the Galaxy. The moving magnetic fields are known as Alfven waves [8]. The velocity Alfven waves propagate along the Galactic magnetic field is called Alfven velocity v_A, which can be estimated as $v_A = B/\rho^{1/2}$ [8], where ρ is the interstellar matter density. For more details see Appendix A. ρ is 1 proton/cm^3, and B is 10^{-7} Gauss, thus v_A is 20 km/sec. Cosmic ray particles gain energy from head-on collisions with Alfven waves and lose energy from overtaking collisions. The head-on collisions happen more frequently than overtaking collisions due to the greater relative velocity, which results in an average net gain. Thus scattering by Alfven waves provides a mechanism of cosmic ray reacceleration.

We consider the propagation of cosmic rays in the interstellar medium with ran-

dom hydromagnetic waves. The transport equation has the following form [62]:

$$\frac{\partial}{\partial t}\Psi(\vec{r},p,t) = q(\vec{r},p)+\vec{\bigtriangledown}\cdot[D_{xx}\vec{\bigtriangledown}\Psi-\vec{V}\Psi]+\frac{\partial}{\partial p}[p^2 D_{pp}\frac{\partial}{\partial p}\frac{\Psi(p)}{p^2}]-\frac{\partial}{\partial p}[(\frac{dp}{dt}-\frac{1}{3}p\vec{\bigtriangledown}\cdot\vec{V})\Psi]-\frac{\Psi}{\tau_f}-\frac{\Psi}{\tau_r}$$

$$(3.1)$$

where Ψ is the density per unit of total particle momentum, $\Psi(p)dp = 4\pi p^2 f(\vec{p})$ in terms of phase-space density $f(\vec{p})$. $q(\vec{r},p)$ is the source term, including the primary particles injected from supernovae remnants and the secondary particles produced during the course of propagation. The time interval between supernovae explosions in galaxy is much smaller than the lifetime of cosmic rays, so supernovae explosion can be seen as a continuous process, which adds source constantly into cosmic rays. Therefore, the source term $q(\vec{r},p)$ is not a function of time. The radial distribution of the sources is chosen to reproduce the cosmic-ray distribution deduced from EGRET > 100 MeV gamma rays [61]. The injection spectrum is assumed to be a power law in energy resulting from Fermi acceleration. D_{xx} is the spatial diffusion coefficient. $\vec{V}$ is the advection velocity, which is assumed to be in the direction perpendicular to the galactic plane only and increases linearly with the distance from the plane [66]. Reacceleration is described as diffusion in momentum space and is determined by the coefficient D_{pp}. Various losses are also taken into account, including momentum loss, fragmentation and radioactive decay with time scale tau_f and τ_r respectively.

We use the software package GALPROP [62], which solves this transport equation numerically given a source distribution and a free escape boundary condition, to perform the propagation calculation. The model assumes a cylindrical shape of the galaxy with a radius of about 20 kpc and the total height of several kpc. The primary sources are distributed in a thin disk about the galactic mid-plane having characteristic thickness of 200 pc.

Modeling galactic propagation of cosmic rays is a very complicated task. The major sources of the uncertainties are fourfold: (1) primary source distribution and the interstellar matter distribution; (2) cross sections for secondary cosmic ray production, annihilation and scattering; (3) galactic propagation models and parameters; (4) solar modulations. The uncertainty we try to investigate is from (3), while for the other three, we use the values to the best of our knowledge. See Ref. [62] [51] for more details for (1) and (2). The solar modulation is discussed later in this chapter.

3.2.2 B/C — A Probe of the Propagation Model

Secondary nuclei are produced by the interaction of primary nuclei with the interstellar medium during propagation. Therefore, their spectra carry the information of the propagation process. Taking the ratio of the secondaries to the primaries can largely cancel out the dependence on the injection spectra, leaving the quantity very sensitive on the variation of the propagation parameters. B/C is the best secondary-to-primary ratio for this purpose, not only because they are relatively well measured in cosmic rays, but also because the cross sections for the production of their secondaries are well known.

More energetic particles tend to escape from the galaxy faster. However, on the

other hand, particles of higher energy tend to be scattered with the magnetic fields more often, thus would spend more time in the system. The competition of these two mechanisms results in the shape of the B/C spectrum, which rises with energy at low energy but decreases at high energy. Therefore, the B/C ratio peaks at the energy where the dominant mechanism transitions from one to another.

Diffusion, reacceleration and advection are the three propagation mechanisms in the transport equation. Diffusion determines the overall height of the B/C spectrum, since the sooner the primaries escape from the galaxy, the fewer secondaries would be produced (see Figure 3-3).

The reacceleration, introduced by the moving magnetic fields, results in more frequent collisions. This changes the energy at which escape balances collisions. Thus, the Alfven velocity determines the peak position of the B/C spectrum (see Figure 3-4). Measurements indicated that the B/C spectrum peaks at 1 GeV/nucleon [62].

An outflow of material from the halo could carry the cosmic rays with it. This advection motion would affect the B/C spectrum. Advection is therefore adds a third mechanism that affects the escape time. The outward advection would speed up the escape of cosmic rays from the Galaxy. Thus advection would reduce the overall height of the B/C spectrum and shift its peak towards lower energy (see Figure 3-5).
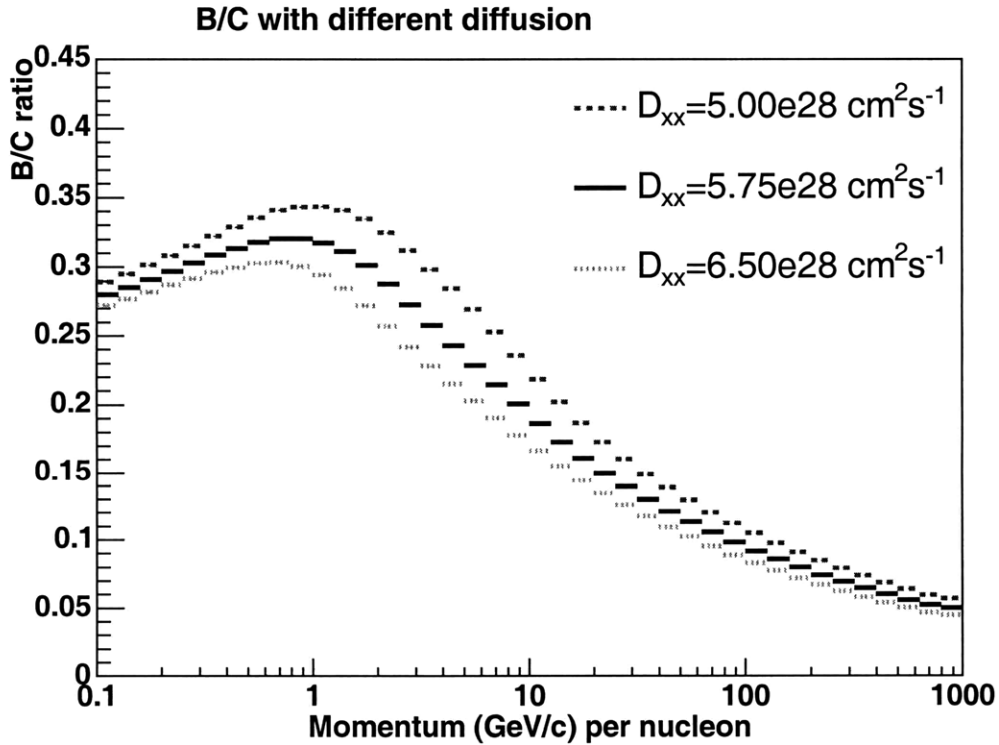
Figure 3-3: The effect of diffusion on B/C, as simulated by GALPROP

Although in principle, all three processes could be important, we only consider diffusion and reacceleration (DR model), since it is the minimum combination which can reproduce the key observation of B/C. The effect of advection on the B/C spectrum

B/C with different reacceleration
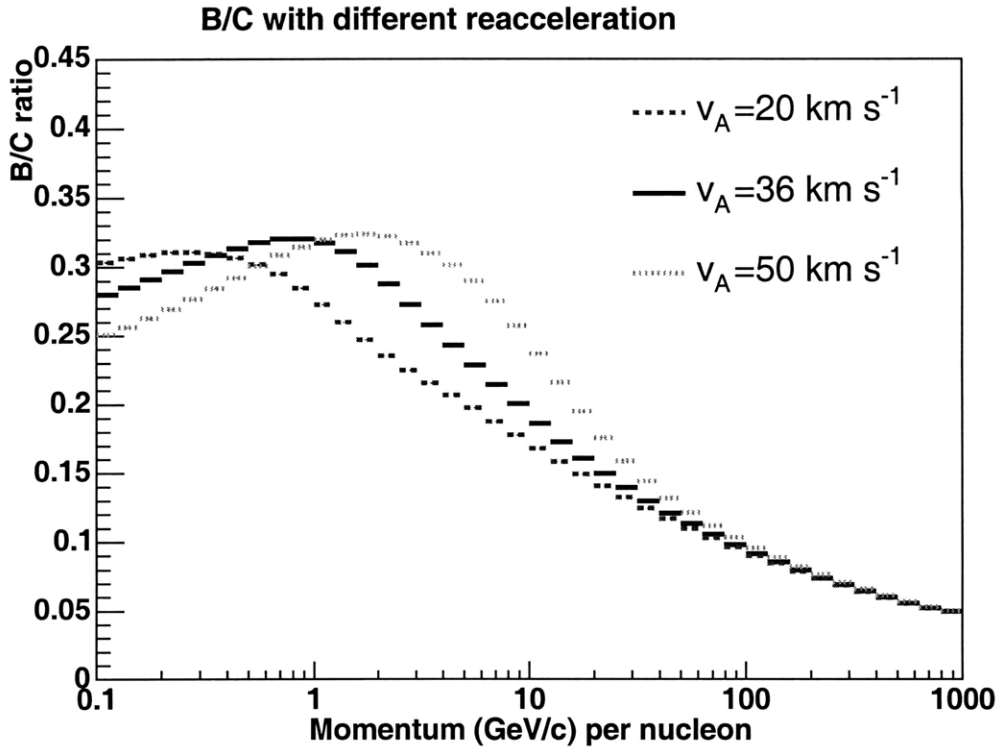
Figure 3-4: The effect of reacceleration on B/C, as simulated by GALPROP

B/C with different advection
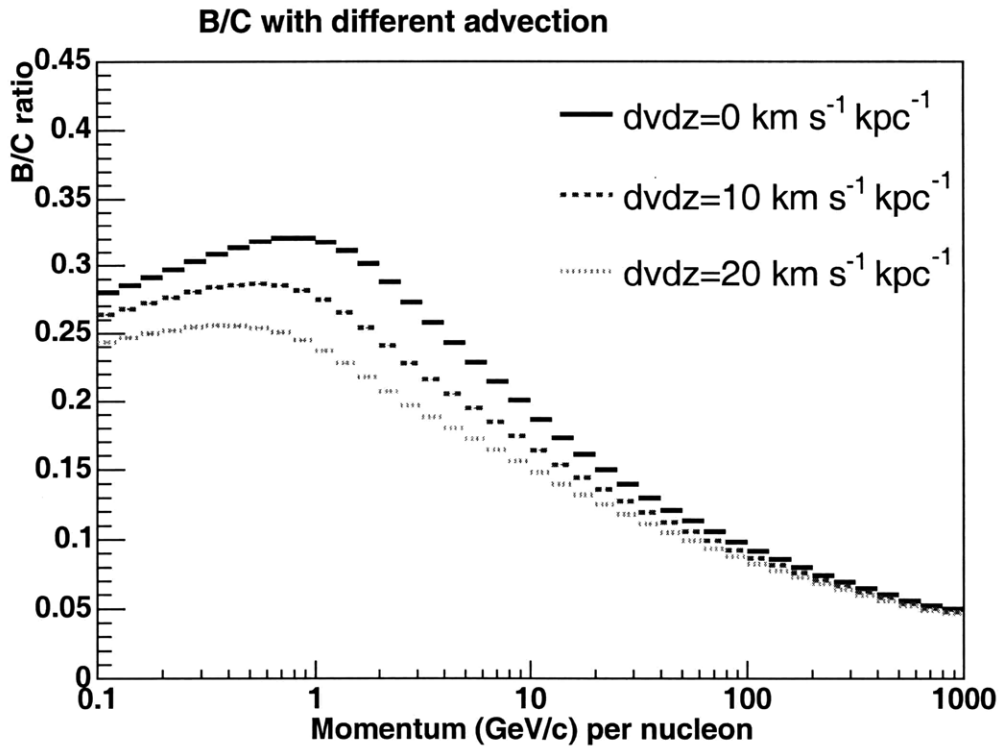
Figure 3-5: The effect of advection on B/C, as simulated by GALPROP.

can be produced by varying diffusion and reacceleration.

3.2.3 Propagation Parameters

The key parameters for diffusion and reacceleration are D_{xx} and D_{pp}, respectively. They can be derived from scattering with Alfven waves (see Equation (9) (10) in [57]). D_{xx} can be formulated as a power law in particle rigidity

$$D_{xx} = D_{xx0}\beta R^\delta$$

where $\beta = v/c, R = p/Z$. For Alfven waves with a Kolmogorov spectrum, $\delta = 1/3$ [57]. D_{pp} can be described by a simple approximation [62]:

$$D_{pp} = p^2 v_A/(9D_{xx})$$

where v_A is Alfven velocity. Therefore, D_{xx0} and v_A are the key parameters in this framework. Due to the poor knowledge of the interstellar medium and the lack of direct measurement for these parameters, their values must be obtained from fitting the cosmic ray data. One major accomplishment of this work is to constrain D_{xx0} and v_A from AMS01 measurements of the B/C spectrum.

3.3 Solar Modulation and Geomagnetic Effects

The cosmic rays are modulated by the solar wind, the expanding magnetized plasma generated by the Sun, which decelerates and partially excludes the lower energy particles from the inner solar system. We make use of the forced field approximation suggested by Gleeson and Axford (1968) [31].

$$J(r, E) = \frac{E^2 - E_0^2}{(E + |q|\Phi)^2 - E_0^2} J(r_\infty, E + |q|\Phi) \qquad (3.2)$$

where $J(r, E)$ is the differential flux of cosmic ray, r is the distance from the Earth, E is the total energy of the particle, E_0 is the rest energy of the particle. This model is characterized by one parameter Φ, which can be interpreted as the energy loss of the cosmic-ray particle when approaching the Earth from infinity. $\Phi = |Z|e\phi$, where ϕ is the potential for unit charged particles. During AMS01 flight, $\phi \approx 0.58 GV$ [55].

Cosmic rays are also affected by the Earth's magnetic field. Low energy particles from outer space cannot penetrate through except at high latitude. Therefore, the events observed by AMS01 with energy lower than some limit would most likely be those trapped by the Earth magnetic field, not from cosmic origin. With a displaced dipole assumption of the Earths magnetic field, the lowest momentum accessible to our detector in low Earth orbit is given by [24]:

$$\frac{p}{|Z|} = \frac{59.6[GeV/c^2]\cos^4\lambda}{(1 + (1 - Q\cos\theta\cos^3\lambda)^{1/2})^2} \qquad (3.3)$$

where λ is the latitude of the detector, θ is the east-west component of the zenith angle of the incident trajectory. We take care of this geomagnetic cutoff effect in the exposure time.

Chapter 4

AMS Experiment

The AMS01 experiment was a magnetic spectrometer designed to measure cosmic rays from several hundred MeV to about 300 GeV, which was a prototype of the future experiment AMS02. It flew on Space Shuttle Discovery mission STS-91 in 1998 for 10 days and recorded about 100 million events. In this chapter, section 4.1 is briefly describe each component of the detector. A quick review of the flight is given in section 4.2. For detail information of AMS01, please refer to [6].

4.1 The AMS01 Detector

AMS01 detector mainly consisted of a permanent magnet, a Time of Flight system (TOF), a silicon tracker, an Aerogel Threshold Cerenkov Counter (ATC), and an Anti-Coincidence Counter (ACC). A schematic of the detector is shown in Figure 4-1. I mainly use the information from the TOF and the Tracker for my analysis.

4.1.1 The Magnet

The design of the magnet should maximize the bending power while keeping the magnet dipole and flux leakage small so not to add unwanted torques to the space shuttle or to affect the electronics. A cylindrical permanent magnet design, constructed of high grade magnetic Nd-Fe-B blocks, was chosen, which had a length of 800mm, and an acceptance of 0.82 m^2 sr [6]. With a clever arrangement of the magnetic building blocks, most of the magnetic flux was returned via the magnetic blocks, reducing the flux leakage and the dipole moment to acceptable levels. The magnet provided a bending power of 0.15 T m^2.

4.1.2 TOF

The time of flight (TOF) had four layers. Two layers formed a double-plane on top of the magnet, orientated orthogonal to each other to obtain a two-dimensional measurement. The other two formed a double-plane in the same way below the magnet. A double plane assembly is shown in Figure 4-2. Each layer consisted of
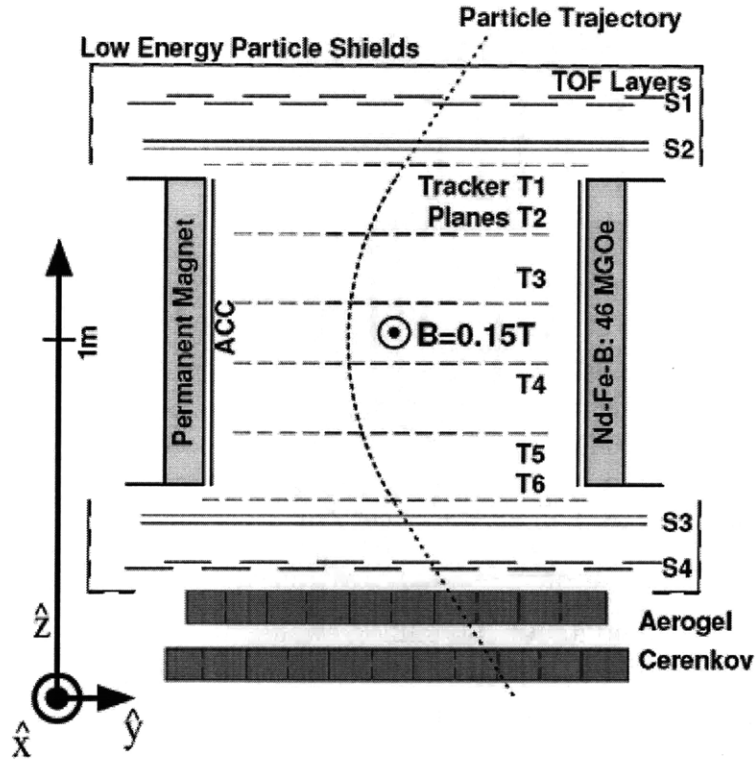
Figure 4-1: The schematic of AMS01 detector

14 scintillator paddles of 10mm thickness, 110mm width and various lengths ranging from 720 to 1360mm. Three photomultiplier tubes were attached at each end of the paddle.

TOF determined two quantities, which were the traversing time of a particle through the detector, and the direction of the particle, whether it was going upwards or downwards. It also provided the fast trigger and a rough charge measurement and trajectory reconstruction.

The time resolution of TOF was better than 120ps which resulted in a position resolution of better than 2 cm along the paddle, and a velocity resolution of $\sim 3\%$. A highly relativistic ($\beta = 1$) particle would take 5 ns to traverse the TOF system, therefore the upward and downward going particle separation was expected to be 1 in 10^{11} [11]. More information of TOF can be found in Ref.[11] [9].

4.1.3 Tracker

The tracker had six layers. Each layer consisted of ladders made of seven to fifteen double-sided silicon microstrip sensors with dimension $40.14 \times 72.04 \times 0.30$ mm^3. Figure 4-3 is an exploded view of the ladder. The sensors were read out from both sides, which ran perpendicular to each other. The S-side measured position in the bending plane with a pitch of 110 μm, and the K-side measured position in the non-bending plane with a pitch of 208 μm. The ladders were aligned parallel to
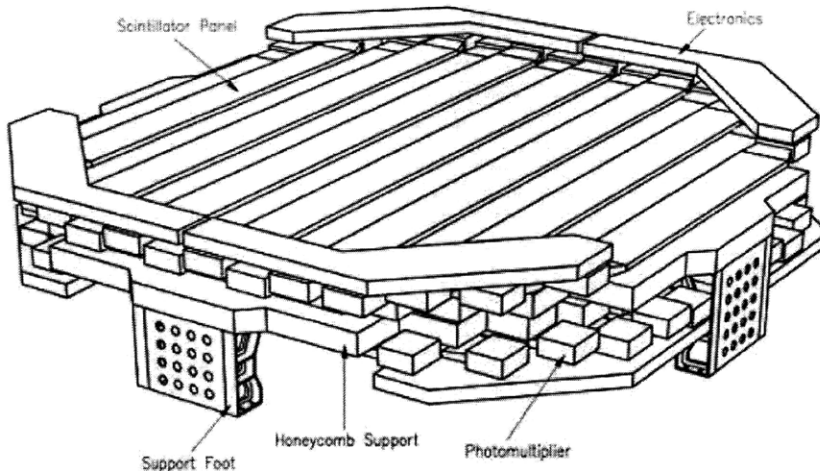
28

Figure 4-2: The schematic of a double-plane assembly of AMS01 TOF.

the magnetic field to maximize the position resolution in the bending plane. The materials in each plane corresponded to approximately 0.65% of a radiation length and $\sim 0.06\%$ of a nuclear interaction length.

The tracker provided a measurement of the rigidity and charge of a particle. It had a position resolution of about 10 micron in the bending plane and about 30 micron in the non-bending plane, which could be translated to a momentum resolution of 9% for protons of 10 GeV. It had a theoretical rigidity range of about 100 MV to 600 GV. However, multiple scattering (MS) in the silicon tracker material would introduce deviation in the particle tracks which should be considered in the error estimation. The mean change in the trajectory due to MS in the Gaussian approximation is given by [33]:

$$\theta_0 = \frac{13.6 MeV}{\beta cp} Z \sqrt{x/X_0}(1 + 0.038 ln(x/X_0))$$

where $p, \beta c$, and Z are the momentum, velocity and charge, and x/X_0 is the thickness of the scattering medium in radiation lengths. It is important to note that $\theta_0 \propto 1/\beta$, which means lower energy particles suffer bigger uncertainty from MS. Therefore in practice, our accessible energy region would be reduced by the multiple scatterings at low energy and low statistics at high energy.

A measurement of total energy loss in the tracker was used to determine the absolute charge of the particle passing through the tracker. A combined charge measurement of the TOF and tracker was estimated to be accurate to 1 in 10^7 in distinguishing Z=1 and Z=2 nuclei. Only tracker was used for charge measurement for higher charged nuclei ($Z > 2$), because the dynamic range of the TOF scintillator does not permit to distinguish such large charges with great accuracy. The tracker could provide good charge measurement for nuclei up to Oxygen. More information of tracker can be found in Ref.[7].
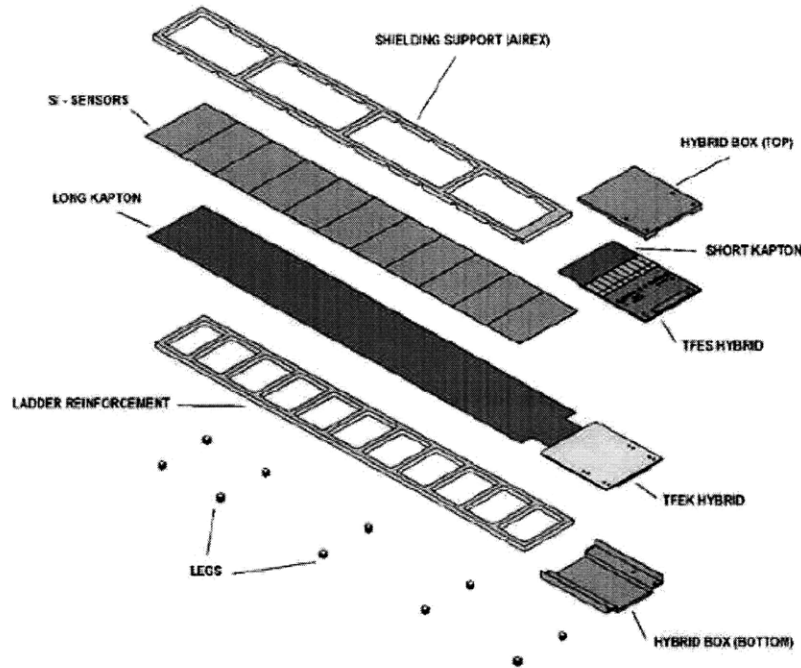
Figure 4-3: An exploded view of AMS01 tracker ladder.

4.1.4 The Aerogel Threshold Cerenkov Counter (ATC)

An ATC was installed underneath the lower TOF layer, which was used to increase the discrimination power between protons and positions below 3.5 GeV. Since it was not used in this analysis, for a detailed discussion on its design, construction and performance, please refer to Ref. [13] [14].

4.1.5 The Anti-Coincidence Counter (ACC)

16 anticoincidence scintillator counter paddles were arranged like barrel staves in the space between the inside wall of the magnet bore and the support shell of the tracker, which provided a tag for particles coming from aside. An event would be discarded if ACC fired since they were unlikely able to be well reconstructed.

4.2 The AMS01 Flight

4.2.1 Flight Parameters

The flight of AMS01 on board the Space Shuttle Discovery was from June 2 to June 12, 1998. An important parameter of the flight was called zenith angle, which was defined as shown in Figure 4-4. The zenith angle was the angle between the pointing direction of the detector and the line connecting the center of the Earth to the shuttle/AMS01. Therefore, a zenith angle of 0° means that AMS01 was pointing up right; a zenith
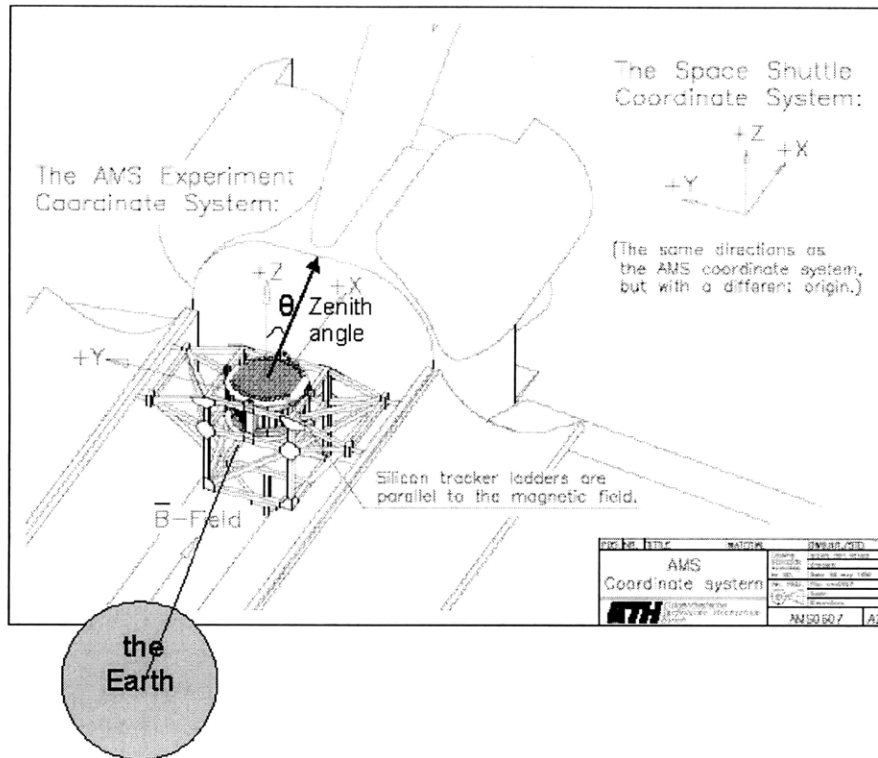
Figure 4-4: The definition of zenith angle.

angle of 180° means that it was pointing to the Earth.

As shown in 4-5, the data taking could be divided into 4 periods: 1. The 25 hours before docking with Mir with the zenith angle within 45°. 2. The four days during which Discovery was docked with Mir. 3. After the Mir undocking, 19, 25 and 20 hours with zenith angle of 0°, 20° and 45°, respectively. 4. Approximately 9 hours with zenith angle of 180° prior the descent of Discovery.

The zenith angle fluctuated quickly during period 2, which could be because that many particles might have interacted with the MIR before passing through the detector. We did not use the data from this period, but one can manage to reconstruct the layout of MIR seen by AMS01 from these data [35]. In period 4, AMS was facing towards the Earth. Because we are interested in those of cosmic origin, we do not use the data from this period either. Therefore only data taken from the first and the third periods are used in the analysis, which leads to roughly 94 hours of active data taking.

4.2.2 Trigger and Data Acquisition

There were three levels of the electronic trigger of AMS01: Fast, Level-1 and Level-3 [35]. The Fast trigger required coincident signals from the top and bottom TOF planes within $200\mu s$. Level 1 triggers required that ACC did not fire, and only specific combinations of the two outer TOF planes were acceptable to avoid particles hitting the unequipped parts of the tracker. Level 3 trigger required that at least 3 clusters

31
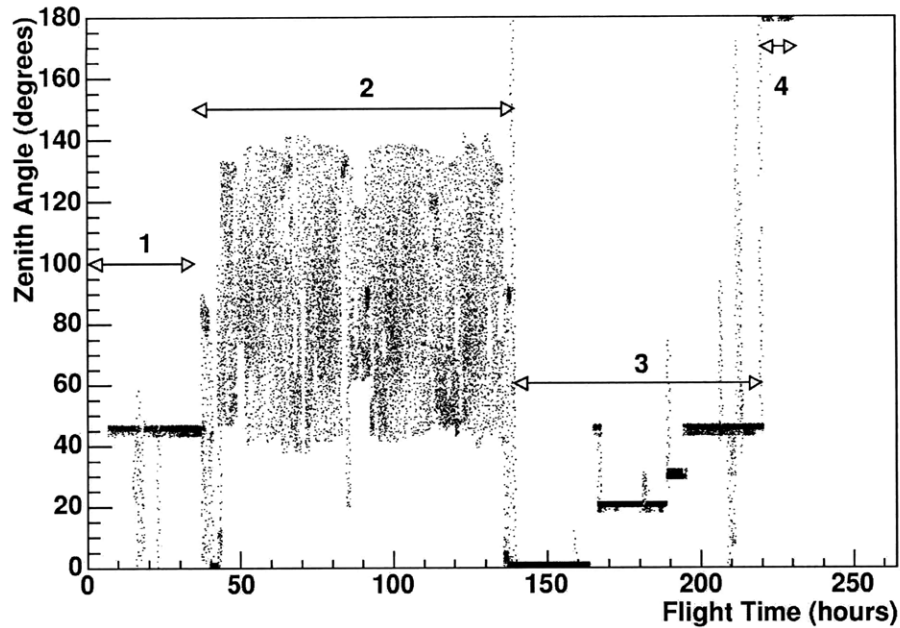
Figure 4-5: Zenith angle vs Flight time for AMS01 during Space Shuttle Discovery mission STS-91 in 1998.[24]

on 3 different tracker layers with signal-to-noise ratio above a certain level were along the expected particle trajectory.

During the flight, events passing all three levels of triggers were recorded. A set of events that triggered only the fast trigger were recorded for trigger efficiency studies. These events constituted about 0.1% of the total dataset and were known as prescaled events. The trigger rate varied between 100 Hz and 1600 Hz depending on magnetic latitude. The detector was saturated when the shuttle was in the South Atlantic Anomaly (SAA) where the trigger rate spiked to almost 20k Hz [5]. This extremely high particle flux is because of the extremely weak geomagnetic fields of this region. The detector lifetime has to be considered during the efficiency calculation by dividing the count rate with the corresponding lifetime. Since the lifetime during SAA was zero, data taken during this period were discarded.

Chapter 5

WIMP annihilation signal search procedure

This chapter outlines the procedure to prepare major ingredients needed for the search of WIMP annihilation in AMS01 Z=-1 data, based on Ref. [55]. Section 5.1 reviews how to produce the momentum spectrum of negative unit charge particle from detector data. Signal production from neutralino annihilation is described in Section 5.2.

5.1 AMS01 Z=-1 Momentum Spectrum

5.1.1 Data Selection

Charged particles deposit energy in the TOF and tracker layers when traversing the detector. This allows for the reconstruction of the particle tracks. Because charged particles are bent by the magnetic field, the radius of the track allows for the determination of the momentum per charge of the particle, which is defined as rigidity.

Preselection cuts are applied to clean up the data set. There are three categories of such cuts which are summarized as the following:

1. To make sure events are of cosmic origin, events are discarded if:

   - they pass from the bottom to the top or through the side (ACC fired);

   - their zenith angle is larger than 50 degrees;

   - their energy is smaller than the geomagnetic cutoff (see Equation 3.2).

2. To remove poorly measured data, events are discarded if they have:

   - no reconstructed particle track;

   - fewer than 4 tracker hits or fewer than 3 TOF hits;

   - different signs between the rigidities as reconstructed from the upper 3 layers and the lower 3 layers of the tracker;

- different charges as measured by the tracker and the TOF.

3. To avoid detector errors, events were discarded if:

   - taken during the time when the detector was at the South Atlantic Anomaly;

   - detector lifetime less than 35%.

Because the trajectory through the detector for very high energy particles is almost a straight line, and the content of protons in the cosmic rays is about 1000 times that of electrons, a major background for electron events of high energy comes from mis-identified protons. Therefore, other cuts are applied to preserve as many electrons as possible while removing the background protons. Two cuts, CircularCorrection and Half rigidity difference [55], could serve for this purpose efficiently. CircularCorrecttion requires the rigidities reconstructed from a simple fit of a circular track and from the FastFit algorithm [7] which accounts for magnetic field inhomogeneities and multiple scattering not to be too different. Half rigidity difference cut requires the rigidities constructed using the upper 3 and lower 3 layers of the tracker respectively not too different. The cutting criteria were determined by maximizing the electron to mis-identified proton ratio generated by Monte Carlo.

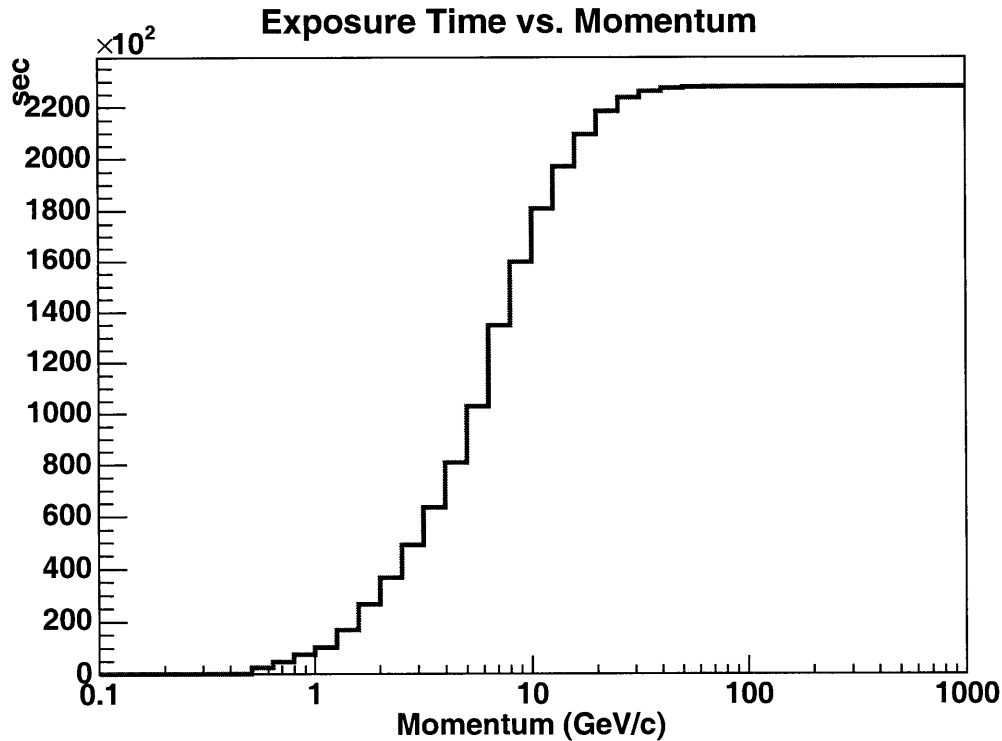After the cuts, 6,563,097 events are identified as Z=1 particles, and 74,216 events are identified as Z=-1 particles.

Figure 5-1: Exposure time for protons and electrons.

5.1.2 Exposure Time

The number of counts in each momentum bin must be turned into count rate by dividing by the exposure time. As mentioned in Section 3.3, the Earth's magnetic field sets a momentum cutoff which varies as a function of the latitude, particle incoming direction and charge. Therefore, a particle directly from outer space with certain momentum can only be seen by AMS01 in a certain region during the flight where its momentum is larger than the geomagnetic cutoff. The summation of time during which AMS01 took data within this region is the exposure time for this momentum bin. Particles with higher momentum have larger exposure time because their momentum is higher than the geomagnetic cutoff over a wider range of latitudes. Because the geomagnetic cutoff depends only on momentum and the magnitude of particle charge, the exposure time as a function of momentum for protons and electrons is the same, as shown in Figure 5-1.

5.1.3 Acceptance

Monte Carlo techniques [63] are used to simulate the gathering power and resolution of AMS01, producing the acceptance matrices, which translate the cosmic ray flux ($cm^{-2}sr^{-1}sec^{-1}$) to the count rate (sec^{-1}) in the detector. The Monte Carlo events are generated over a rectangle (250 cm×90 cm), 100 cm above the detector and are run through the analysis chain as real data. The matrix element (P_{rec}, P_{gen}) is the probability of a particle coming from space with momentum P_{gen} detected at momentum P_{rec}. The matrix elements have unit of cm^2 sr, which come from multiplying by the event generating phase space, which is the rectangle area. The acceptance matrices for protons and electrons are shown in Figure 5-2 [55]. Panel (a) is the matrix of Monte Carlo protons detected with correct sign charge. It is also used as an approximation of the acceptance of antiprotons recorded as antiprotons. Panel (b) is the matrix of Monte Carlo protons recorded as electrons, which is used to calculate the misidentified proton rate from proton background.

Both systematic and statistic uncertainties are considered in the acceptance matrix. By comparing with the pre-scaled events, it is found that the simulation is over efficient by 13±3.5 % [5]. Therefore, the count rate in Monte Carlo is reduced by 13% and a systematic error of 3.5% is set. The statistic error assumes poisson statistics. If the counts is N, the uncertainty is of $\sqrt{N}$.

5.1.4 Background Fit

As shown in the Monte Carlo simulation, high momentum protons are often misidentified as high momentum electrons, and vice versa. Because protons outnumber electrons by a factor of 1,000, misidentified electrons only add a very small fraction to the proton spectrum while misidentified protons are a significant background of electrons.

GALPROP predicts the cosmic ray backgrounds given the particle injection spectrum and the propagation model. The injection spectra of proton and electron are assumed to have a power law in energy $NE^{-\gamma}$. The normalization and the index are
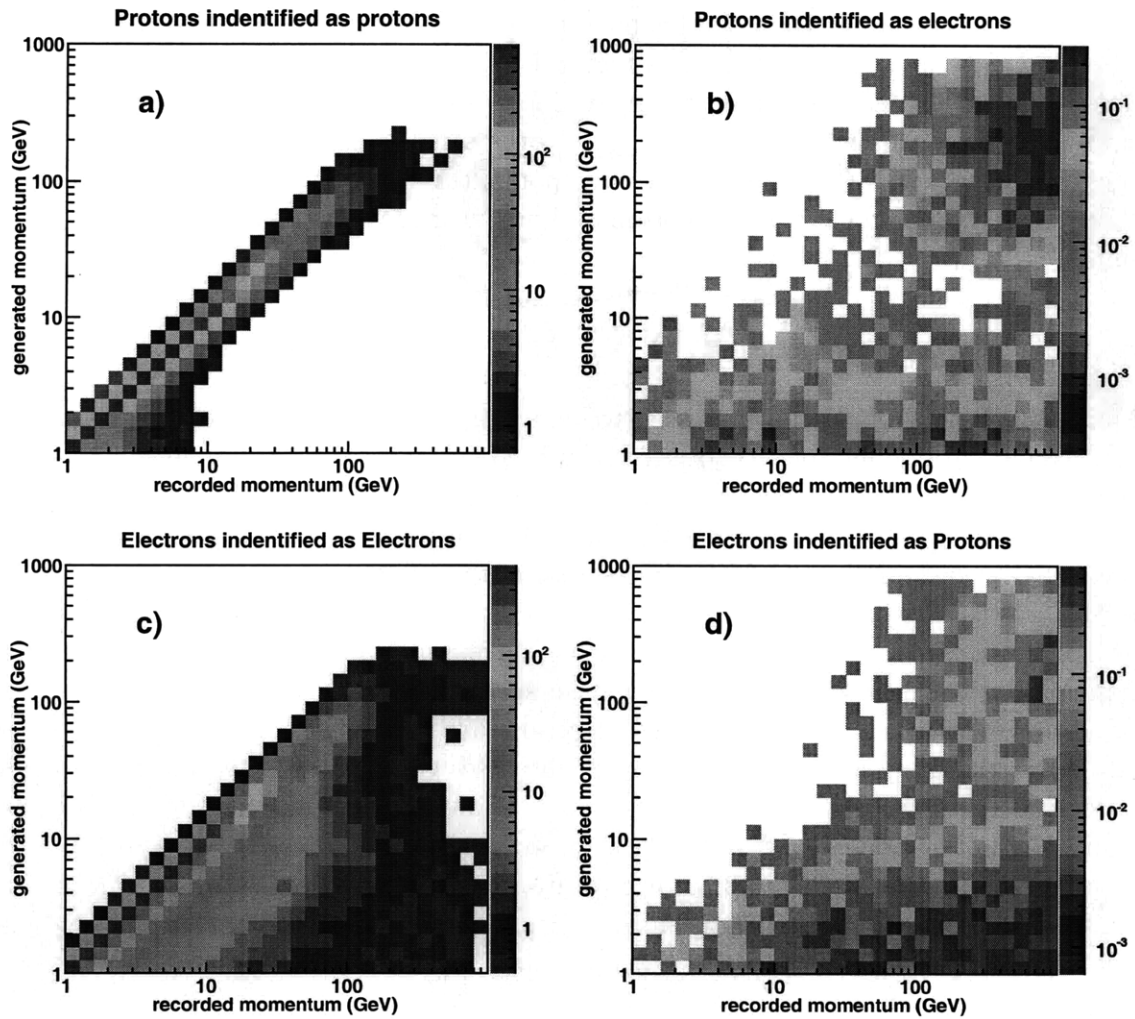
35

Figure 5-2: AMS01 acceptance matrices for electrons and protons [55]. Particles detected with the correct sign charge are also mostly detected with the correct momentum, as shown in panel (a) and (c). High momentum protons are often misidentified as high momentum electrons, as shown in panel (b).
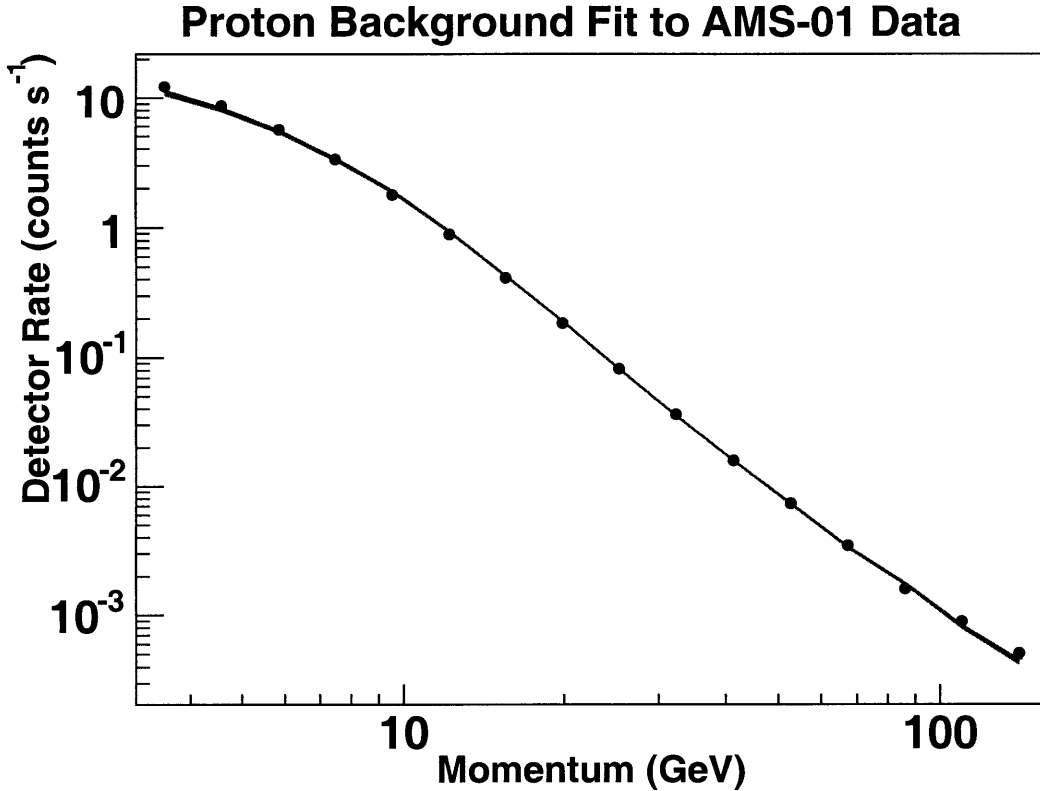
Proton Background Fit to AMS-01 Data

Figure 5-3: Proton background fit to AMS data [55].

left as free parameters in the fit. The diffusive reacceleration propagation model with default parameters setting (see Appendix C) is employed.

All Z=1 events are assumed to be background cosmic ray protons. The spectrum generated by GALPROP, modulated by solar modulation and multiplied by proton-to-proton acceptance (Figure 5-2 panel (a)), is fit to our Z=1 data. The fit yields a normalization of 0.67 ± 0.02, as a fraction of the initial GALPROP normalization, and an injection index of 2.43 ± 0.01 with $\chi_2/N = 7.98$ ($N = 13$) [55] (Figure 5-3).

We then perform the background fit to Z=-1 data, assuming no dark matter signal. There are two main components. One is the misidentified protons, which can be calculated using the resultant proton background and the proton-to-electron acceptance matrix (Figure 5-2 panel (b)). It is kept fixed in the fit. The other is cosmic ray background electrons, which is treated in the same way as that for protons. The fit yields a normalization of 0.70 ± 0.04 and an injection index of 2.70 ± 0.04 with $\chi_2/N = 2.04$ ($N = 13$) [55] (Figure 5-4). In principle, Z=-1 data should include antiprotons. However, it should be safe to ignore this in the fit because the abundance of antiprotons in cosmic rays is tiny compared to that of electrons, only about one thousandth.
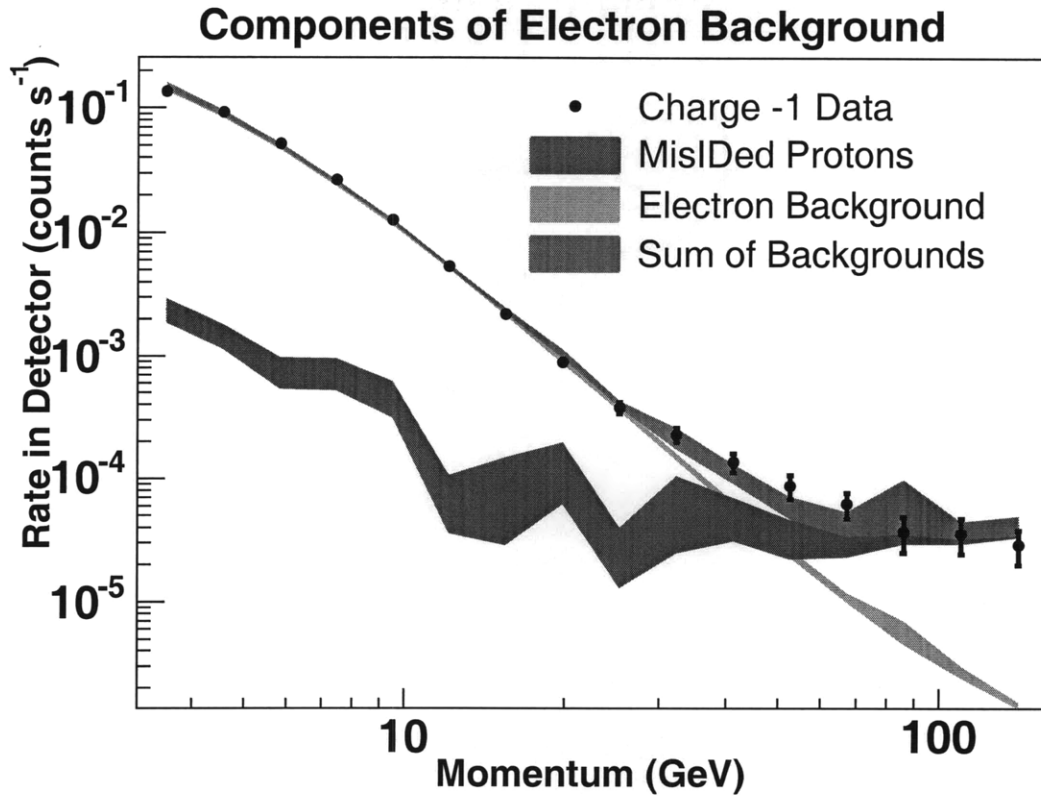
37

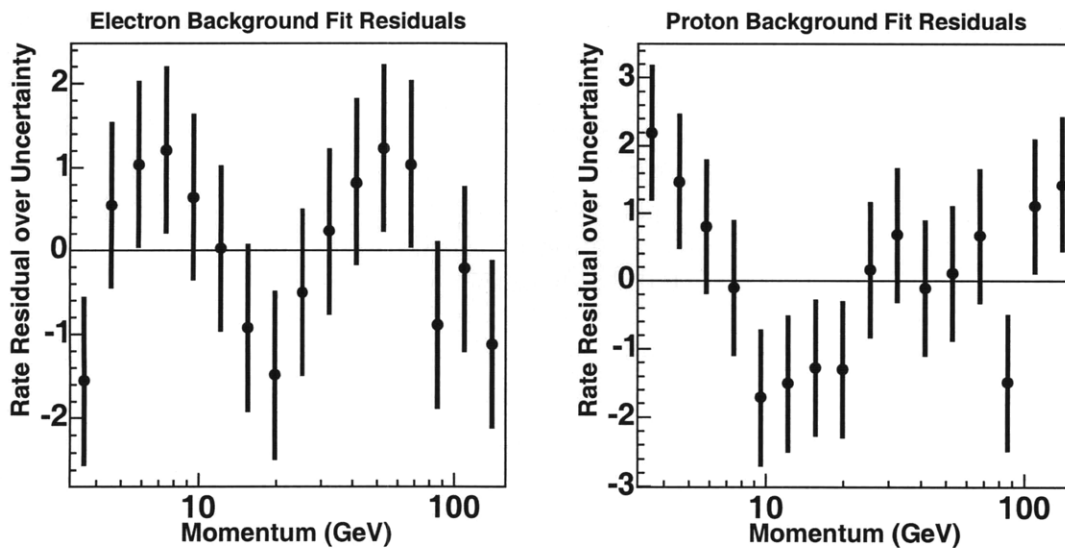Figure 5-4: Electron background fit to AMS01 data [55].

Figure 5-5: Residuals for AMS01 electron (left) and proton (right) background fit.
[55].

5.2   Neutralino Annihilation Electron and Antiproton Signal Production

As mentioned in Chapter 2, the exact process of neutralino annihilation is model dependent. We use the benchmark points in cMSSM framework listed in Chapter 2 for this analysis. The electron or antiproton spectrum at Earth from neutralino annihilation is given by:

$$\frac{d\Phi}{d\Omega dE} = \frac{{\rho_0}^2}{{m_\chi}^2} \sum \sigma_i v B_i \int dr dE' f_i(E') G(E', E, r) \rho^2(r) \tag{5.1}$$

For a particular cMSSM scenario, DarkSUSY [32] is used to calculate the neutralino mass m_χ, their self annihilation branching ratios B_i and the cross section σ_i for each channel. Then Phythia [59] is used to simulate the spectrum of electrons or antiprotons $f_i(E')$ produced in the cascades of particles produced in each annihilation channel. An example of benchmark I is shown in Figure 5-6. An isothermal distribution is assumed for the dark matter distribution $\rho_0 \rho(r)$, where the local density ρ_0 takes the value of 0.3 GeV/cm^3. The Green's function $G(E', E, r)$ describes the evolution of a monoenergetic electron or antiproton signal during the propagation from the place of neutralino annihilation to the Earth, which is simulated by GALPROP. Figure 5-7 shows an example of the Green's function for a 10 GeV monoenergetic electron source with isothermal distribution, integrated over the volume with the scale of electron propagation length: $\int_V dr G(E', E, r) \rho(r)$. Finally, the signal spectrum at the Earth is obtained by convolving the Green's functions with the original electron or antiproton spectrum. Figure 5-8 shows the electron and antiproton spectra from neutralino annihilation for SUSY benchmark I before and after the galactic propagation.
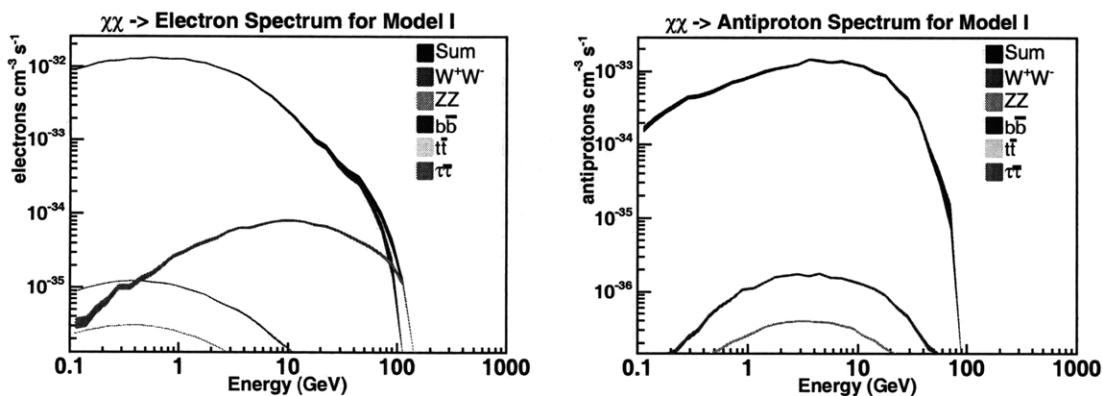

Figure 5-6: Electron (left) and antiproton (right) spectra at the place of neutralino annihilation for benchmark I [55]. The legend gives the final states of neutralino annihilation.
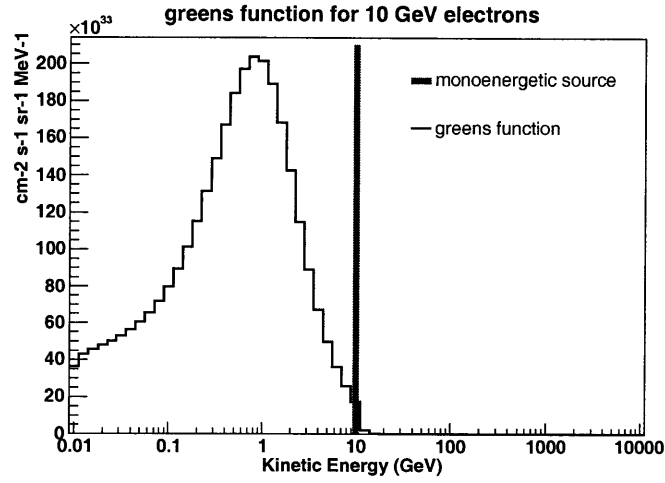
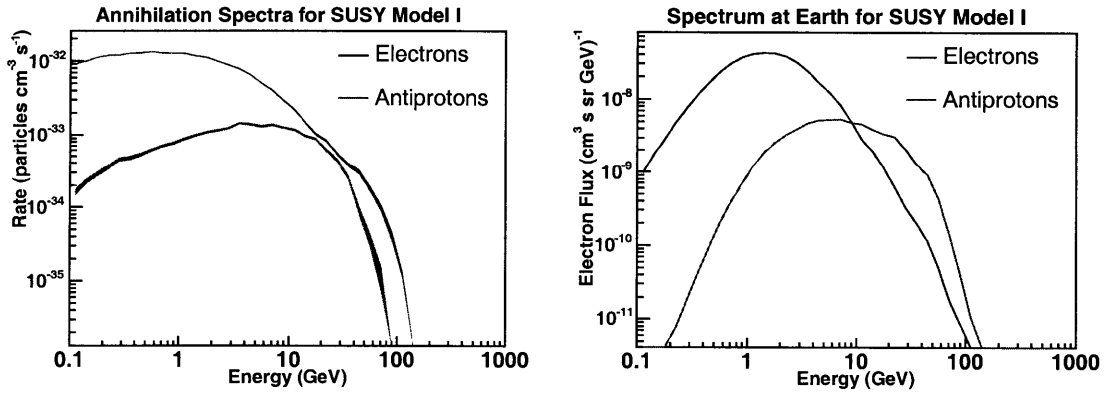Figure 5-7: Green's function for 10 GeV monoenergetic electron source with isothermal distribution.

Figure 5-8: Electron and antiproton spectra from neutralino annihilation at Earth for benchmark I [55].

Chapter 6

The B/C Ratio

This chapter describes the procedure to select boron and carbon events from AMS01 data and to obtain their acceptance by using Monte Carlo. There are 21,674 carbons and 8,582 borons selected out of 100 million raw data. A fit on the B/C momentum spectrum is conducted to constrain the galactic propagation parameters. The diffusion reacceleration model is adopted. The fitting result is given on the propagation parameter space.

6.1   Charge Identification

The identity of boron and carbon is straight forward. They are distinguished from other elements by their charge. Boron has charge equal to 5 and carbon has charge equal to 6. The tracker of AMS01 has very good charge identification ability up to oxygen (Z=8). For lower charged particles (Z=1, 2), both TOF and tracker are used to determine the charge. However, due to the limited dynamic range of the TOF [25], only tracker information is used in the selection of boron and carbon.

6.1.1   Energy Loss Of Heavy Nuclei

Charged particles lose energy when traversing matter primarily by means of inelastic interaction with the electrons of atoms in the matter, which excites or ionizes the atoms. Bethe-Bloch formula is the theoretical description of such energy loss of charged particle in matter per unit length, as given in 6.1. It depends only on two properties of the traversing particles, their charge and velocity. It is proportional to charge square and depends on velocity in a complicated way. Therefore, it provides a very clean way to distinguish charges of different nuclei by comparing their energy loss in each velocity bin.

$$-\frac{dE}{dx} = \frac{4\pi}{m_e c^2} \cdot \frac{nz^2}{\beta^2} \cdot \left(\frac{e^2}{4\pi\epsilon_0}\right)^2 \cdot \left[ln\left(\frac{2m_e c^2 \beta^2}{I \cdot (1-\beta^2)}\right) - \beta^2\right] \qquad (6.1)$$

where $\beta = v/c$, v is velocity of the traversing particle. z is charge of the traversing particle. n is electron density of the target. I is mean excitation potential of the

target.

6.1.2 Cluster Selection

Energy deposition on the trackers is measured by the S and K side independently, so this information is redundant. Because S side has better resolution, only S side is used for the following analysis.

From the quality control in the preselection, each event has hits reconstructed from at least 4 tracker layers. The reconstruction program gives a most possible cluster of energy deposition for the hit on each layer. The energy deposition of an event can be obtained by averaging the clusters on all layers. There are two categories of cuts I apply to make sure the clusters used for this calculation are good.

- Examine the energy distribution within the cluster. Each cluster is composed of at most 5 strips. The strip which has the highest energy deposition should be the point where the particle hits on, and the strips on its both sides should have decreasing readings. If there is more than one hump in the energy distribution among the strips, the cluster has high chance to have been polluted by secondary particles, thus should be marked as bad cluster. If the highest strip is the right-most or left-most one, it would probably underestimate the total energy deposition of the whole cluster. This kind of cluster could be bad, but not necessarily. I do not simply get rid of the clusters of this kind. This concern is taken care of in the cuts of the second category.

- Examine the distribution of the clusters composing a single track to get rid of the outliers. The mean energy deposition is estimated by averaging the clusters excluding the minimum and the maximum one. The std is approximated by taking the square root of the estimated mean. Re-examine all the clusters and keep those within 3σ from the estimated mean. The mean energy deposition is then calculated again by using all the clusters passing the cuts above.

If the incident angle is θ, the actual distance particles traversed would be $dx/\cos\theta$. Therefore the recorded energy deposition needs to be reduced by $\cos\theta$ to obtain the true energy deposition.

$$\frac{dE}{dx}_{true} = \frac{dE}{dx}_{record} \cdot |\cos\theta| \tag{6.2}$$

The energy deposition of all data is plotted in each beta bin, from 0.67 to 1, in steps of 0.01. Several examples are shown in Figure 6-1, Figure 6-2 and Figure 6-3 for data, boron Monte Carlo and carbon Monte Carlo, respectively.

6.2 Event Selection

6.2.1 Charge Selection

Energy deposition plots in each velocity bin for data and Monte Carlo (MC) are generated in the same way. A discrepancy between data and MC in the cluster
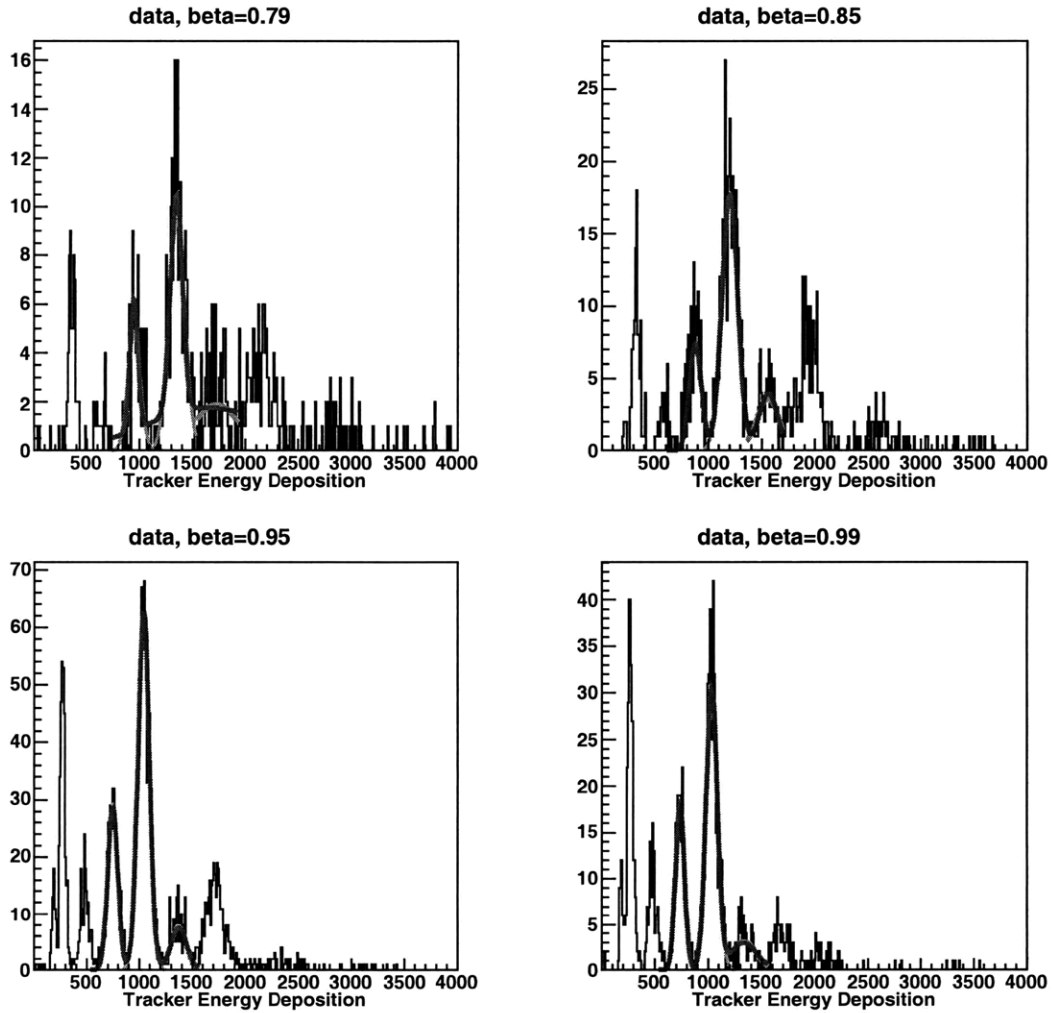
Figure 6-1: Energy deposition on trackers for data in several beta bins. The colored lines are Gaussian fits.
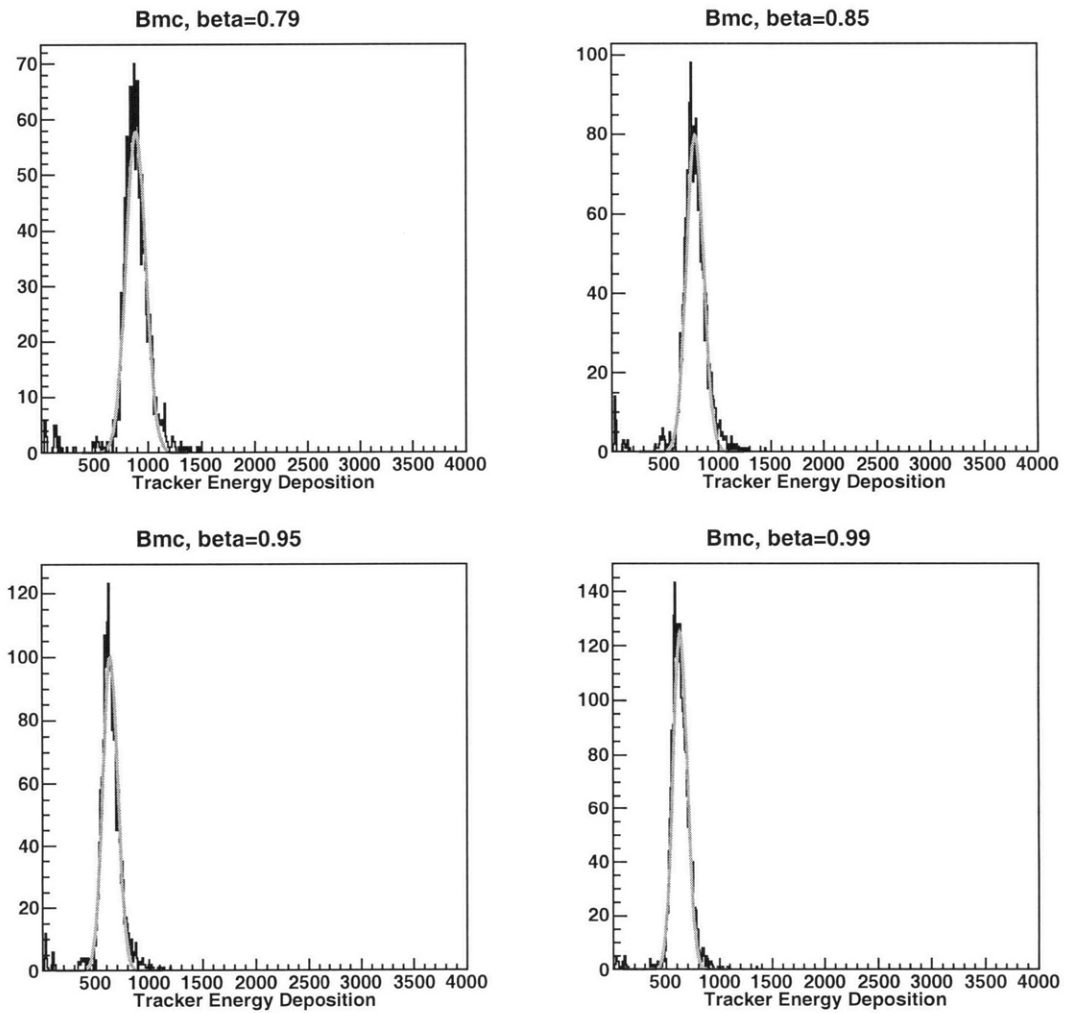
Figure 6-2: Energy deposition on trackers for boron Monte Carlo in several beta bins. The colored lines are Gaussian fits.
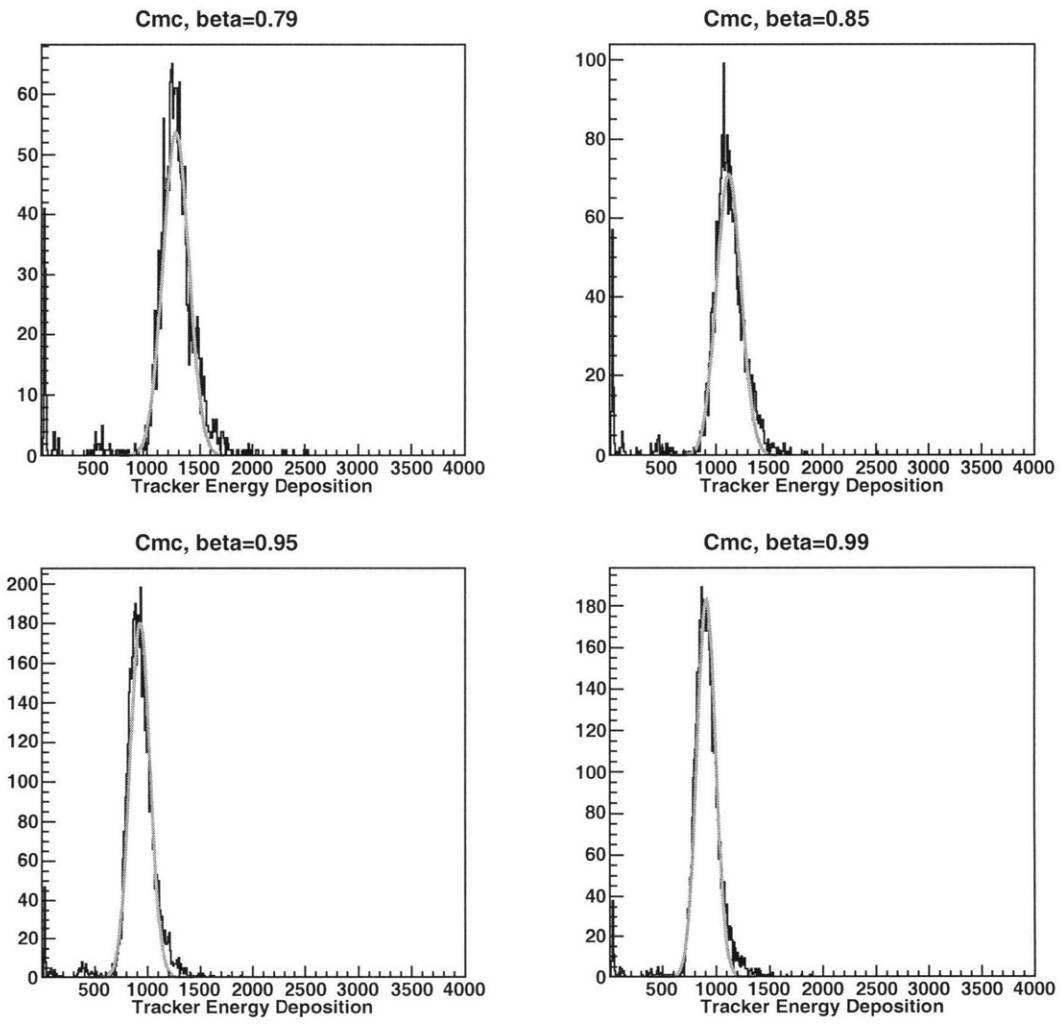
Figure 6-3: Energy deposition on trackers for carbon Monte Carlo for several beta bins. The colored lines are Gaussian fits.
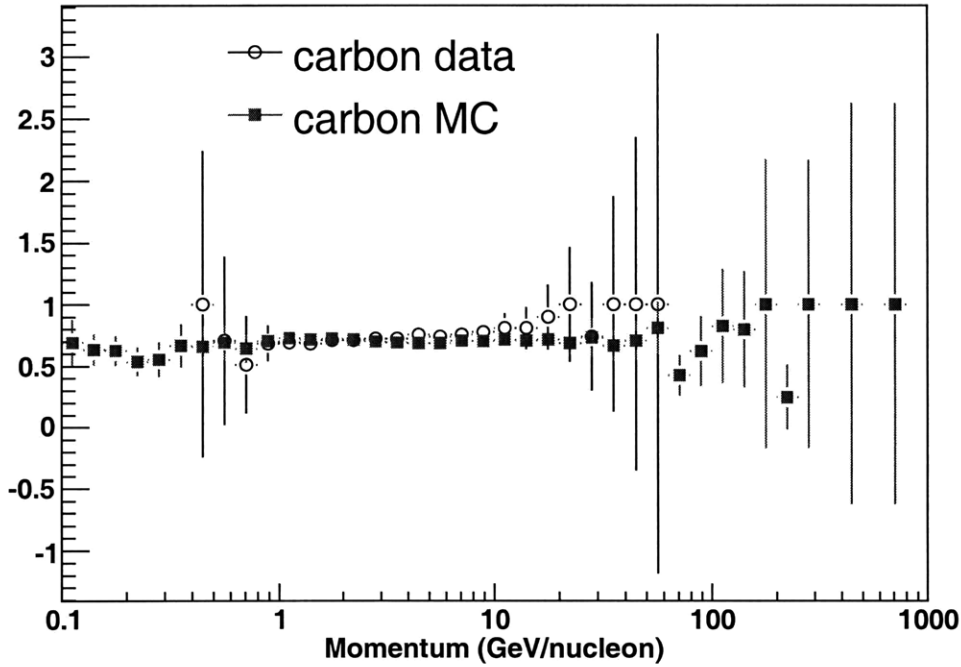
Figure 6-4: Comparison of two ratios: circle: the ratio of 1σ data to 2σ data; square: ratio of 1σ MC to 2σ MC.

position and width makes it difficult to determine comparable selection criteria for data and MC. Fortunately, clusters of each element for data and MC have similar shapes and can be fitted fairly well by a Gaussian. Therefore, my procedure to select boron and carbon is the following: Fit the data energy deposition histogram with three Gaussians in a rough region for boron, carbon and nitrogen. For each element, select events with energy deposition within 2 standard deviations from the mean. Fitting results for several velocity bins are shown in Figure 6-1, 6-2 and 6-3. It can be seen that each element separates from each other reasonably well and no significant contaminations from the neighbor elements are seen. The same Gaussian fit is applied to boron and carbon MC and the same selection criteria are employed.

Without beam tests to do better fine-tuning of the MC, this "k-sigma" method is a reasonable way to do the selection with the information handy. A test is done to verify the feasibility of this method. Data and MC are selected within 1σ and 2σ respectively. Taking carbon as an example, the two data spectra are called 1σ data and 2σ data, and the two acceptance matrices are called 1σ acceptance and 2σ acceptance. I then pick a carbon spectrum generated by GALPROP from an arbitrary model and convolve it with 1σ and 2σ acceptance respectively. This produces two carbon spectra on the detector, which characterize the difference in MC due to 1 or 2σ selection criteria. These two spectra were denoted as 1σ MC and 2σ MC. If the "k-sigma" selection criterion is ideally comparable for data and Monte Carlo, the ratio of 1σ data to 2σ data and the ratio of 1σ MC to 2σ MC should be exactly the

46

same. They are plotted in Figure 6-4. They are consistent with each other within the errors.

There are 25,079 events past 2σ selection identified as carbons, and 9,847 events identified as borons. Their acceptances obtained by similar selection on MC are shown in Figure 6-7.

6.2.2 Cosmic Origin Selection

The final step of selection is to differentiate borons and carbons of cosmic origin from those trapped by the Earth magnetic field or produced in the atmosphere (the latter two categories are known as atmospheric secondary particles). A set of programs [3] is adopted to trace charged particles in the geomagnetic field. Tracing backwards a certain amount of time (~ 20 seconds), if particles come from sufficiently far away from the Earth ($\geq 10R_\oplus$), they are identified as of cosmic origin. The advantage of using this technique than simply cutting all events with energy below the geomagnetic cutoff is that more events we can possibly keep for analysis. There are approximately twice as many events survived by using this method. However, the drawback is that it is difficult to calculate the exposure time in this case, because there is some probability that charged particles with energy below the geomagnetic cutoff bouncing off by the magnetic field, which we do not have much handle on. Fortunately, the quantity we are interested in is the ratio of borons to carbons, not their absolute spectra. The exposure time is only a function of rigidity which can be canceled out by taking the ratio of the two elements. Therefore, we use this tracing technique for selection to get more statistics.

There are 21,674 carbons and 8,582 borons identified as of cosmic origin (Figure 6-5). There are 3,405 carbons and 1,265 borons identified as atmospheric secondaries (Figure 6-6).

6.3 Fitting

GALPROP [62] predicts the B/C spectrum given the propagation model and the injection spectra. As discussed before, the diffusive reacceleration model is employed. B/C has little dependence on the injection spectra. Figure 6-8 shows the comparison of the effect of varying injection spectra and propagation parameters on B/C. Therefore, in the B/C fit, the injection index is fixed as the default value 2.36 suggested by Strong and Moskalenko. Only the propagation parameters, which are diffusion coefficient D_{xx} and Alfven velocity v_A, are allowed to vary. The fitting method is described in Appendix B. Boron and carbon spectra generated by GALPROP, modulated by solar modulation, and convolved with their acceptance matrices respectively, are fit to our B/C data. The best fit yields $D_{xx} \approx 4.8$, and $v_A \approx 30$, with $\chi^2/N = 1.3(N = 18)$ (Figure 6-9).

Figure 6-10 shows the χ^2 of the fit on the propagation parameter space. D_{xx} and v_A have a strong correlation. The reason is that the poor energy resolution washes out the difference between the features of peak position and overall height, which are

Cosmic Borons

Cosmic Carbons

Figure 6-5: AMS01 cosmic boron (panel (a)) and carbon (panel (b) counts as a function of momentum on the detector, before accounting for the acceptance.

Atmospheric Secondary Borons

a)

counts

10^2

10

1

Momentum (GeV/c) per nucleon

0.1 1 10 100 1000

Atmospheric Secondary Carbons

b)

counts

10^3

10^2

10

1

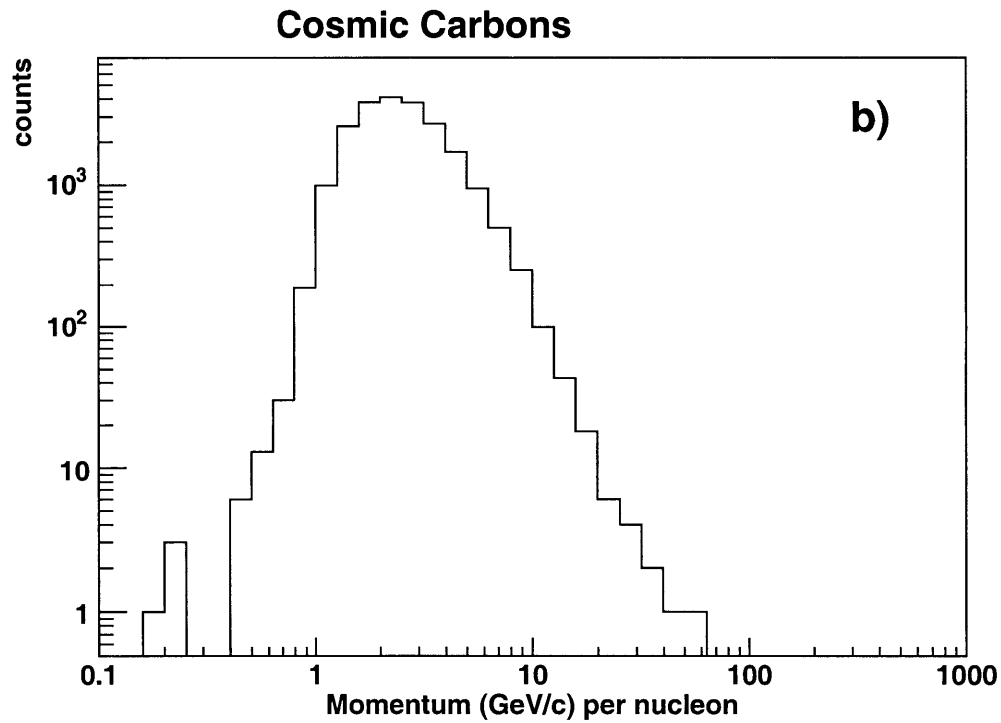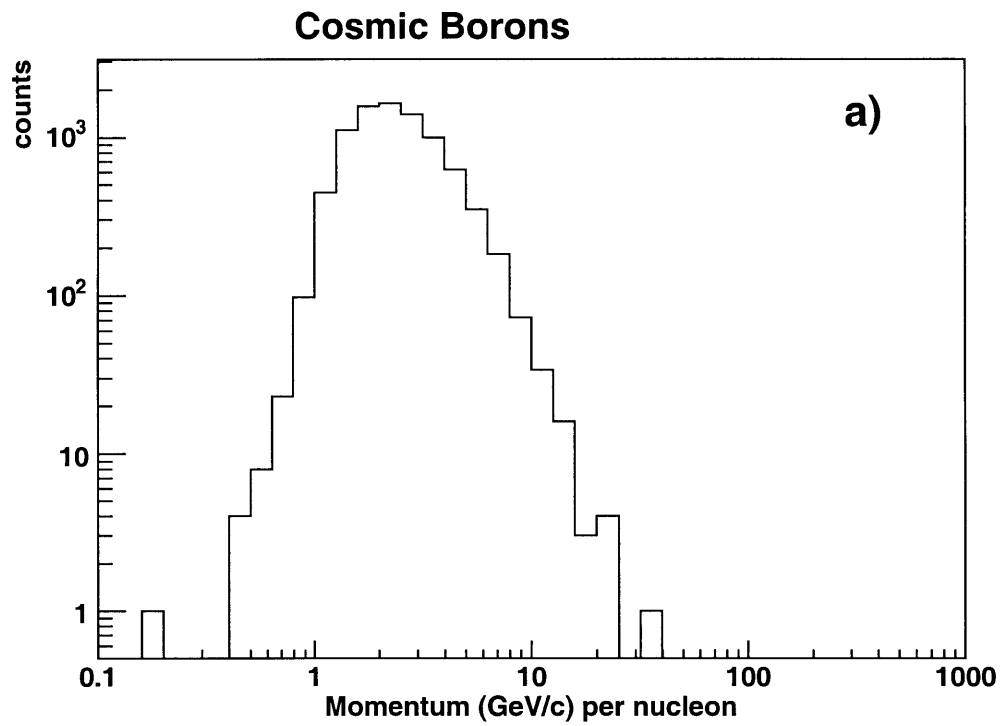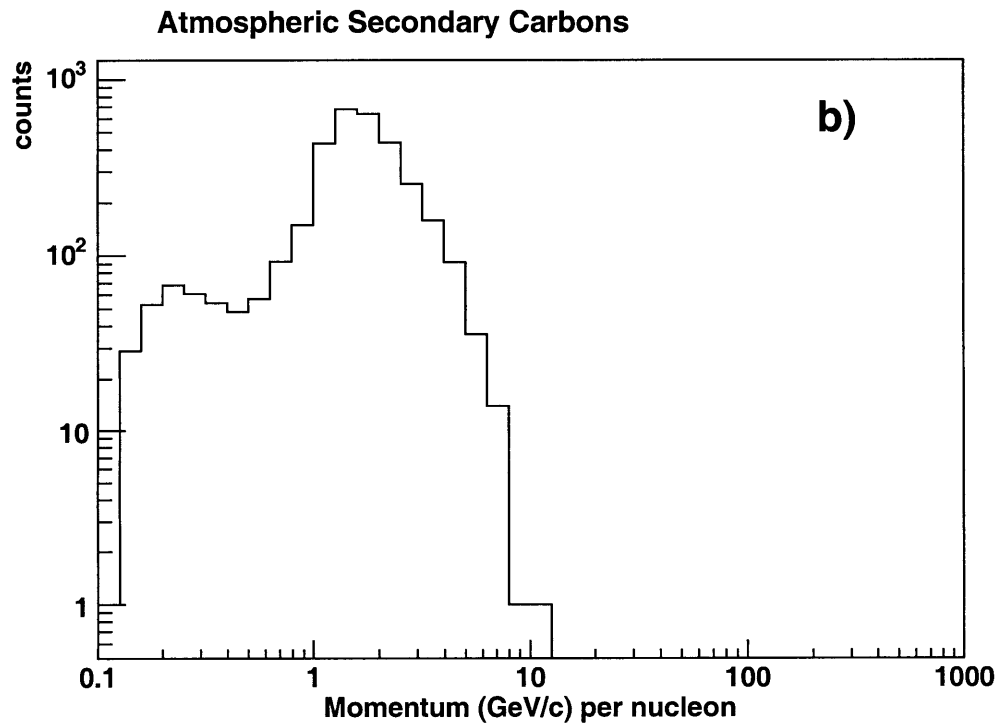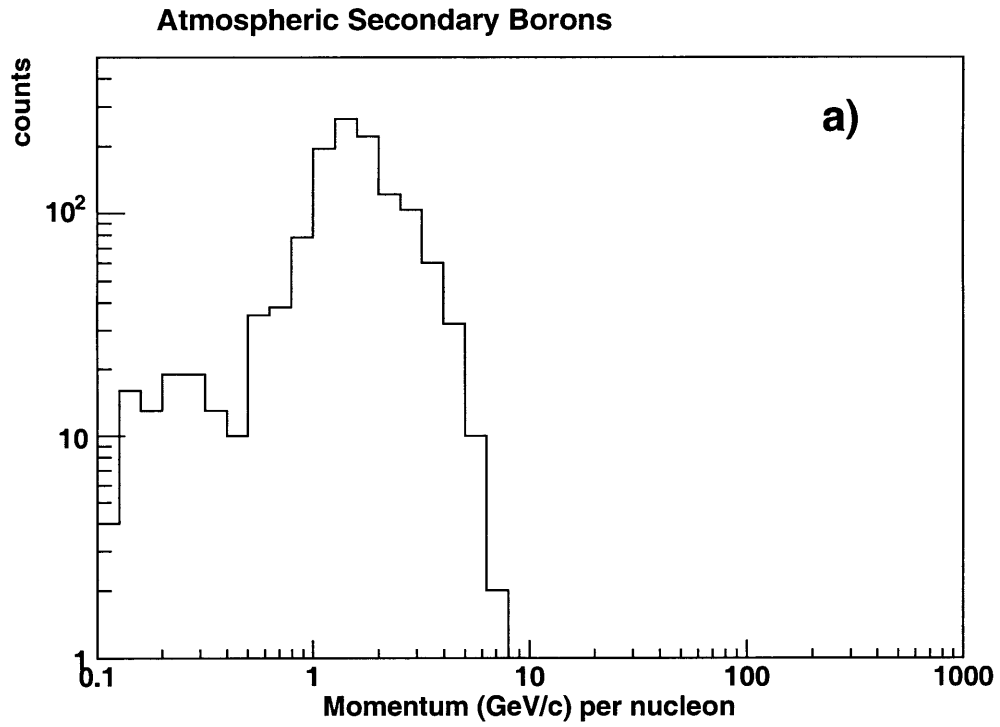Momentum (GeV/c) per nucleon

0.1 1 10 100 1000

Figure 6-6: AMS01 atmospheric secondary boron (panel (a)) and carbon (panel (b)) counts as a function of momentum on the detector, before accounting for the acceptance.
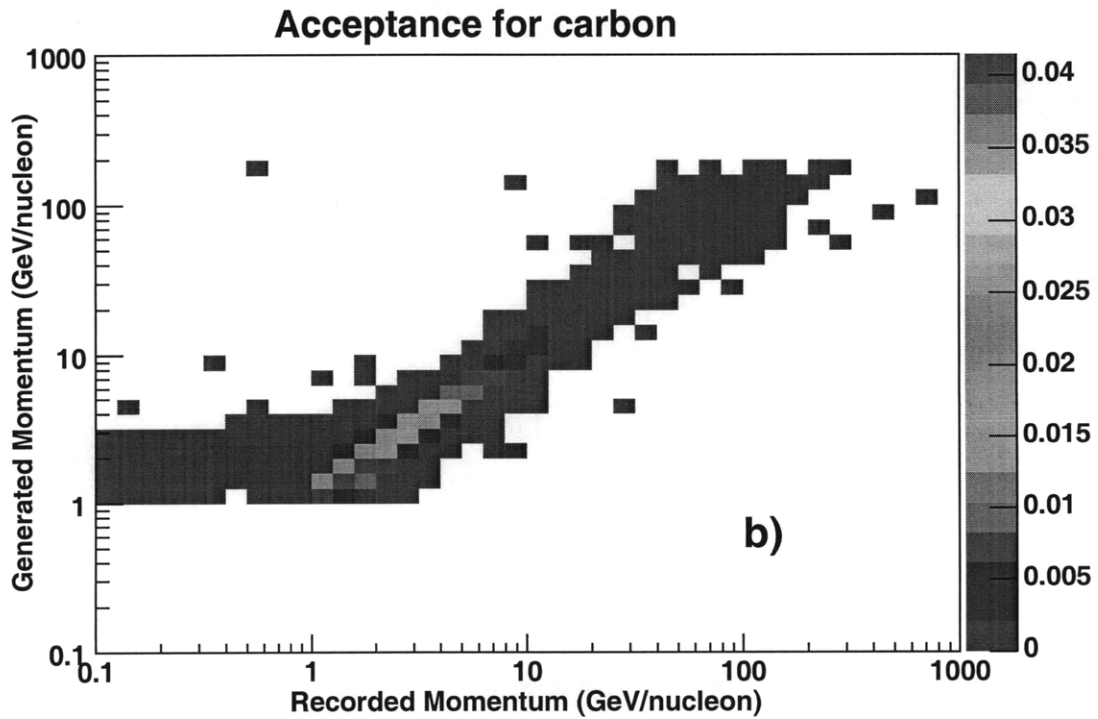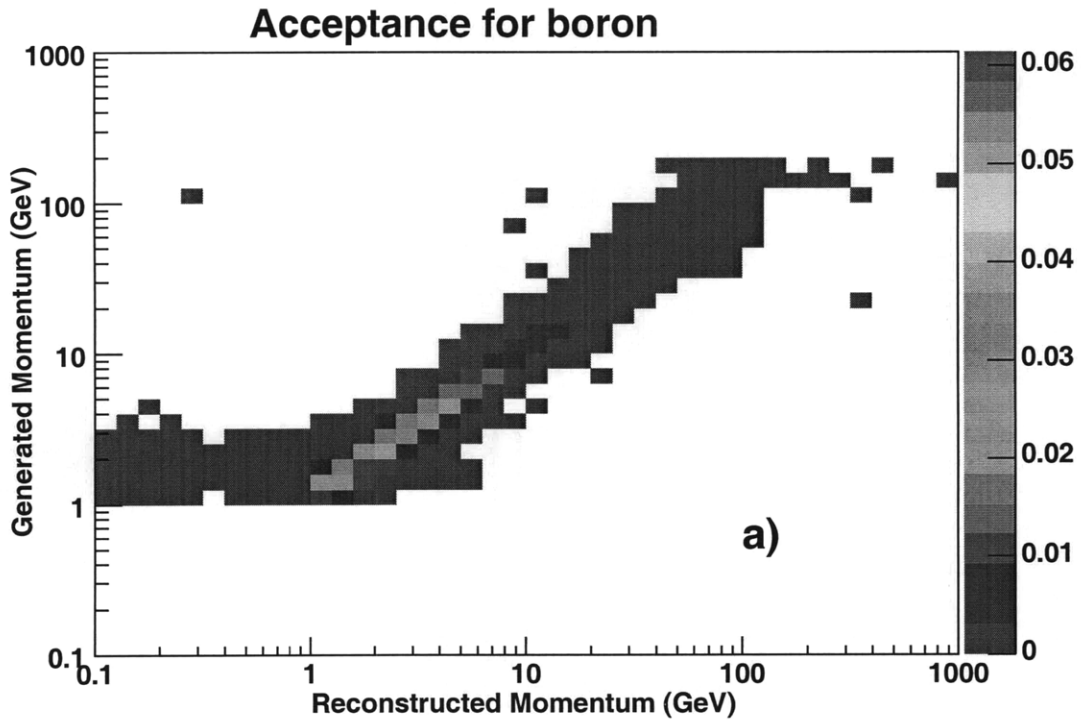
Figure 6-7: Acceptance of boron (panel (a)) and carbon (panel (b)) generated by Monte Carlo.
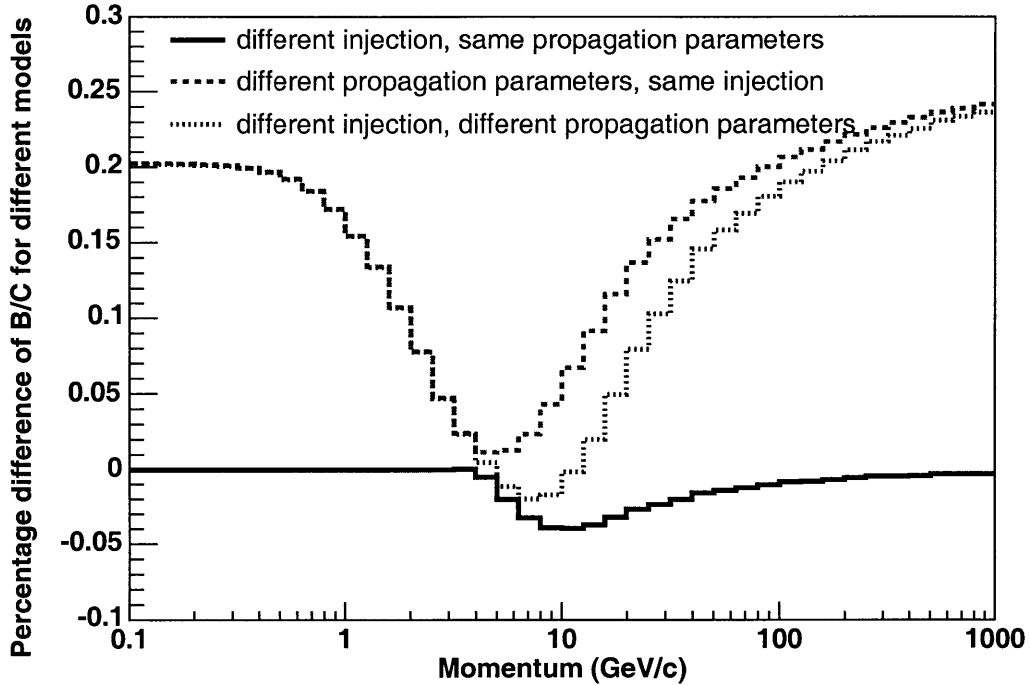
Figure 6-8: Difference of B/C for different models, simulated by GALPROP. Solid line: with only the injection changed, the difference in B/C is small; dashed line: with only the propagation parameters changed, the difference is sizable; dotted line: with both changed, the difference is dominant by the effect from propagation.

the typical information carried by v_A and D_{xx} respectively. A confidence region is found for D_{xx} and v_A, as described in Appendix B (Figure 6-11).

Alternatively, we plot the χ^2 of the fit on D_{xx} vs v_A/D_{xx} space, shown as Figure 6-12, which is attempted to decorrelate the propagation parameters. The effect of decorrelation by doing this is not significant since the trend line does not go through the origin.

6.4 Combining With Proton Fit

The galactic propagation model we are seeking is a model which can explain all the observations self-consistently. Protons are the majority constituent of cosmic rays, so their measurement is most reliable. The proton spectrum is thus used to investigate self-consistency of the propagation model. In the proton fit, propagation parameters, v_A and D_{xx}, are fixed, and only the injection index and normalization are allowed to vary. In Figure 6-13, I survey the proton fit on the propagation parameter space. A poor proton fit means that no matter how one adjusts the injection, a good fit can not be found with these propagation parameters. For example, our proton data disfavor the combinations of low D_{xx} and low v_A while the B/C loses the resolving
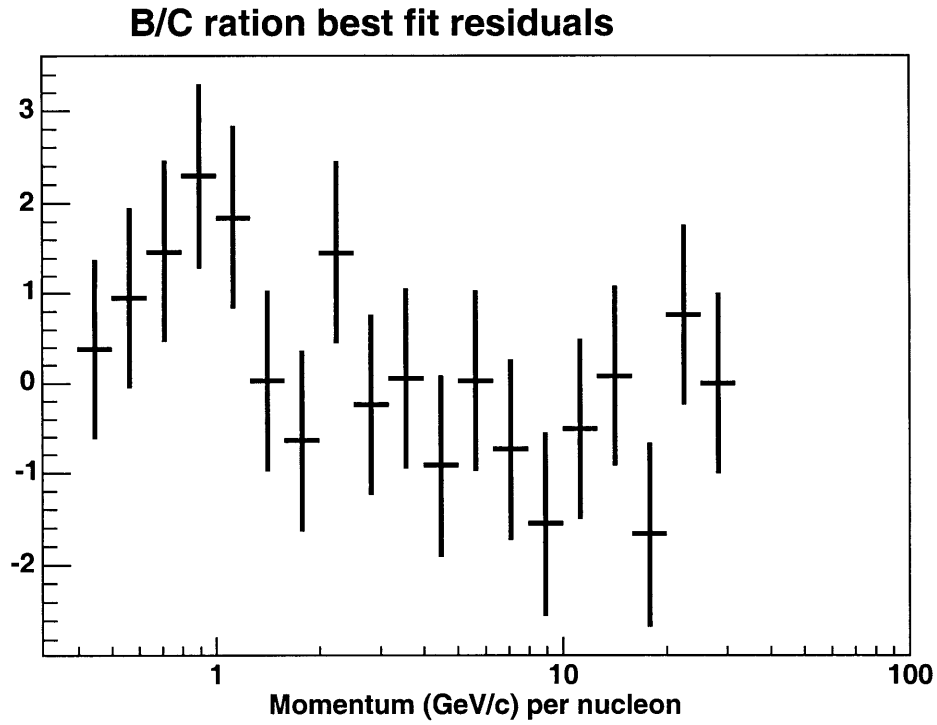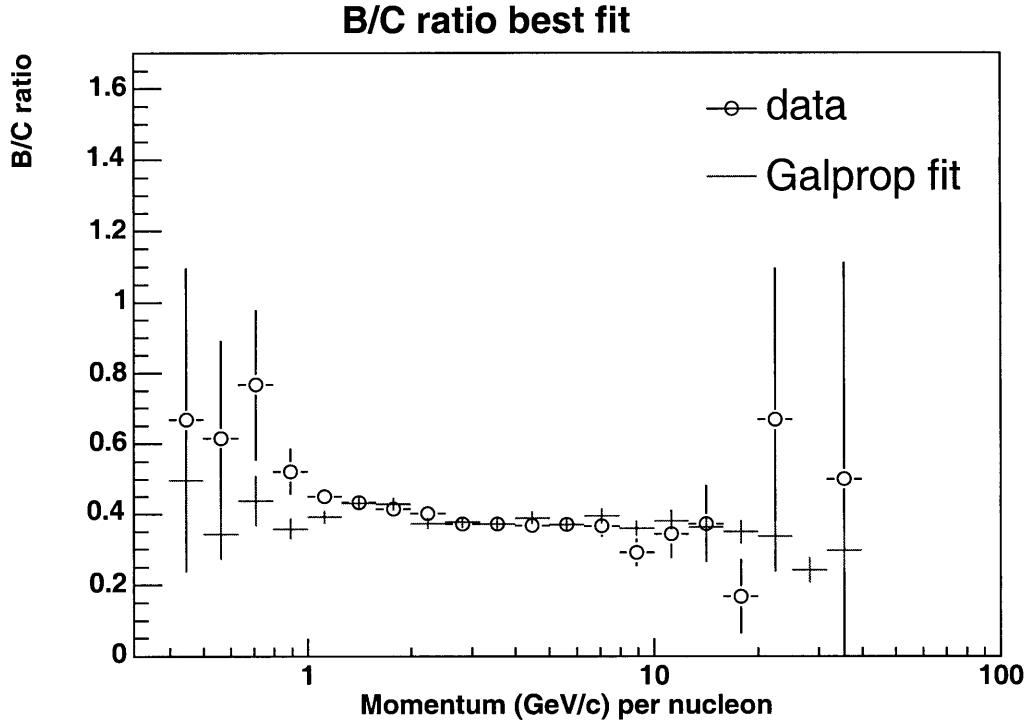
Figure 6-9: Upper panel: Best fit of B/C ratio on the detector; lower panel: residuals of the fit.
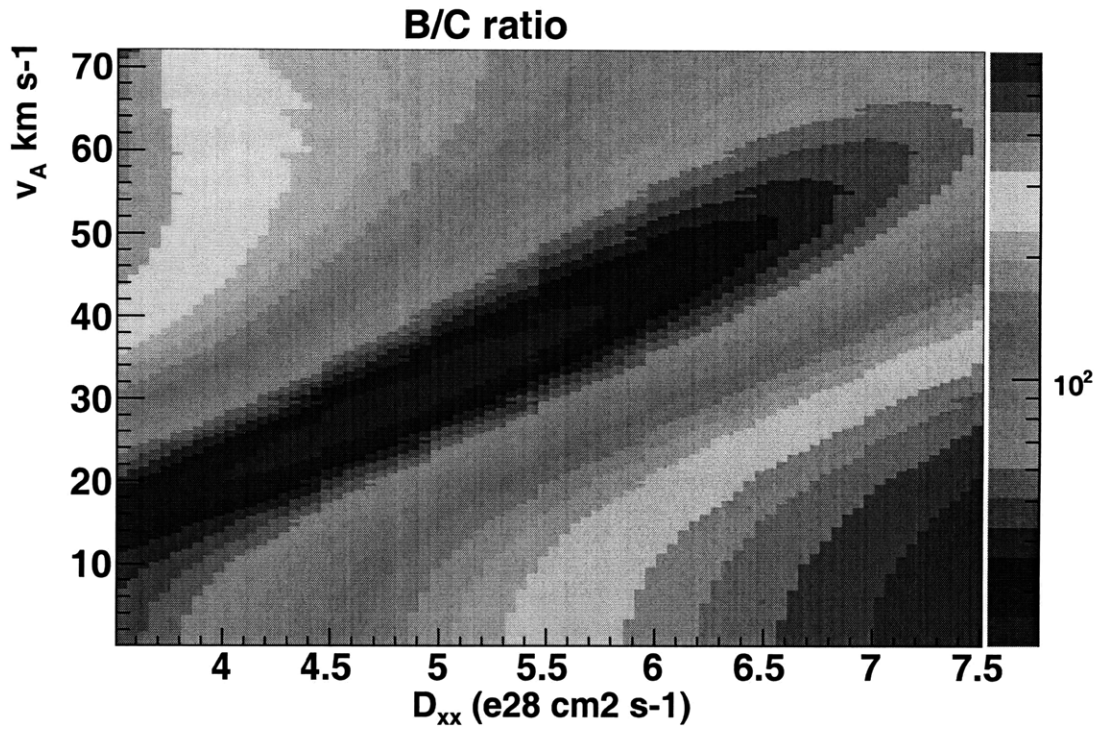
Figure 6-10: B/C fit on the propagation parameter space: D_{xx} vs v_A.
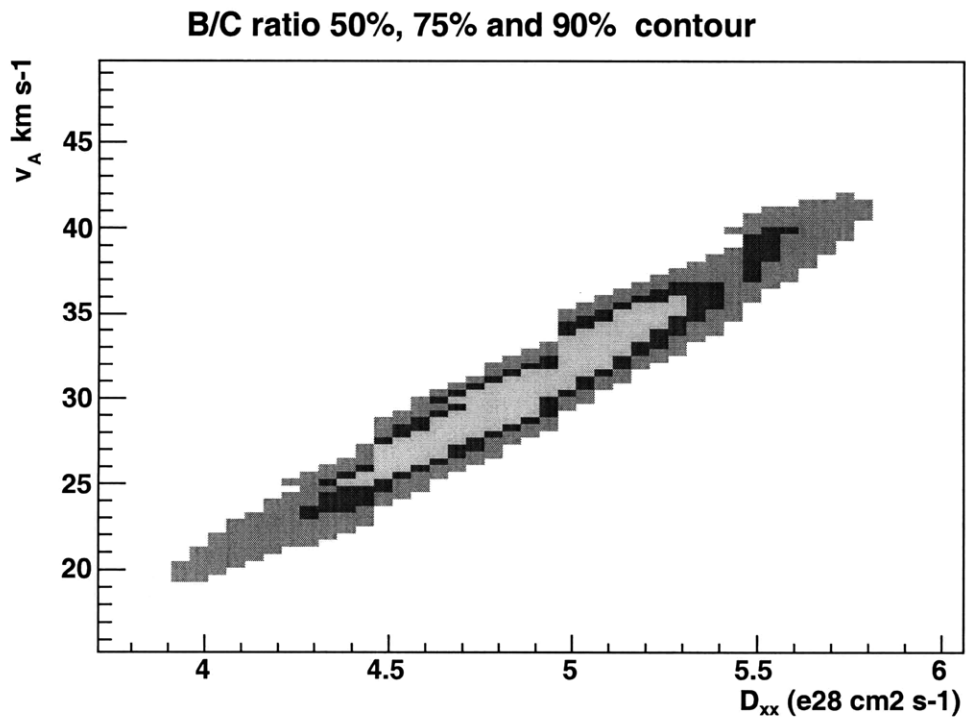
Figure 6-11: Confidence regions of B/C fit for D_{xx} and v_A.
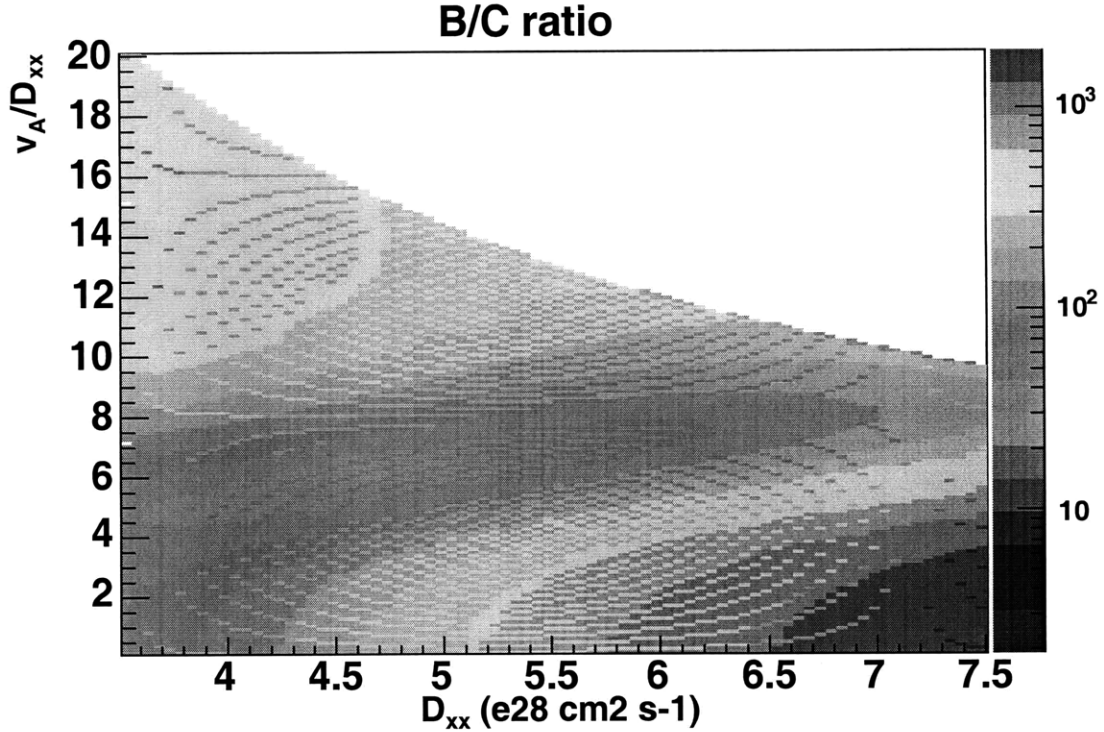
Figure 6-12: B/C fit on the propagation parameter space: D_{xx} vs v_A/D_{xx}.

power along that band. In conclusion, by adding the information from proton fit, our data favor the right side of the confidence region of D_{xx} and v_A.

6.5 Comparison with Other Measurements

In order to make a comparison of our data with other measurements, we need to obtain the B/C above the detector. This unfolding is not a trivial problem, since the acceptance matrix is singular. If we use Singular Value Decomposition class to invert the matrix directly, a lot of negative numbers are generated in the inverted matrix which have no physical meaning. Instead, the method of convergent weights [35] [43], an iterative procedure, is used to solve this problem (see Appendix D).

The unfolded B/C spectrum is shown in Figure 6-14. HEAO3 [29] and Voyager2 [64] data are also plotted in the same figure. Our result is consistent with these measurements, although ours have larger error bars. Limited statistics above and below a few GeV are limited by statistical error. Around several GeV, MC systematics dominate.(see Chpater 9).

6.6 Global Constraints on Propagation Models

Better constraints on propagation models can be obtained by including HEAO3[29] and Voyager2 [64] data in our fit. Following exactly the same method as fitting

B/C ratio 50%, 75% and 90% contour
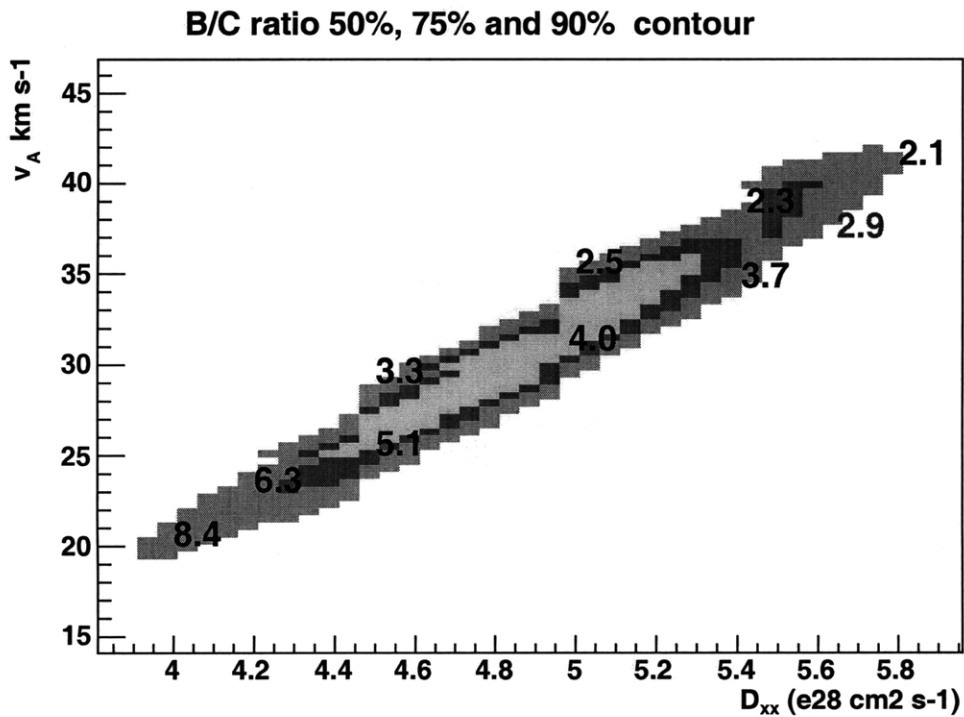
Figure 6-13: Self-consistency check by proton fit. The number is the chi square of the best proton fit for that particular combination of propagation parameters. The red number indicates the default set of propagation parameters in GALPROP. The color code underneath is the 50%, 70% and 90% contour from B/C fit (copied of Figure 6-10).
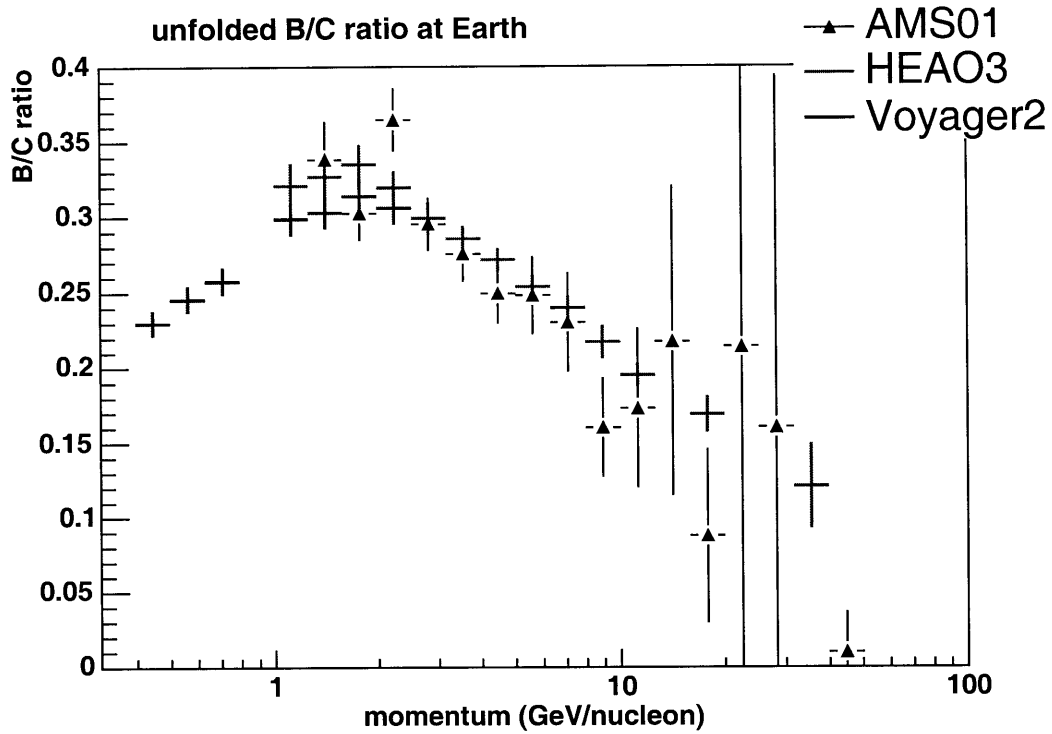
Figure 6-14: Boron to carbon ratio at Earth

AMS01 data only, the best fit yields $D_{xx} \approx 5.7$, and $v_A \approx 35.6$, with $\chi^2 \approx 2.2$ ($N = 36$). Figure 6-15 is a scan of the fit over the propagation parameter space. A strong correlation is still present between D_{xx} and v_A. Figure 6-16 indicates the confidence regions for these two parameters.
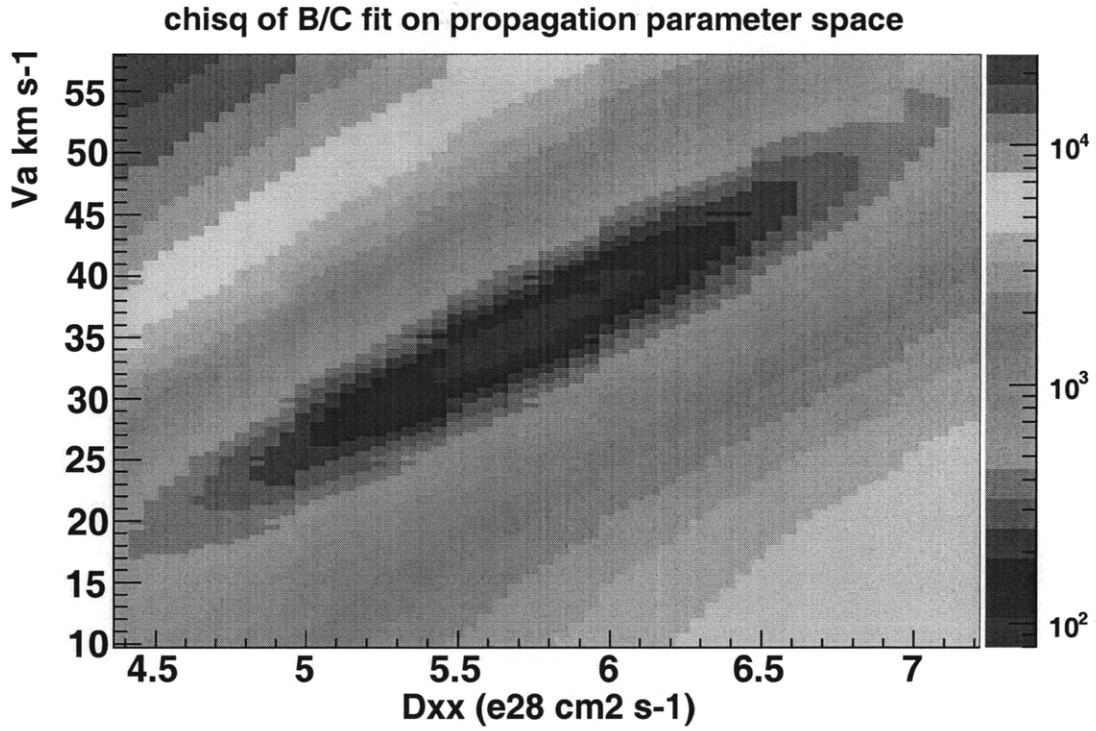
Figure 6-15: B/C fit combining AMS01, HEAO3 and Voyager2 data.
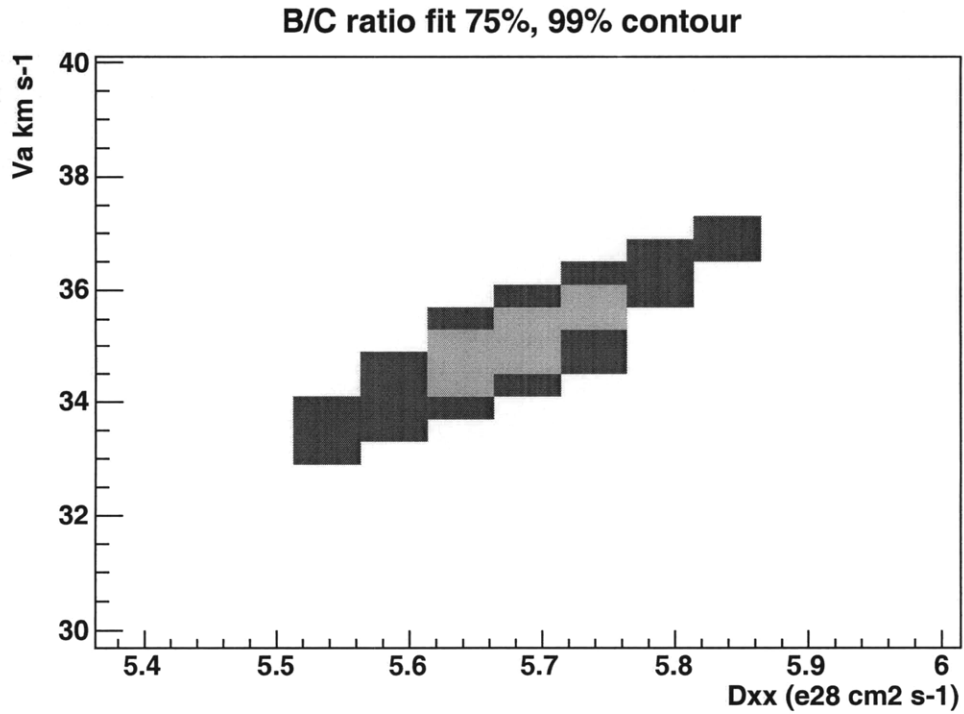
Figure 6-16: Confidence regions of the B/C fit combing AMS01, HEAO3 and Voyager2 data.

Chapter 7

Results

7.1 Constraining the Boost Factor

We fit a model of e^- backgrounds and χ annihilation to e^- and $\bar{p}$ momentum spectra in order to determine the maximum allowable boost factor consistent with AMS01 Z=-1 data. In the fit, the background normalization, injection index and boost factor are free parameters. The boost factor is constrained to be non-negative in the fit. The fit actually relies on the spectral shape — DM annihilation produces spectral feature on top of an otherwise smooth power-law like spectrum. The best fit of the boost factors for all SUSY benchmarks [55] are not statistically significantly different from zero, which means our fitting results are consistent with no dark matter for all SUSY scenarios with boost factor of unity. However, an upper limit of the boost factor with certain confidence allowed by our data can be determined. Tables 7.1 and 7.2 show the best fits and the 90% upper bounds of the boost factor, obtained with a particular set of propagation parameters in diffusive reacceleration (DR) model (the default values in GALRPOP: $D_{xx} = 5.75 \times 10^{28}$ cm^2 s^{-1}, $v_A = 36$ km s^{-1}).

A best fit boost factor equal to zero means that no improvement is made by including the neutralino annihilation products (electrons and antiprotons) for that particular SUSY scenario. For the benchmark M, the best fit of the boost factor is a value which could be realized in our Galaxy, while the χ^2 has a sizable change compared with that of the background-only case. Therefore, we would most possibly obtain a useful upper bound for this scenario. However, for the benchmark H, the best fit boost factor is too large to be realistic, and the χ^2 improves even less than 0.5% over the background only case. This analysis is thus insensitive to this particular scenario. For the benchmark J, even though the best fit boost factor might still be possible given a very clumpy dark halo, the χ^2 changes by less than the convergence criteria of the fitting algorithm. We therefore expect to obtain a very loose upper bound. in Table 7.2, we see this is the case.

SUSY Benchmark	Boost Factor	$1\sigma\pm$	Background Normalization	Background Index	χ^2/dof (dof=13)
A	0	17874	0.729	2.695	0.95
B	0	412	0.719	2.695	0.95
C	0	6863	0.729	2.695	0.95
D	0	56261	0.729	2.695	0.95
E	0	93	0.729	2.695	0.95
F	0	3603	0.729	2.695	0.95
G	0	900	0.729	2.695	0.95
H	26349	86639	0.690	2.720	0.93
I	0	130	0.729	2.695	0.95
J	866	11436	0.710	2.707	0.95
K	184.2	349	0.664	2.739	0.91
L	0	142	0.729	2.695	0.95
M	26	44	0.658	2.744	0.91

Table 7.1: Best fits for all benchmark points.

SUSY Benchmark	90% Upper Bound of the Boost Factor
A	52001
B	1871
C	16935
D	77566
E	364
F	3731
G	2811
H	206454
I	435
J	13626
K	902
L	262
M	116

Table 7.2: 90% upper bounds of the boost factor.

7.2 Propagation Model Uncertainties

An optimal region of propagation parameters for the diffusive reacceleration (DR) model can be deduced by the B/C ratio, which is done in the previous chapter. AMS01 data alone produce weak constraint. Combined with the constraints from proton flux, I define benchmarks on the DR propagation model parameter space, as shown in Figure 7-1. The default settings of GALPROP is denoted as "S&M", where $D_{xx} = 5.75 \times 10^{28}$ cm^2 s^{-1}, $v_A = 36$ km s^{-1}. I then perform the same fitting as described in Section 7.1, scanning the propagation parameter space following these benchmark points. The extracted upper bounds of the boost factor are given in Table 7.3. For the simplicity for comparison, they are given in terms of the percentage difference compared to that of the S&M benchmark point. For example, for SUSY model A, the boost factor 90% upper bound is decreased by 8% using DR model at benchmark I than that of DR model at benchmark S&M. Under this loose constraint, the upper bounds of the boost factor change less than 30% resulting from the uncertainty of modeling the galactic propagation.

The blue line is a linear fit through the reference point S&M and the two points where the changes in boost factors are smallest, II and VII. We see that above the line, the changes in the boost factor are negative, while below the line, the changes are positive. The further away from the line, the bigger the change is. The reason is that reacceleration produces bumps, so relatively larger Alfven velocity (reacceleration) leaves smaller room for adding in DM signal, and thus decreases the upper limit of the boost factor. Therefore, it is actually the spread in the Alfven velocity that determines the induced uncertainty of the boost factor upper bound. With AMS01 data alone, the spread is ~ 5 km/sec.

Much tighter constraints on the propagation parameters can be obtained by adding HEAO3 and Voyager2 data in the fit. Benchmark points I and II defined in Figure 7-1 are at the lower and upper edge of the 99% confidence contour(Figure 6-11). In this case, the spread in v_A shrinks to ~ 2 km/sec, thus the resultant uncertainty in the upper bound of the boost factor is down to $\sim 10\%$.

B/C ratio 50%, 75% and 90% contour
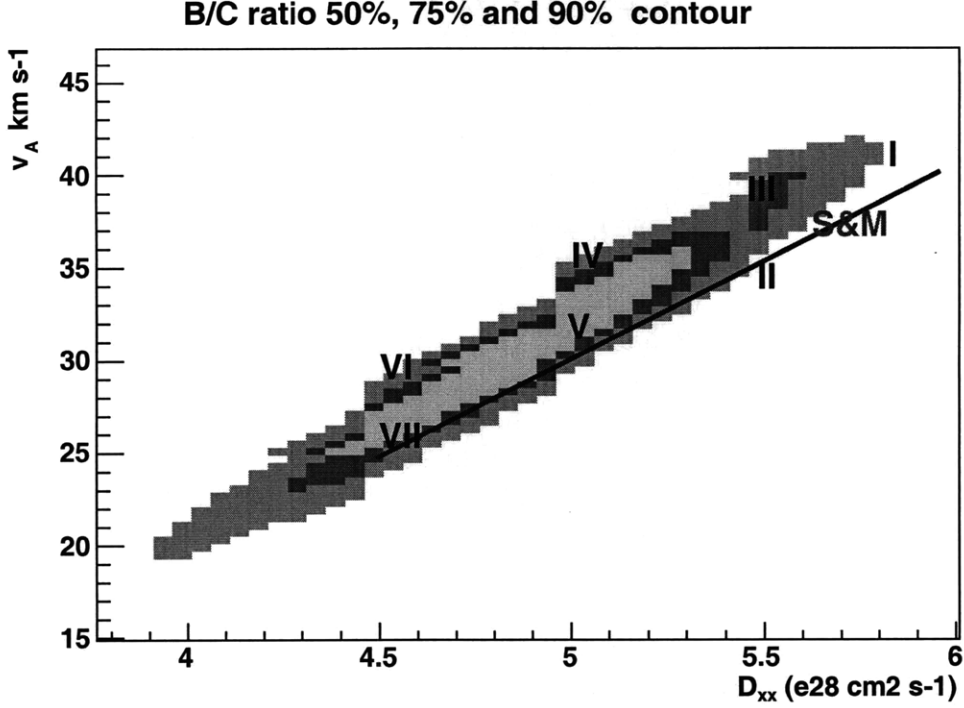
Figure 7-1: Benchmark points on the DR propagation model parameter space, suggested by AMS01 B/C ratio and proton flux.

90% Upper Bounds of the Boost Factor								
SUSY	Galactic Propagation Benchmark							
Benchmark	S&M	I	II	III	IV	V	VI	VII
A	52001	-8%	4%	-21%	-30%	-11%	-23%	-1%
B	1871	-4%	0%	-14%	-24%	-15%	-23%	-10%
C	16935	-8%	4%	-20%	-30%	-11%	-22%	-2%
D	77566	-8%	5%	-19%	-26%	-51%	-17%	6%
E	364	-7%	3%	-23%	-28%	-11%	-23%	-2%
F	3731	-9%	5%	-20%	-31%	-10%	-22%	-1%
G	2811	-8%	3%	-21%	-29%	-12%	-22%	-3%
H	206454	-43%	3%	-21%	-29%	-13%	-21%	-5%
I	435	-8%	3%	-21%	-29%	-13%	-22%	-4%
J	13626	-8%	3%	-19%	-27%	-13%	-22%	-4%
K	902	-7%	3%	-23%	-30%	-11%	-19%	-4%
L	262	-6%	3%	-19%	-26%	-13%	-22%	-3%
M	116	-7%	3%	-18%	-26%	-10%	-18%	-3%

Table 7.3: 90% upper bounds of the boost factor, scanning on the optimal propagation parameter region constrained by AMS01 data only. The percentages shown in the table are the change of the 90% upper bound of the boost factor of that particular galactic propagation benchmark compared with that of the S&M benchmark.

Chapter 8

PAMELA Results

PAMELA recently released their first results of antiproton and positron [4] [?]. In this chapter, I investigate the implications of these results on Boost Factor (BF) constraints.

8.1   The $\bar{p}/p$ Ratio

8.1.1   Background Only

Figure 8-1 shows the PAMELA $\bar{p}/p$ data and the GALPROP predictions of our favored propagation parameters assuming no dark matter. The antiproton data can be explained by the predictions of secondary antiprotons, and are consistent with no dark matter.

8.1.2   Background + DM Signal

We can add antiprotons from neutralino annihilations for different SUSY benchmarks. Maximum boost factors can be derived by requiring that the resulting antiproton flux does not exceed 2σ error bars of the PAMELA data in each kinetic energy bin above 10 GeV. Smaller energy bins are not considered because of two reasons: (1) they are not the sensitive energy region for the DM signal; (2) they suffer from solar modulations. The results are shown in Figure 8-2. For example, the boost factors can not exceed 120, 21, 43, and 5, for SUSY benchmarks B, E, K and M, respectively. The effect of propagation model parameters on the BF upper limits is less than an order of magnitudes in all cases. (see Figure 8-3).

8.2   The $e^+/(e^+ + e^-)$ ratio

8.2.1   Background Only

Figure 8-4 shows the PAMELA $e^+/(e^+ + e^-)$ data and GALPROP predictions of our favored propagation models assuming no dark matter. The agreements are poor. The
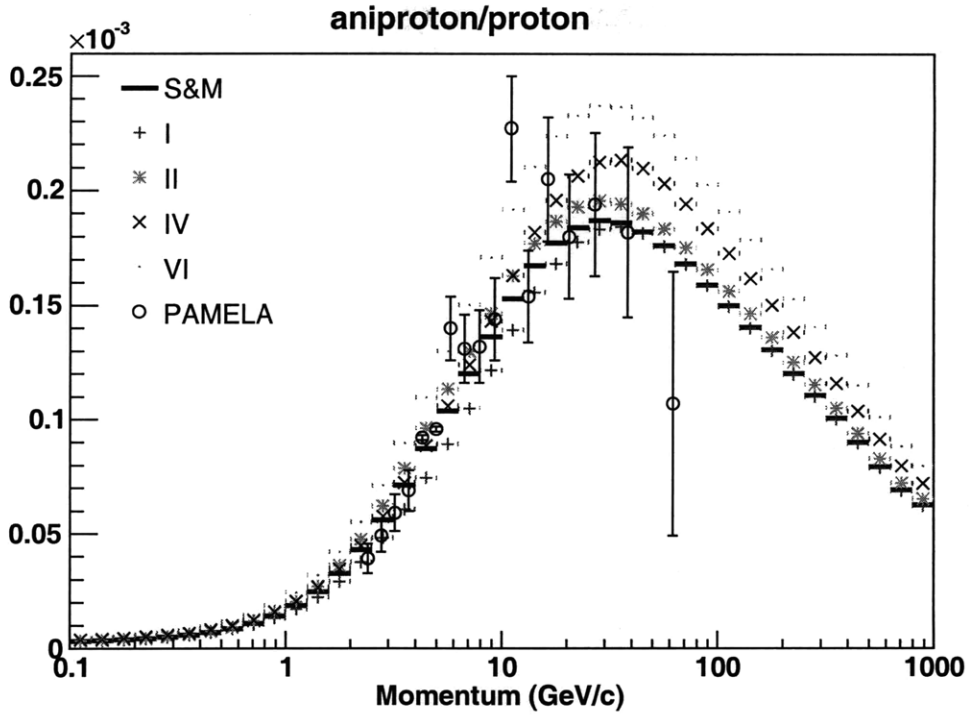
Figure 8-1: Simulations of our favored galactic propagation models, assuming no dark matter. PAMELA antiproton data are from [4].
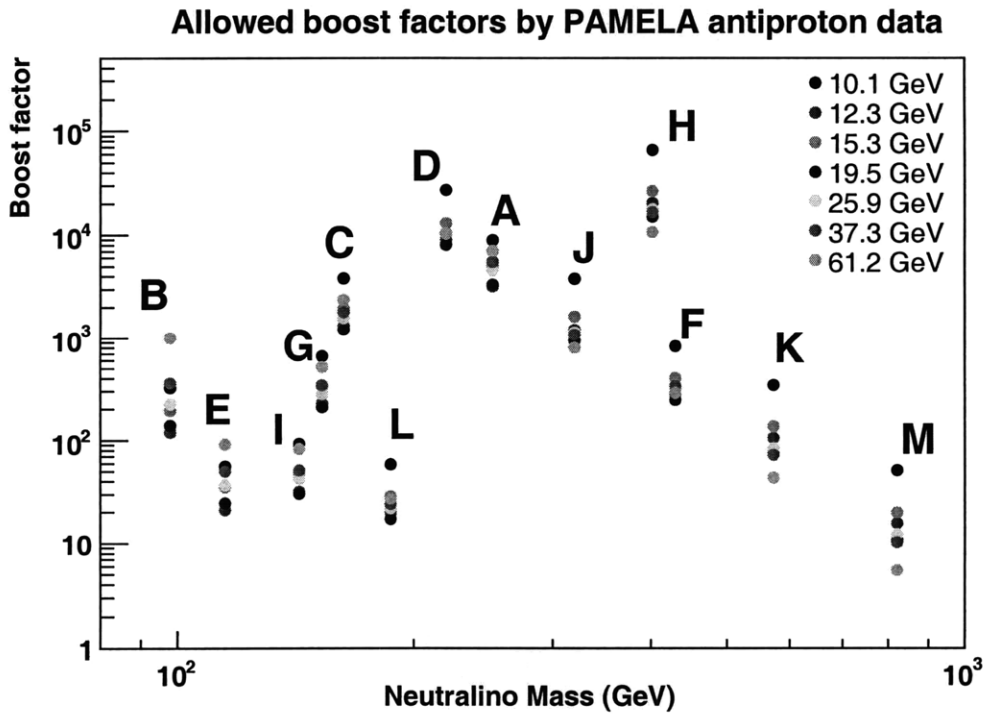
Figure 8-2: Boost factor upper limits allowed by PAMELA antiproton data in each kinetic energy bin above 10 GeV, for SUSY benchmarks A - M.
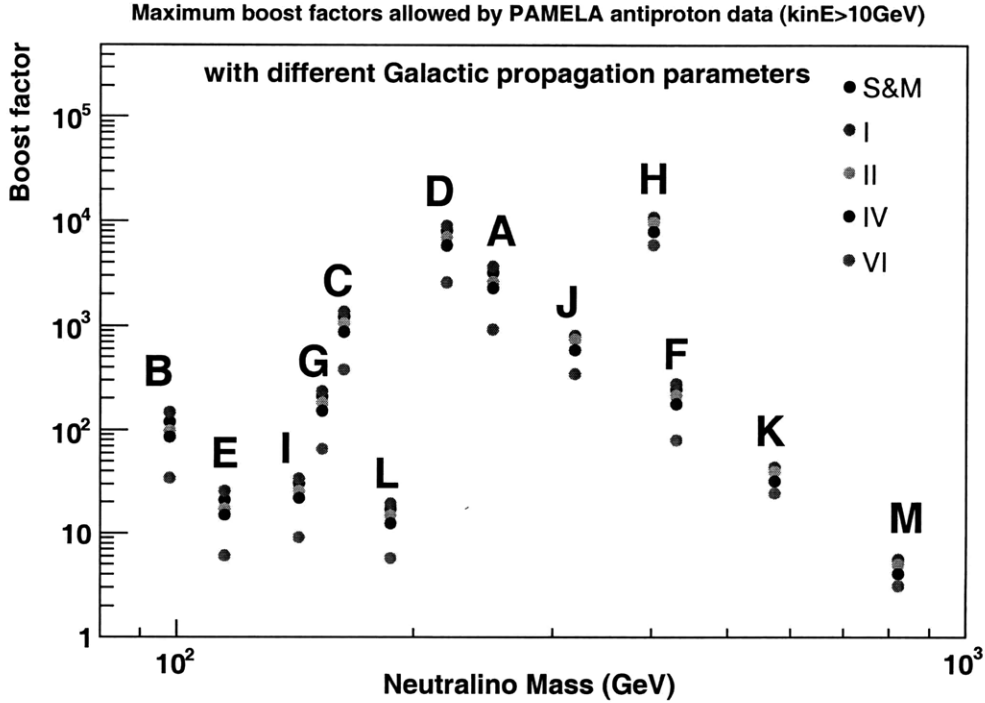
Figure 8-3: Maximum boost factor upper limits in all kinetic energy bin above 10 GeV, for SUSY benchmarks A - M, using different Galactic propagation parameters.

secondary positrons generated by our galactic propagation models have big excess in low energy. One argument is that the measurement at low energy is not very reliable because of the large uncertainties from solar modulation. Figure 8-5 shows the effect from solar modulation on the $e^+/(e^+ + e^-)$ ratio. It seems that solar modulation alone can not explain the big discrepancy between the prediction and the data. Some adjustments in the propagation model are likely necessary. Reducing reacceleration or adding advection could reduce this discrepancy.

Figures 8-6 and Figure 8-7 show that reducing reacceleration or adding advection can significantly reduce the excess in low energy region, but the high energy region is still poorly fit. However, in Chapter 6 we have seen that B/C and proton data disfavor DR propagation model with very small Alfven velocity. In the next section, we use the spectra of $\bar{p}/p$, B/C and protons to check the consistency of adding advection.

8.2.2 Consistency Check

Adding advection can produce good fit to PAMELA antiproton data (see Figure 8-8).

It is still possible to produce good fit to the B/C spectrum when adding moderate advection. However, when the advection is too large, the agreement deteriorates. $dvdz = 20$ km s^{-1} kpc^{-1}, which is needed to fit PAMELA $e^+/(e^+ + e^-)$ data well, is apparently too large for B/C (See Figure 8-9).

It is similar to the situation of B/C, where moderate advection is acceptable, while
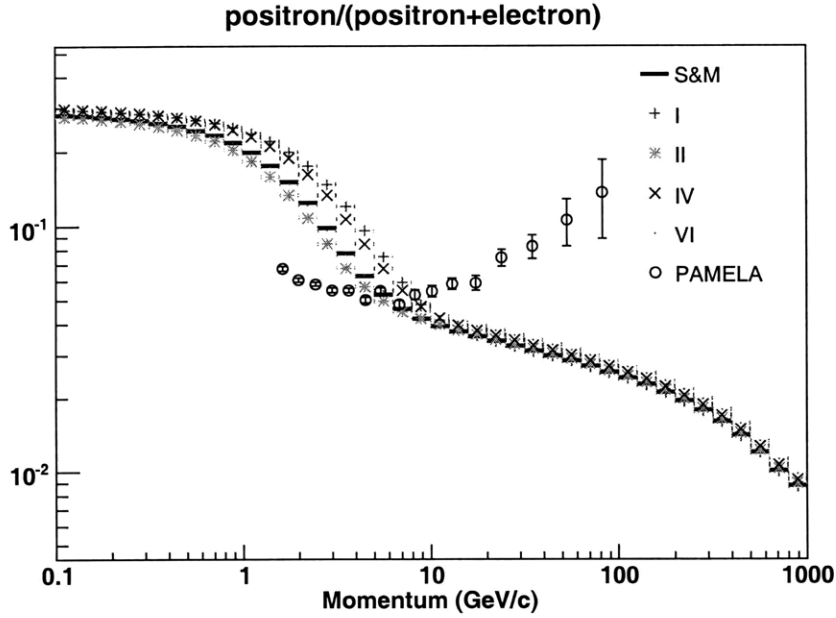
Figure 8-4: Simulations of our favored galactic propagation models, assuming no dark matter. PAMELA positron data are from [?].

too large advection would degrade the fit (See Figure 8-10).

8.2.3 Background + DM signal

There is significant excess of $e^+/(e^+ + e^-)$ events above 10 GeV/c. Positron flux from neutralino annihilations could be one possible explanation. However, large boost factors are required to give a reasonable fit (see Figure 8-11). If the excess results from neutralino annihilation, it should have a cut-off somewhere before the neutralino mass, which should be at several tens to several hundreds GeV. Therefore it would be extremely important to measure the spectrum of $e^+/(e^+ + e^-)$ to higher energies to address the source of this excess.
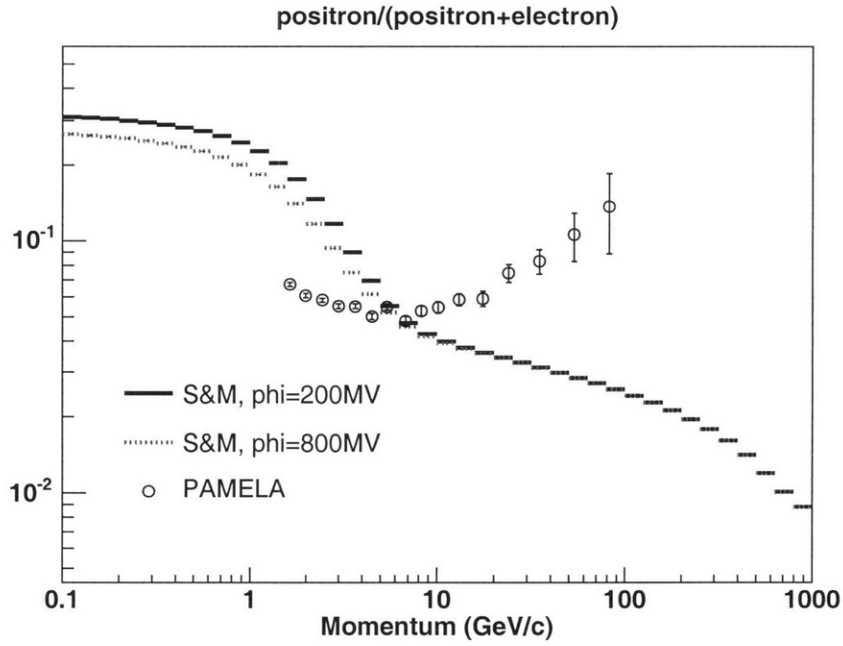
Figure 8-5: Effect of solar modulation on $e^+/(e^+ + e^-)$. Phi is the parameter in the forced field approximation of solar modulation, described in Chapter 3.3.
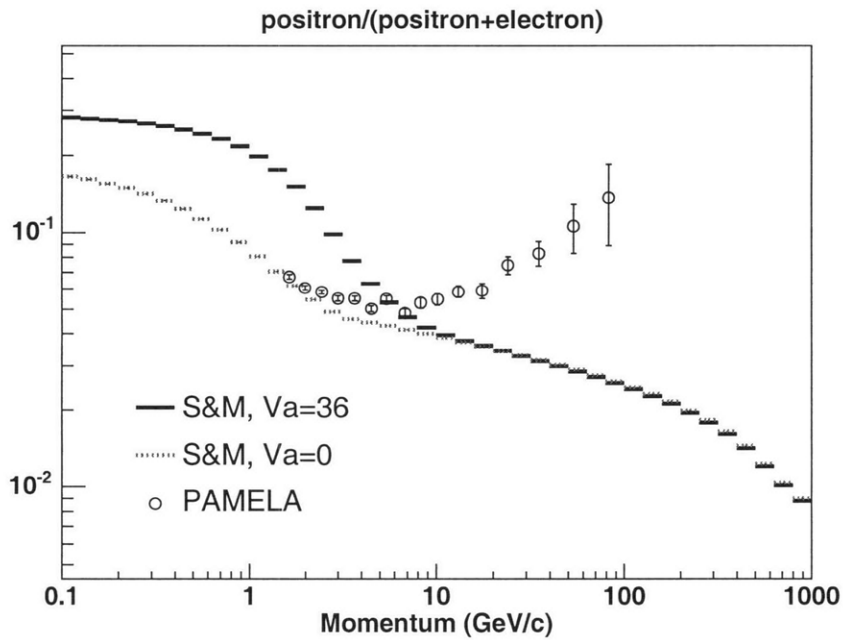
Figure 8-6: Effect of reducing reacceleration on $e^+/(e^+ + e^-)$. Solid line: DR model, $v_A = 36$ km/s; dotted line: DR model , $v_A = 0$;

positron/(positron+electron)
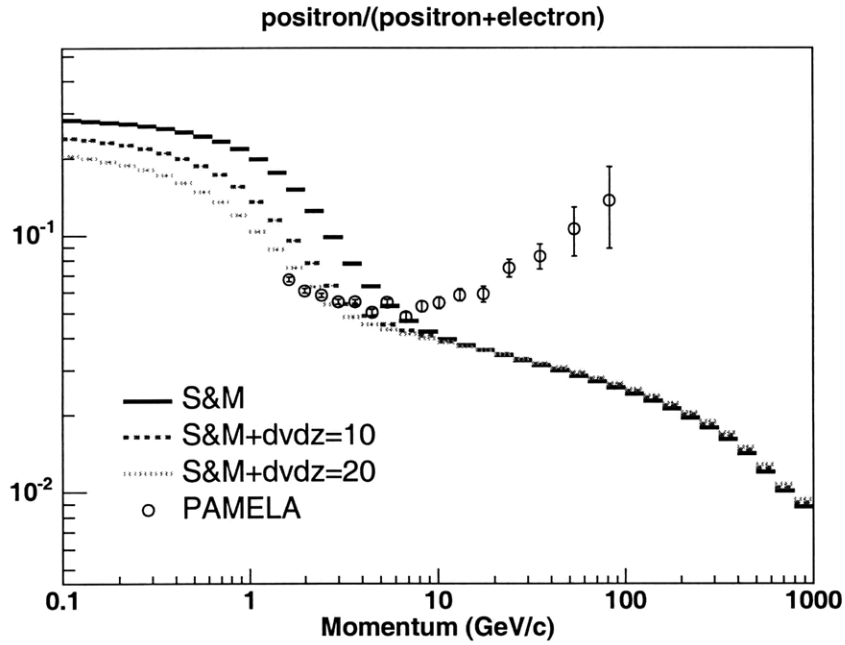
Figure 8-7: (Effect of adding advection on $e^+/(e^+ + e^-)$. Solid line: DR model with parameters at S&M point. Dashed line: DR model at S&M point + advection with $dvdz = 10$ km s^{-1} kpc^{-1}; dotted line: DR model at S&M point + advection with $dvdz = 20$ km s^{-1} kpc^{-1}

aniproton/proton
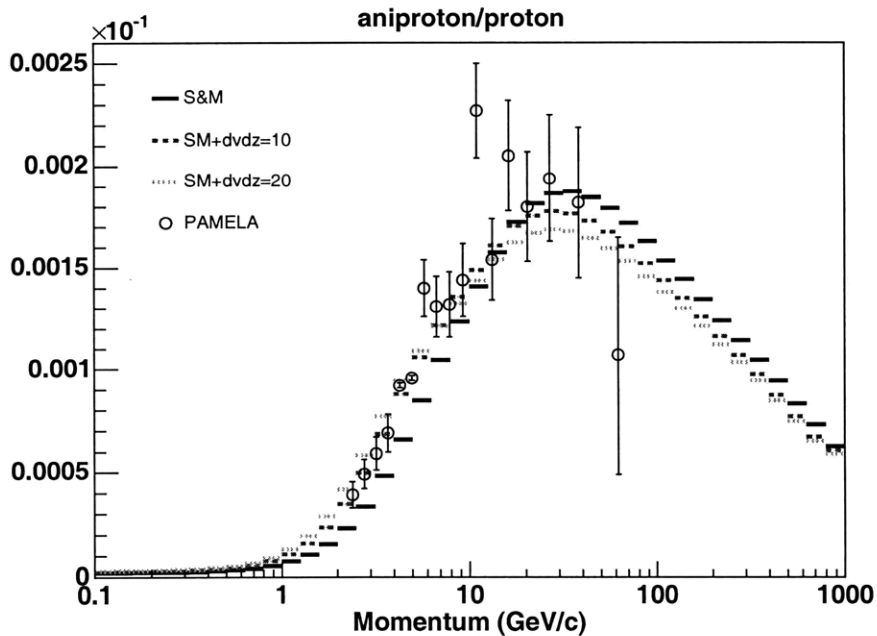
Figure 8-8: Solid line: DR model with parameters at S&M point; dashed line: DR mode at S&M point + advection with $dvdz = 10$ km s^{-1} kpc^{-1}; dotted line: DR model at S&M point + advection with $dvdz = 20$ km s^{-1} kpc^{-1}.

68
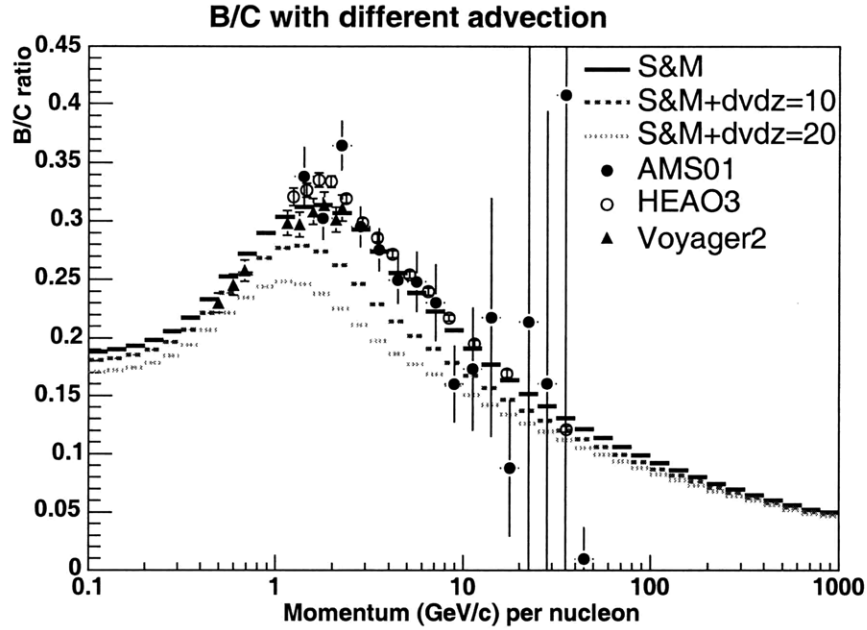
Figure 8-9: Solid line: DR model with parameters at S&M point. Dashed line: DR mode at S&M point + advection with $dvdz = 10$ km s^{-1} kpc^{-1}; dotted line: DR model at S&M point + advection with $dvdz = 20$ km s^{-1} kpc^{-1}.
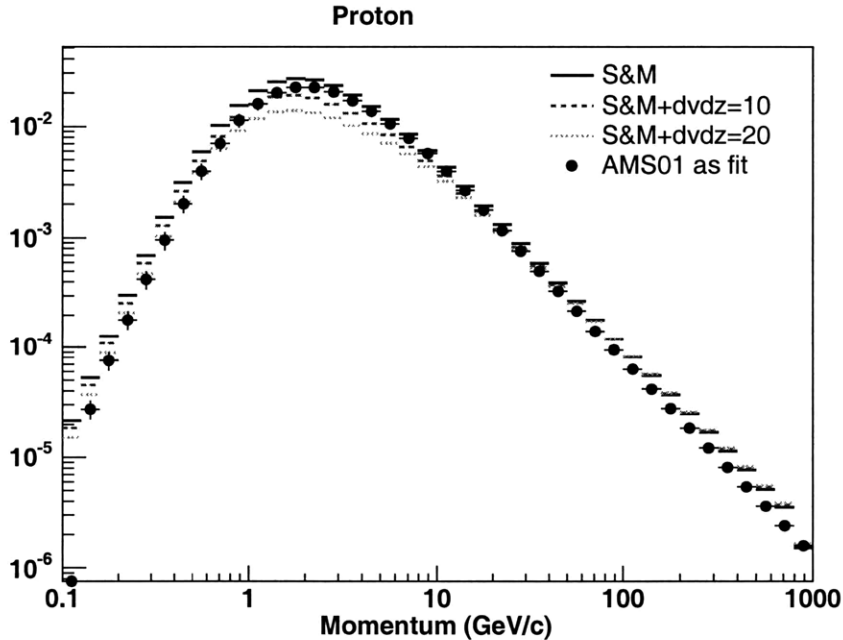
Figure 8-10: Solid line: DR model with parameters at S&M point. Dashed line: DR mode at S&M point + advection with $dvdz = 10$ km s^{-1} kpc^{-1}; dotted line: DR model at S&M point + advection with $dvdz = 20$ km s^{-1} kpc^{-1}. Solid circles: fit from AMS01 proton data.
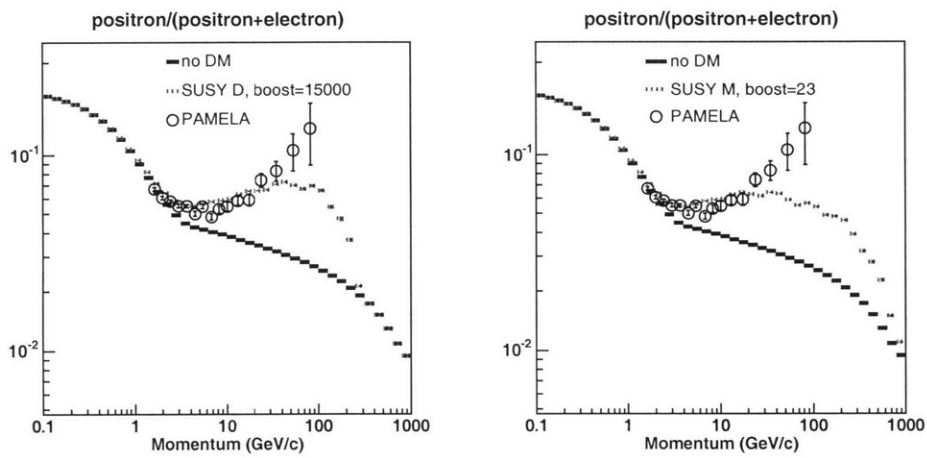
Figure 8-11: Examples of $e^+/(e^+ + e^-)$ with neutralino annihilation for SUSY benchmarks D (left) and M (right). Black line: simulation assuming no dark matter; gray line: simulation with signal from neutralino annihilation, multiplying by a boost. Use DR model at S&M point + advection with $dvdz = 20$ km s^{-1} kpc^{-1} for the Galactic propagation model.

Chapter 9

Conclusion

9.1 Main Message of This Analysis

The 90% upper limits on the boost factor for 13 cMSSM benchmark scenarios [17] are derived, and the effect of CR propagation model uncertainties is assessed. A diffusive reacceleration model is employed to describe the propagation process. An optimal parameter region is obtained from the AMS01 measurement of the B/C ratio and the proton flux. The diffusion coefficient (D_{xx}) and Alfven velocity (V_A) are along a correlated band from lower left to upper right within the region of D_{xx} from 4.5×10^{28} cm^2 s^{-1} to 6×10^{28} cm^2 s^{-1} and V_A from 28 km s^{-1} to 42 km s^{-1}, as shown in Figure 7-1. The resultant uncertainty on the 90% upper bounds of the boost factor is shown to be less than 30%, except for SUSY D, DR V (-51%), and SUSY H, DR I (-43%). Better constraints on the propagation parameters are deduced by including more accurate measurements of the B/C ratio (HEAO3 [29] and Voyager2 [64]), which shrinks the induced uncertainty on the upper bounds of the boost factor to $\sim 10\%$. In conclusion, the resultant error on dark matter limits in the $Z = -1$ spectrum from the uncertainty of galactic propagation modeling is not significant. However, because propagation models can mimic neutralino annihilation in some SUSY models, the impact of propagation models must be studied.

9.2 Broaden the Interpretation of the Boost Factor

Since some of the boost factor limits we get are very large, a natural question to ask would be what is a reasonable number. A recent study showed that the boost factor associated to DM clumps could not exceed at most a factor of ~ 10 in the standard Λ-CDM scenario of structure formation [46]. However, the annihilation rate not only depends on the ρ_{dm}^2, but also depends on the annihilation cross-section. The cross-section could be enhanced by the Sommerfeld effect [45], which is a quantum effect, arising because, in the interaction the wave function of the particles is distorted by the presence of a potential if their kinetic energy is low enough. DM is very non-

relativistic, so they could have the Sommerfeld effect. Such enhancement S goes as $1/\beta$, $S \simeq \pi\alpha/\beta$ [45], where α is the fine structure constant. Take $\beta = 10^{-3}$, we estimate $S \sim 23$. In the clumps, DM particles would have even smaller kinetic energy, therefore a larger Sommerfeld enhancement would be expected for them. The boost factor can thus be interpreted as the product of the clumpiness enhancement and the Sommerfeld enhancement. 10^2 to 10^3 will still be reasonable for a boost factor.

9.3 Message from PAMELA First Results

PAMELA antiproton data is consistent with no DM signal. A maximum boost factor can be derived by requiring the resultant flux not to exceed 2σ error bars of the data (see Figure 8-2). Uncertainties in the Galactic propagation parameters introduce changes in this upper limit of the boost factor, but it will not affect the order of magnitude estimates (see Figure 8-3).

PAMELA sees a significant excess in the e^+ data above 10 GeV. DM annihilation could be a plausible explanation, however, it would require large boost factors. Also, this rising trend is so steep that most of the SUSY benchmark scenarios cannot produce signals to accommodate it. Measurements to higher energy will help address the source of this excess. A cut-off at the energy region of several tens to several hundreds GeV is expected because no charged final states could be produced at energy higher than the neutralino mass.

PAMELA $e^+/(e^+ + e^-)$ data below 10 GeV require little reacceleration or large advection in the Galactic propagation model. However, such propagation models contradict the constraints from B/C measurements. Alternatively, solar modulation is hoped to explain the discrepancy, but the force field model seems to fail to do this job.

9.4 Future Prospects

9.4.1 B/C Ratio Measurement

Figure 9-1 shows all the constituents from which AMS01 B/C measurement error budget is built up, where we can get some indications on how to improve this measurement in the future, probably with AMS02. At the momentum of around several GeV/c per nucleon, where the peak is supposed to be located, the systematic error resulted from imperfect energy resolution dominates. This would wash out the peak, which is one of the main reasons for the poor constraints on propagation parameters placed by our data. AMS02 will have a bending power 5 times stronger than that of AMS01 [23], thanks to the strong superconducting magnet, which can improve the energy resolution. For lower energies (< 1 GeV/nucleon) and higher energies (> 5 GeV/nucleon), data statistical error quickly take over. Having too few events lower than 1 GeV makes it more difficult to recognize the peak, which is another main reason for the poor constraints. AMS02 is supposed to take data for three years to accumulate enough statistics, so this error should be reduced significantly.

Contributions of different components to B/C error
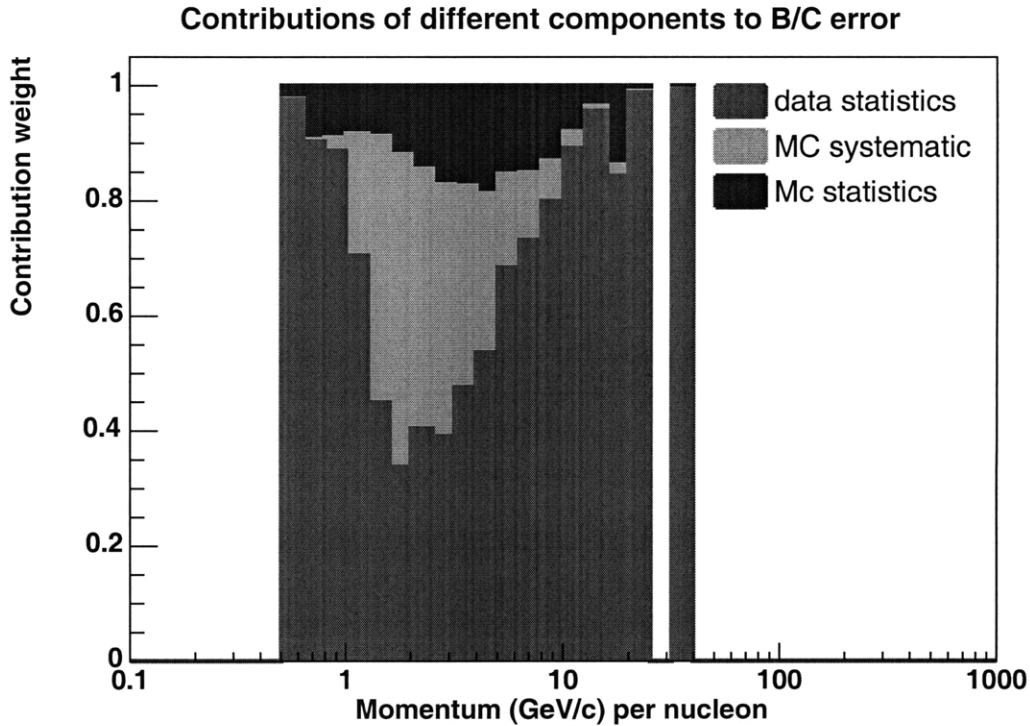
Figure 9-1: Constituents of the error budget of AMS01 B/C ratio measurement.

9.4.2 Moving to Positron and Antiproton Channels

Positron and antiproton signals from dark matter annihilation have similar strength as that of electrons, while having very little background from astrophysical sources. Thus they are much attractive channels to search for dark matter.

The precise measurements of positrons from several GeV to 300 GeV need to reduce the dominating proton background by a factor of 10^6. This would be achieved by AMS02, where its electromagnetic calorimeter would deliver 3 to 4 orders of magnitude and its Transition Radiation Detector (TRD) would deliver another factor of 100 to 1000 Figure [40]. The geometric acceptance of AMS02 is about 400 times of that of PAMELA, which means if run for 3 years, AMS02 could reduce the error bar of current PAMELA measurements by more than a factor of 25. Such high accuracy measurements would start shedding light on dark matter.

Appendix A

Derivation of Alfven Velocity
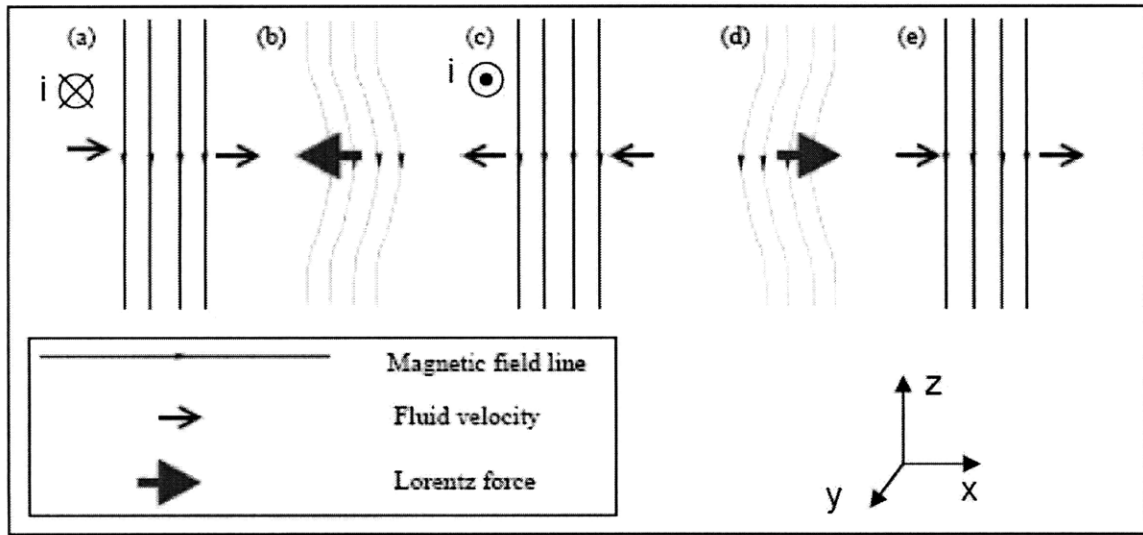
Figure A-1: Mechanism of the generation of Alfven waves.

The interstellar matter, which is mainly composed of hydrogen and helium. can be seen as a perfectly conducting fluid. To balance inertial accelerations and accelerations caused by magnetic field curvature, we have $v_A/T_A = B^2/(L_A\rho)$, where v is the fluid velocity, T_A is the time scale of the inertial magnetic oscillation, L_A is the length scale associated with the oscillation, B is the galactic magnetic field strength, ρ is the interstellar matter density. The conductivity is so high that the magnetic lines of force are attached to the interstellar matter and partaking in its streaming motions. Thus we have $v_A = L_A/T_A$. Combining these relationships, the Alfven velocity is estimated as $v_A = B/\rho^{1/2}$.

The following calculation is according to H. Alfven's 1942 paper [8]. Consider the simple case where the constant magnetic field B_0 is homogeneous and parallel to the z-axis. In order to study a plane wave, we assume all variables depend on time t and z only. The fluid velocity v is parallel to the x-axis. This motion of the conducting fluid gives rise to an electromotive force (emf) which produces Electric currents parallel to

the y-axis (See Figure A-1). Assume $\mu = 1$.

$$\vec{E} = \frac{1}{c}\vec{v} \times \vec{B_0} = -\frac{vB_0}{c}\widehat{e_y} \tag{A.1}$$

This produces a variable magnetic field B parallel to the x-axis.

$$-\frac{1}{c}\frac{\partial B}{\partial t} = \nabla \times E = -\frac{\partial}{\partial z}(\frac{-vB_0}{c})\widehat{e_x} \tag{A.2}$$

Multiply $\frac{\partial}{\partial t}$ with Equation A.2 gives:

$$\frac{1}{c^2}\frac{\partial^2 B}{\partial t^2} = -\frac{\partial^2 v}{\partial t \partial z}B_0 \tag{A.3}$$

The hydrodynamic equation:

$$\rho\frac{\partial v}{\partial t} = \frac{1}{c}(i \times B_0) - \nabla p \tag{A.4}$$

Where the current i parallel to y-axis us generated by:

$$\frac{4\pi}{c}i = \nabla \times B = \frac{\partial B}{\partial z}\widehat{e_y} \tag{A.5}$$

Plug Equation A.5 in Equation A.4, we get:

$$\rho\frac{\partial v}{\partial t} = -\frac{1}{4\pi c^2}\frac{\partial B}{\partial z}B_0\widehat{e_x} - \nabla p \tag{A.6}$$

$\nabla\times$ Equation A.6 gives:

$$\rho\frac{\partial^2 v}{\partial z \partial t} = -\frac{1}{4\pi c^2}\frac{\partial^2 B}{\partial z^2}B_0 \tag{A.7}$$

Combine Equation A.3 and Equation A.7, we get:

$$\frac{\partial^2 B}{\partial t^2} = \frac{B_0{}^2}{4\pi\rho}\frac{\partial^2 B}{\partial z^2} \tag{A.8}$$

Since B has a plane wave solution: $B \propto e^{i(\omega t - kz)}$, thus

$$\frac{B_0{}^2}{4\pi\rho} = v_A{}^2 v_A = \frac{B_0}{sqrt4\pi\rho} \tag{A.9}$$

75

Appendix B

GALPROP Parameters (default setting)

```
=====================value
Title = conventional/2D 4 kpc tuned to agree with ACE
Title = source isotopic distr. of an element = solar isot. abund. distr.
n_spatial_dimensions = 2
r_min =00.0        min r
r_max =20.00        max r
dr = 1.0        delta r
z_min =-4.0        min z
z_max =+4.0        max z
dz = 0.1        delta z

x_min = 0.0        min x
x_max =+15.0        max x
dx = 0.2        delta x y_min = 0.0        min y
y_max =+15.0        max y
dy = 0.2        delta y

p_min =1000        min momentum (MV)
p_max =4000        max momentum
p_factor =1.50        momentum factor

Ekin_min =1.0e1        min kinetic energy per nucleon (MeV)
Ekin_max =1.0e7        max kinetic energy per nucleon
Ekin_factor =1.2        kinetic energy per nucleon factor

p_Ekin_grid = Ekin        p———Ekin alignment

E_gamma_min = 1.e0        min gamma-ray energy (MeV)
E_gamma_max = 1.e8        max gamma-ray energy (MeV)
E_gamma_factor = 1.4        gamma-ray energy factor
```

77

integration_mode = 1   integr.over part.spec.: =1-old E*logE; 0=1-PL analyt.

nu_synch_min = 1.0e6   min synchrotron frequency (Hz)
nu_synch_max = 1.0e10   max synchrotron frequency (Hz)
nu_synch_factor = 2.0   synchrotron frequency factor

long_min = 0.50   gamma-ray intensity skymap longitude minimum (deg)
long_max =359.50   gamma-ray intensity skymap longitude maximum (deg)
lat_min =-89.50   gamma-ray intensity skymap latitude minimum (deg)
lat_max =+89.50   gamma-ray intensity skymap latitude maximum (deg)
d_long = 1.00   gamma-ray intensity skymap longitude binsize (deg)
d_lat = 1.00   gamma-ray intensity skymap latitude binsize (deg)

D0_xx =5.75e28   diffusion coefficient at reference rigidity
D_rigid_br =4.0e3   reference rigidity for diffusion coefficient in MV
D_g_1 = 0.34   diffusion coefficient index below reference rigidity
D_g_2 = 0.34   diffusion coefficient index above reference rigidity
diff_reacc =1   0=no reacc.; 1,2=incl.diff.reacc.; -1==beta$\hat{3}$ Dxx; 11=Kolmogorov+damping;
12=Kraichnan+damping
v_Alfven =36   Alfven speed in km s-1

damping_p0 = 1.e6   MV -some rigidity (where CR density is low)
damping_const_G = 0.02   a const derived from fitting B/C
damping_max_path_L = 3.e21   Lmax 1 kpc, max free path

convection =0   1=include convection
v0_conv =0.   km s-1   v_conv=v0_conv+dvdz_conv*dz
dvdz_conv =5.   km s-1 kpc-1   v_conv=v0_conv+dvdz_conv*dz

nuc_rigid_br =9.0e3   reference rigidity for nucleus injection index in MV
nuc_g_1 =1.82   nucleus injection index below reference rigidity
nuc_g_2 =2.36   nucleus injection index index above reference rigidity

inj_spectrum_type = rigidity   rigidity——beta_rig——Etot nucleon injection
spectrum type

electron_g_0 =1.60   electron injection index below electron_rigid_br0
electron_rigid_br0 =4.0e3   reference rigidity0 for electron injection index in MV
electron_g_1 =2.5   electron injection index below reference rigidity
electron_rigid_br =1.0e9   reference rigidity for electron injection index in MV
electron_g_2 =5.0   electron injection index index above reference rigidity

He_H_ratio =0.11   He/H of ISM, by number
X_CO =0.4E20, 0.4E20, 0.6E20, 0.8E20, 1.5E20, 10.0E20, 10.0E20, 10.0E20, 10.0E20
conversion factor from CO integrated temperature to H2 column density

for CO rings 0.0 - 1.5 - 3.5 - 5.5 - 7.5 - 9.5 - 11.5 - 13.5 - 15.5 - 50 kpc
fragmentation =1   1=include fragmentation
momentum_losses =1   1=include momentum losses
radioactive_decay =1   1=include radioactive decay
K_capture =1   1=include K-capture

start_timestep =1.0e7
end_timestep =1.0e2
timestep_factor =0.25
timestep_repeat =20   number of repeats per timestep in timetep_mode=1
timestep_repeat2 =0   number of timesteps in timetep_mode=2
timestep_print =10000   number of timesteps between printings
timestep_diagnostics =10000   number of timesteps between diagnostics
control_diagnostics =0   control detail of diagnostics

network_iterations = 2   number of iterations of entire network

prop_r = 1   1=propagate in r (2D)
prop_x = 1   1=propagate in x (2D,3D)
prop_y = 1   1=propagate in y (3D)
prop_z = 1   1=propagate in z (3D)
prop_p = 1   1=propagate in momentum

use_symmetry = 0   0=no symmetry, 1=optimized symmetry, 2=xyz symmetry by copying(3D)

vectorized = 0   0=unvectorized code, 1=vectorized code

source_specification = 0   2D::1:r,z=0 2:z=0 3D::1:x,y,z=0 2:z=0 3:x=0 4:y=0
source_model = 1   0=zero 1=parameterized 2=Case&B 3=pulsars 4= 5=S&Mattox 6=S&Mattox with cutoff
source_parameters_1 = 0.5   model 1:alpha
source_parameters_2 = 1.0   model 1:beta
source_parameters_3 = 20.0   model 1:rmax

n_cr_sources = 0   number of pointlike cosmic-ray sources 3D only!
cr_source_x_01 = 10.0   x position of cosmic-ray source 1 (kpc)
cr_source_y_01 = 10.0   y position of cosmic-ray source 1
cr_source_z_01 = 0.1   z position of cosmic-ray source 1
cr_source_w_01 = 0.1   sigma width of cosmic-ray source 1
cr_source_L_01 = 1.0   luminosity of cosmic-ray source 1
cr_source_x_02 = 3.0   x position of cosmic-ray source 2
cr_source_y_02 = 4.0   y position of cosmic-ray source 2
cr_source_z_02 = 0.2   z position of cosmic-ray source 2

cr_source_w_02 = 2.4   sigma width of cosmic-ray source 2
cr_source_L_02 = 2.0   luminosity of cosmic-ray source 2

SNR_events = 0   handle stochastic SNR events
SNR_interval = 1.0e4   time interval in years between SNR in 1 kpc^3 volume
SNR_livetime = 1.0e4   CR-producing live-time in years of an SNR
SNR_electron_sdg = 0.00   delta electron source index Gaussian sigma
SNR_nuc_sdg = 0.00   delta nucleus source index Gaussian sigma
SNR_electron_dgpivot = 5.0e3   delta electron source index pivot rigidity (MeV)
SNR_nuc_dgpivot = 5.0e3   delta nucleus source index pivot rigidity (MeV)

HI_survey = 9   HI survey 8=orig 8 rings 9=new 9 rings
CO_survey = 9   CO survey 8=orig 8 rings 9=new 9 rings

B_field_model = 050100020   bbbrrrzzz   bbb=10*B(0)   rrr=10*rscale   zzz=10*zscale
ISRF_file = MilkyWay_DR0.5_DZ0.1_DPHI10_RMAX20_ZMAX5_galprop_format.fits
input ISRF file
ISRF_factors = 1.0,1.0,1.0   ISRF factors for IC calculation: optical, FIR, CMB

proton_norm_Ekin = 1.00e+5 proton kinetic energy for normalization (MeV)
proton_norm_flux = 4.90e-9 to renorm nuclei/flux of protons at norm energy (cm^2 sr^1 s^1 MeV^1)

electron_norm_Ekin = 34.5e3   electron kinetic energy for normalization (MeV)
electron_norm_flux = .40e-9   flux of electrons at normalization energy (cm^2 sr^1 s^1 MeV^1)

max_Z = 28   maximum number of nucleus Z listed
use_Z_1 = 1
use_Z_2 = 1
use_Z_3 = 1
use_Z_4 = 1
use_Z_5 = 1
use_Z_6 = 1
use_Z_7 = 1
use_Z_8 = 1
use_Z_9 = 1
use_Z_10 = 1
use_Z_11 = 1
use_Z_12 = 1
use_Z_13 = 1
use_Z_14 = 1
use_Z_15 = 1
use_Z_16 = 1

use_Z_17 = 1
use_Z_18 = 1
use_Z_19 = 1
use_Z_20 = 1 use_Z_21 = 1
use_Z_22 = 1
use_Z_23 = 1
use_Z_24 = 1
use_Z_25 = 1
use_Z_26 = 1
use_Z_27 = 1
use_Z_28 = 1
use_Z_29 = 0
use_Z_30 = 0

iso_abundance_01_001 = 1.06e+06   H
iso_abundance_01_002 = 34.8
iso_abundance_02_003 = 9.033   He
iso_abundance_02_004 = 7.199e+04
iso_abundance_03_006 = 0   Li
iso_abundance_03_007 = 0
iso_abundance_04_009 = 0   Be
iso_abundance_05_010 = 0   B
iso_abundance_05_011 = 0
iso_abundance_06_012 = 2819   C
iso_abundance_06_013 = 5.268e-07
iso_abundance_07_014 = 182.8   N
iso_abundance_07_015 = 5.961e-05
iso_abundance_08_016 = 3822   O
iso_abundance_08_017 = 6.713e-07
iso_abundance_08_018 = 1.286
iso_abundance_09_019 = 2.664e-08   F
iso_abundance_10_020 = 312.5   Ne
iso_abundance_10_021 = 0.003556
iso_abundance_10_022 = 100.1
iso_abundance_11_023 = 22.84   Na
iso_abundance_12_024 = 658.1   Mg
iso_abundance_12_025 = 82.5
iso_abundance_12_026 = 104.7
iso_abundance_13_027 = 76.42   Al
iso_abundance_14_028 = 725.7   Si
iso_abundance_14_029 = 35.02
iso_abundance_14_030 = 24.68
iso_abundance_15_031 = 4.242   P
iso_abundance_16_032 = 89.12   S
iso_abundance_16_033 = 0.3056

iso_abundance_16_034 = 3.417
iso_abundance_16_036 = 0.0004281
iso_abundance_17_035 = 0.7044   Cl
iso_abundance_17_037 = 0.001167
iso_abundance_18_036 = 9.829   Ar
iso_abundance_18_038 = 0.6357
iso_abundance_18_040 = 0.001744
iso_abundance_19_039 = 1.389   K
iso_abundance_19_040 = 3.022
iso_abundance_19_041 = 0.0003339
iso_abundance_20_040 = 51.13   Ca
iso_abundance_20_041 = 1.974
iso_abundance_20_042 = 1.134e-06
iso_abundance_20_043 = 2.117e-06
iso_abundance_20_044 = 9.928e-05
iso_abundance_20_048 = 0.1099
iso_abundance_21_045 = 1.635   Sc
iso_abundance_22_046 = 5.558   Ti
iso_abundance_22_047 = 8.947e-06
iso_abundance_22_048 = 6.05e-07
iso_abundance_22_049 = 5.854e-09
iso_abundance_22_050 = 6.083e-07
iso_abundance_23_050 = 1.818e-05   V
iso_abundance_23_051 = 5.987e-09
iso_abundance_24_050 = 2.873   Cr
iso_abundance_24_052 = 8.065
iso_abundance_24_053 = 0.003014
iso_abundance_24_054 = 0.4173
iso_abundance_25_053 = 6.499   Mn
iso_abundance_25_055 = 1.273
iso_abundance_26_054 = 49.08   Fe
iso_abundance_26_056 = 697.7
iso_abundance_26_057 = 21.67
iso_abundance_26_058 = 3.335
iso_abundance_27_059 = 2.214   Co
iso_abundance_28_058 = 28.88   Ni
iso_abundance_28_060 = 11.9
iso_abundance_28_061 = 0.5992
iso_abundance_28_062 = 1.426
iso_abundance_28_064 = 0.3039

total_cross_section = 2   total cross section option: 0=L83 1=WA96 2=BP01
cross_section_option = 012   100*i+j i=1: use Heinbach-Simon C,O-¿B j=kopt
j=11=Webber, 21=ST

t_half_limit = 1.0e4 year - lower limit on radioactive half-life for explicit inclusion

primary_electrons = 1
secondary_positrons = 1
secondary_electrons = 1
secondary_antiproton = 2   0 1 2
tertiary_antiproton = 1
secondary_protons = 1

gamma_rays = 0   1=compute gamma rays, 2=compute HI,H2 skymaps separately
pi0_decay = 0   1= old formalism 2=Blattnig et al.
IC_isotropic = 1   1,2= compute isotropic IC: 1=compute full, 2=store skymap components
IC_anisotropic = 1   1,2,3= compute anisotropic IC: 1=full, 2=approx., 3=isotropic
bremss = 0   1=compute bremsstrahlung
synchrotron = 0   1=compute synchrotron

comment = the dark matter (DM) switches and user-defined parameters
DM_positrons = POSITRON_ON   1=compute DM positrons
DM_electrons = ELECTRON_ON   1=compute DM electrons
DM_antiprotons = ANTIPROTON_ON   1=compute DM antiprotons
DM_gammas = 0   1=compute DM gammas

DM_double0 = 2.8   core radius, kpc
DM_double1 = 0.43   local DM mass density, GeV cm-3
DM_double2 = ENERGY   neutralino mass, GeV
DM_double3 = 40.   positron width distribution, GeV
DM_double4 = 40.   positron branching
DM_double5 = 40.   electron width distribution, GeV
DM_double6 = 30.   electron branching
DM_double7 = 50.   pbar width distribution, GeV
DM_double8 = 40.   pbar branching
DM_double9 =3.e-25   ¡cross_sec*V¿-thermally overaged, cm3 s-1

DM_int0 = 1   isothermal profile
DM_int1 = 1
DM_int2 = 1
DM_int3 = 1
DM_int4 = 1
DM_int5 = 1
DM_int6 = 1
DM_int7 = 1
DM_int7 = 1
DM_int9 = 1

output_gcr_full = 0   output full galactic cosmic ray array

warm_start = 0   read in nuclei file and continue run

verbose = 0   verbosity: 0=min,10=max ¡0: selected debugs

test_suite = 0   run test suite instead of normal run

Appendix C

Unfolding Method: Convergent Weights

What we measure on the detector can be expressed as

$$f(p) = \int A(p, p') g(p') dp' \tag{C.1}$$

where $f(p)$ is the recorded spectrum, $g(p')$ is the incident spectrum, $A(p, p')$ is the acceptance matrix, which is the probability that a particle with momentum p' is detected with momentum p. $f(p)$ is known and we want to invert the acceptance matrix to obtain the incident spectrum $g(p')$. This is not a trivial problem, since the acceptance matrix is singular. If we use Singular Value Decomposition class to invert the matrix directly, a lot of negative numbers are generated in the inverted matrix which have no physical meaning. Instead, the method of convergent weights [35] [43] is used to solve this unfolding problem. The iterative procedure is formulated as following:

$$g^{j+1}(p') = \frac{\int r^j(p) A(p, p') dp}{A(p, p') dp} g^j(p') \tag{C.2}$$

where

$$r^j(p) = \frac{f(p)}{\int A(p, p') g^j(p') dp'} \tag{C.3}$$

There are two main sources of errors, one is the statistics error from data, the other is the systematic error from the acceptance matrix (the statistic error from acceptance can be reduced to an ignorable level by generating more Monte Carlo events). The errors are propagated quadratically.

Appendix D

FitMethod

χ^2 minimization (Equation D.1 or log likelihood maximization ?? is used in the fitting. Gaussion error is assumed in the fit, so the two methods are accentually equivalent.

$$f_{ChiSquare} = \sum_{i \in bins} \frac{(d_i - y_i)^2}{\sigma_i^2} \qquad (D.1)$$

$$f_{LogLikelihood} = - \sum_{i \in bins} \left(\frac{(d_i - y_i)^2}{\sigma_i^2} + ln\sigma_i \right) \qquad (D.2)$$

where index i stands for the momentum bin. d_i and y_i are data and theoretical prediction at momentum bin i respectively. σ_i is the total error including statistical error from data and systematic error encoding in the acceptance, $\sigma_i^2 = \sigma_{i,stat}^2 + \sigma_{i,sys}^2$. The program MINUIT [2]is used to do this optimization problem and a gradient descent method is chosen.Uncertainty for the fit parameter α is calculated as $\sigma_\alpha = (\frac{d^2 f}{d\alpha^2})^{-1}$.

The difference between the value of the fit function (χ^2 or log likelihood) and that of the best-fit point determines the contours of equal likelihood, see Table D-1. There are three free parameters in the DM boost factor fit, so we use $\Delta\chi^2 = 6.25$ to set the contour of 90% confidence ellipsoid. There are two free parameters in the B/C ratio fit, so we use $\Delta\chi^2$=1.39, 2.41, and 4.61 to set the 50%, 70% and 90% confidence ellipsoid respectively.

Number of Parameters	Confidence level (probability contents desired inside hypercontour of $\chi^2 = \chi^2_{min} + UP$)				
	50%	70%	90%	95%	99%
1	0.46	1.07	2.70	3.84	6.63
2	1.39	2.41	4.61	5.99	9.21
3	2.37	3.67	6.25	7.82	11.36
4	3.36	4.88	7.78	9.49	13.28
5	4.35	6.06	9.24	11.07	15.09
6	5.35	7.23	10.65	12.59	16.81
7	6.35	8.38	12.02	14.07	18.49
8	7.34	9.52	13.36	15.51	20.09
9	8.34	10.66	14.68	16.92	21.67
10	9.34	11.78	15.99	18.31	23.21
11	10.34	12.88	17.29	19.68	24.71
	If FCN is $-\log(\text{likelihood})$ instead of χ^2, all values of UP should be divided by 2.				

Figure D-1: Table of UP for multi-parameter confidence regions [2]

Bibliography

[1] [arXiv:astro-ph/0310192v1].

[2] Minuit reference manual.

[3] *Chinese Journal of Physics*, 39:1, 2001.

[4] O. Adriani et al. A new measurement of the antiproton-to-proton flux ratio up to 100gev in the cosmic radiation. [arXiv:0810.4994].

[5] M. Aguilar et al. *Physics Reports*, 366(6):331–405, 2002.

[6] S. Ahlen. *NIM A*, 350:351, 1994.

[7] J. Alcaraz et al. *Nuovo Cimiento II*, 122 A:1325–1344, 1999.

[8] H. Alfven. *Nature*, 150:405, 1942.

[9] D. Alvisi et al. *NIM A*, 437:212, 1999.

[10] U. Amaldi et al. *Phys.Lett.B*, 260:447, 1991.

[11] L. Baldini et al. *Proc. of 27th ICRC*, pages 2211–2214, 2001.

[12] E. A. Baltz et al. *Phys.Rev.D*, 65:063511, 2002. [arXiv: astro-ph/0109318].

[13] D. Barancourt et al. *NIM A*, 465:306, 2001.

[14] F. Barao et al. *NIM A*, 454:174, 2000.

[15] V. Barger et al. [arXiv:hep-ph/0003154].

[16] S. W. Barwick and others [HEAT collaboration]. *ApJ*, 482:L191, 1997. [arXiv:astro-ph/9703192].

[17] M. Battaglia et al. *Eur.Phys.J. C33 273*, C33:273, 2004. [arXiv:hep-ph/0306219].

[18] G. W. Bennett and others [Muon g 2 Collaboration]. *Phys.Rev.Lett.*, 89:101804, 2002. [arXiv:hep-ex/0208001].

[19] L. Bergstrom et al. *Astropart. Phys.*, 9:137, 1998. [arXiv:astro-ph/9712318].

[20] L. Bergstrom et al. *Phys.Rev.D*, 59:043506, 1999.

[21] G. Bertone et al. Particle dark matter: Evidence, candidates and constraints. 2008. [arXiv:hep-ph/0404175].

[22] E. Bertschinger. *Phys.Rev.D*, 74:063509, 2006. [arXiv:astro-ph/0607319].

[23] B. Blau et al. *NIM A*, 518:139, 2004.

[24] G. Carosi. Ph.d thesis. *MIT Physics Department*, 2006.

[25] M. Cristinziani. Ph.d thesis. *Atelier de reproduction de la Section de physique*, 2002.

[26] DMSAG. Report on the direct detection and study of dark matter. 2007.

[27] F. Donato et al. *Phys.Rev.D*, 69:063501, 2004. [arXiv:astro-ph/0306207].

[28] J. Ellis et al. *Phys.Rev.D*, 71:095007, 2005. [arXiv:hep-ex/0502001].

[29] J. J. Engelmann et al. *Astron.Astrophys.*, 233:96–111, 1990.

[30] E. Fermi. *Phys.Rev.*, 75(8):1169, 1949.

[31] L. J. Gleenson and W. I. Axford. *The Astrophys. J.*, 154:1011, 1968.

[32] P. Gondolo et al. *JCAP*, 0407:008, 2004. [arXiv:astro-ph/0406204].

[33] K. Hagiwara et al. *Phys.Rev.D*, 66:010001, 2002.

[34] F. Halzen and D. Hooper. *Rept. Prog. Phys.*, 65:1025, 2002. [arXiv:astro-ph/0204527].

[35] R. Henning. Ph.d thesis. *MIT Phsyics Department*, 2003.

[36] T. Hurth. *Rev.Mod.Phys.*, 75:1159, 2003. [arXiv:hep-ph/0212304].

[37] G. Jungman et al. *Phys.Rept.*, 267:195, 1996.

[38] M. Kamionkowski and A. Kinkhabwala. *Phys. Rev. D*, 57(6):3256, 1998.

[39] G. L. Kane et al. *Phys.Rev.D*, 49:6173, 1994. [arXiv:hep-ph/9312272].

[40] T. Kirn. *NIM A*, 581:156, 2007.

[41] E. W. Kolb and I. I. Tkachev. *Phys.Rev.D*, 50:769, 1994.

[42] K. o. Komatsu. Wmap 5 year result. [arXiv:astro-ph/0803.0547].

[43] A. Kondor. *Nucl.Inst.and Math*, 216, 1982.

[44] M. Kowalski et al. *ApJ*, 686:749, 2008. [arXiv:0804.4142].

[45] M. Lattanzi and J. Silk. 2008. astro-ph/0812.0360.

[46] T. Lavalle et al. *Astron. Astrophys.*, 479:427, 2008.

[47] LEP2. "combined lep chargino results, up to 208 gev", "combined lep selec-trn/smoun/stau results, 183-208 gev". *Joint LEP 2 Supersymmetry Working Group*. LEP website.

[48] K. Lodders. *ApJ*, 591:1220, 2003.

[49] B. Moore et al. *Astron. Soc.*, 310:1147, 1999. [arXiv:astro-ph/9903164].

[50] A. Morselli et al. *Nucl. Phys. Proc. Suppl.*, 113:213, 2002. [arXiv:astro-ph/0211327].

[51] I. V. Moskalenko et al. *ApJ*, 565:280, 2002.

[52] J. F. Navarro et al. *ApJ*, 462:563, 1996. [arXiv:astro-ph/9508025].

[53] H. P. Nilles. *Phys.Lett.B*, 115:193, 1982.

[54] PDG. Cosmic ray (rev.). 2008.

[55] G. Rybka. Ph.d thesis. *MIT Phsyics Department*, 2007.

[56] U. Seljak et al. *JCAP*, 0610:014, 2006.

[57] E. S. Seo and V. S. Ptuskin. *The Astrophy.J.*, 431:705, 1994.

[58] J. Simpson. *Ann.Rev.Nucl.Part.Sci.*, 33:323, 1983.

[59] T. Sjostrand et al. *Computer Physics Communications*, 135:238–259, 2001.

[60] Y. Sofue and V. Rubin. *Annual Reviews of Astron. & Astrophys.*, 39:137, 2001.

[61] A. W. Strong. and J. R. Mattox. *A&A*, 308:L21, 1996.

[62] A. W. Strong and I. V. Moskalenko. *ApJ*, 509:212, 1998.

[63] J. Sullivan et al. *NIM*, 95:5–11, 1971.

[64] W. R. Webber et al. *ApJ*, 599:582–595, 2003.

[65] S. Weinberg. *Phys.Rev.D*, 26:287, 1982.

[66] V. N. Zirakashvili et al. *A&A*, 311:113, 1996.

[67] F. Zwicky. *ApJ*, 86:217, 1937.